Carbon ion therapy for lung cancer: enhancing dose conformity and cost-effectiveness

Kohlenstoffionentherapie bei Lungenkrebs: Verbesserung der Dosiskonformität und Kosteneffizienz

Zur Erlangung des akademischen Grades Doktor-Ingenieur (Dr.-Ing.)
Genehmigte Dissertation im Fachbereich Elektrotechnik und Informationstechnik von
Maria Chiara Martire
Tag der Genehmigung: 10. März 2026, Tag der Prüfung: 17. Juni 2026

1. Gutachten: Prof. Dr. Christian Graeff
2. Gutachten: Prof. Dr. Anna Bakenecker

Darmstadt, Technische Universität Darmstadt

TECHNISCHE UNIVERSITÄT DARMSTADT

etit

GSI

FAIR

Bundesministerium für Forschung, Technologie und Raumfahrt

Carbon ion therapy for lung cancer: enhancing dose conformity and cost-effectiveness

at the Electrical Engineering and Information Technology department of the Technischen Universität Darmstadt

Approved in fulfilment of the requirements for the degree of Doctor-Engineer (Dr.-Ing.)

Doctoral thesis by

Maria Chiara Martire

First assessor: Prof. Dr. Christian Graeff

Second assessor: Prof. Dr. Anna Bakenecker

Darmstadt 2026

Carbon ion therapy for lung cancer: enhancing dose conformity and cost-effectiveness

Kohlenstoffionentherapie bei Lungenkrebs: Verbesserung der Dosiskonformität und Kosteneffizienz

Approved doctoral thesis in the department of Electrical Engineering and Information Technology by Maria Chiara Martire

Date of thesis approval: 10th March 2026

Date of thesis defense: 17th June 2026

Darmstadt, Technische Universität Darmstadt

Thesis written in Darmstadt, Technische Universität Darmstadt

Year thesis published in TUprints: 2026

Date of the viva voce: 17th June 2026

DOI: https://doi.org/10.26083/tuda-8334

URL: https://tuprints.ulb.tu-darmstadt.de/handle/tuda/16028

URN: https://nbn-resolving.org/urn:nbn:de:tuda-tuda-160283

Alla mia Famiglia,

Cristina, Roberto e Francesco.

Abstract

In radiotherapy, to achieve a conformal dose distribution is essential to minimize toxicity in critical organs. Particle therapy offers the potential for highly conformal dose delivery due to the precise energy deposition of charged particles. Carbon ion radiotherapy additionally provides enhanced radiobiological effectiveness, making it a promising treatment modality for complex tumors such as lung cancer. However, the broader clinical implementation of carbon ion therapy for thoracic tumors is limited by several physiological and technological challenges.

A major limitation arises from the intrinsic sensitivity of carbon ion range to density variations and tissue inhomogeneities within the lung. Respiratory motion introduces significant intra-fractional movement which, combined with the motion of actively scanned particle beams, produces the so-called interplay effect. In addition, the heterogeneous structure of lung tissue induces energy and range straggling of the particles. This phenomenon, known as lung modulation, leads to a broadening of the sharp depth–dose distribution of carbon ions. Both the interplay and lung modulation effects can potentially compromise treatment quality.

Dose conformity can also be improved through optimization of beam angles, which benefits significantly from full 360 degrees beam flexibility. In clinical practice, such flexibility is achieved using a rotating gantry that allows the beam to be delivered from multiple directions around the patient. However, the technological complexity and high cost of gantries, particularly large for heavy ions, limit their widespread clinical adoption.

This thesis investigates the radiobiological, clinical, and technological aspects of carbon ion therapy for lung cancer, addressing key uncertainties related to treatment efficacy and delivery optimization. For comprehensive characterization of lung modulation, the radiobiological effect of carbon ion dose modulation was studied in lung fibroblast survival experiments and simulated with an in-house research version of a treatment planning system. A lower cell survival trend at the distal fall-off of the dose distribution was observed and reproduced in simulations.

The impact of lung tissue inhomogeneities was further investigated both independently and in combination with the interplay effect in patient-like scenarios. A retrospective treatment planning analysis on a cohort of lung cancer patients showed that while tissue heterogeneities introduce systematic dose modulation, their clinical impact remains small compared to motion-induced uncertainties. Notably, lung modulation partially mitigates interplay-related degradation.

Upright therapy was investigated as a gantry-less solution that enables full beam angle flexibility with a fixed horizontal beamline. A framework was developed to robustly compare supine and upright treatments. The results demonstrated equivalent plan quality, and the clinical benefit of 360 degrees angle rotation which can be provided by upright therapy without the need for a gantry. These results indicate upright therapy as a cost-effective alternative to gantry-based carbon ions treatments of lung cancer.

Zusammenfassung

In der Strahlentherapie ist eine konforme Dosisverteilung entscheidend, um die Toxizität in kritischen Organen zu minimieren. Die Teilchentherapie bietet aufgrund der präzisen Energiedeposition geladener Teilchen das Potenzial für eine hochkonforme Dosisapplikation. Kohlenstoffionen weisen zudem eine erhöhte radiobiologische Wirksamkeit auf und die Kohlenstoffionentherapie stellt daher eine vielversprechende Behandlungsmethode für komplexe Tumoren wie Lungenkrebs dar. Die breitere klinische Anwendung der Kohlenstoffionentherapie bei thorakalen Tumoren ist jedoch durch mehrere physiologische und technologische Herausforderungen eingeschränkt. Eine wesentliche Einschränkung ergibt sich aus der Empfindlichkeit der Reichweite von Kohlenstoffionen gegenüber Dichtevariationen und Gewebeinhomogenitäten innerhalb der Lunge. Die heterogene Struktur des Lungengewebes verursacht Energie- und Reichweitenstraggling der Teilchen. Dieses Phänomen, bekannt als Lungenmodulation, führt zu einer Verbreiterung der ansonsten scharfen Tiefendosisverteilung von Kohlenstoffionen. Des Weiteren verursachen Atembewegungen erhebliche intrafraktionelle Verschiebungen, die in Kombination mit der Bewegung aktiv gescannter Teilchenstrahlen zum sogenannten Interplay-Effekt führen. Sowohl der Interplay-Effekt als auch die Lungenmodulation können die Behandlungsqualität potenziell beeinträchtigen.

Die Dosiskonformität kann durch die Optimierung der Bestrahlungswinkel verbessert werden, welche erheblich von einer vollständigen 360-Grad-Strahlflexibilität profitiert. In der klinischen Praxis wird eine solche Flexibilität durch den Einsatz einer rotierenden Gantry erreicht, die eine Bestrahlung aus mehreren Richtungen um den Patienten herum ermöglicht. Die technologische Komplexität und die hohen Kosten von Gantrys, insbesondere für schwere Ionen, begrenzen jedoch die breitere klinische Anwendung.

Diese Arbeit untersucht radiobiologische, klinische und technologische Aspekte der Kohlenstoffionentherapie bei Lungenkrebs und thematisiert die Unsicherheiten hinsichtlich der Behandlungseffektivität und der Optimierung der Therapiedurchführung. Zur umfassenden Charakterisierung der Lungenmodulation wurde der radiobiologische Effekt der Modulation der Kohlenstoffionendosis in Überlebensexperimenten mit Lungenfibroblasten untersucht und mithilfe einer institutseigenen Version eines Bestrahlungsplanungssystems simuliert. Dabei wurde ein Trend zu geringerer Zellüberlebensrate im distalen Abfall der Dosisverteilung beobachtet, der in den Simulationen reproduziert werden konnte.

Der Einfluss von Gewebeinhomogenitäten der Lunge wurde anschließend sowohl isoliert als auch in Kombination mit dem Interplay-Effekt in patientenähnlichen Szenarien untersucht. Eine retrospektive Bestrahlungsplanungsanalyse an einer Kohorte von Lungenkrebspatienten zeigte, dass Gewebeinhomogenitäten zwar eine systematische Dosismodulation verursachen, ihr klinischer Einfluss jedoch im Vergleich zu bewegungsbedingten Unsicherheiten gering bleibt. Interessanterweise kann die durch den Interplay-Effekt verursachte Degradation teilweise durch die Lungenmodulation kompensiert werden.

Darüber hinaus wurde die aufrechte Therapie als Lösung ohne Abhängigkeit von einer Gantry untersucht, die eine vollständige Bestrahlungswinkel-Flexibilität mit einer festen horizontalen Strahlführung ermöglicht. Es wurde eine Struktur entwickelt, um Behandlungen in Rückenlage und in aufrechter Position robust zu vergleichen. Die Ergebnisse zeigen eine gleichwertige Planqualität sowie den klinischen Vorteil einer 360-Grad-Strahlwinkelrotation, die durch die aufrechte Therapie ohne Einsatz einer Gantry erreicht werden kann. Diese Ergebnisse unterstützen die Annahme, dass die aufrechte Therapie eine kosteneffiziente Alternative zu gantrybasierten Kohlenstoffionenbehandlungen bei Lungenkrebs darstellt.

Contents

1 Motivation and scope of this work

1.1 Lung cancer

Lung cancer remains one of the major causes of cancer death globally, with about 2.5 million new cases and 1.9 million deaths in 2022 (latest completed, globally verified dataset) according to the Global Cancer Observatory of International Agency for Research on Cancer (IARC) [1]. The disease accounts for approximately 12–13 % of all cancer diagnoses and nearly one in five cancer deaths worldwide. Non-Small Cell Lung Cancer (NSCLC) represents 85% of the total malignant lung tumors, it includes subtypes such as adenocarcinoma and squamous cell carcinoma. Its management is challenging because many patients are diagnosed at a late stage, when the disease is already locally advanced or metastatic, limiting curative options. In addition, NSCLC can exhibit radioresistance and molecular heterogeneity, which can reduce treatment effectiveness and contribute to relapse and progression [2]. However, NSCLC is characterized by growth and spread usually slower than Small Cell Lung Cancer (SCLC). Therefore, NSCLC treatments are more effective and lead to an overall better long-term survival [3]. In the last decades, several treatment modalities have been developed for NSCLC patients, improving the survival rate thanks to the combination of earlier cancer detection as well as increasing treatment options such as chemotherapy, immunotherapy, targeted treatments and radiotherapy.

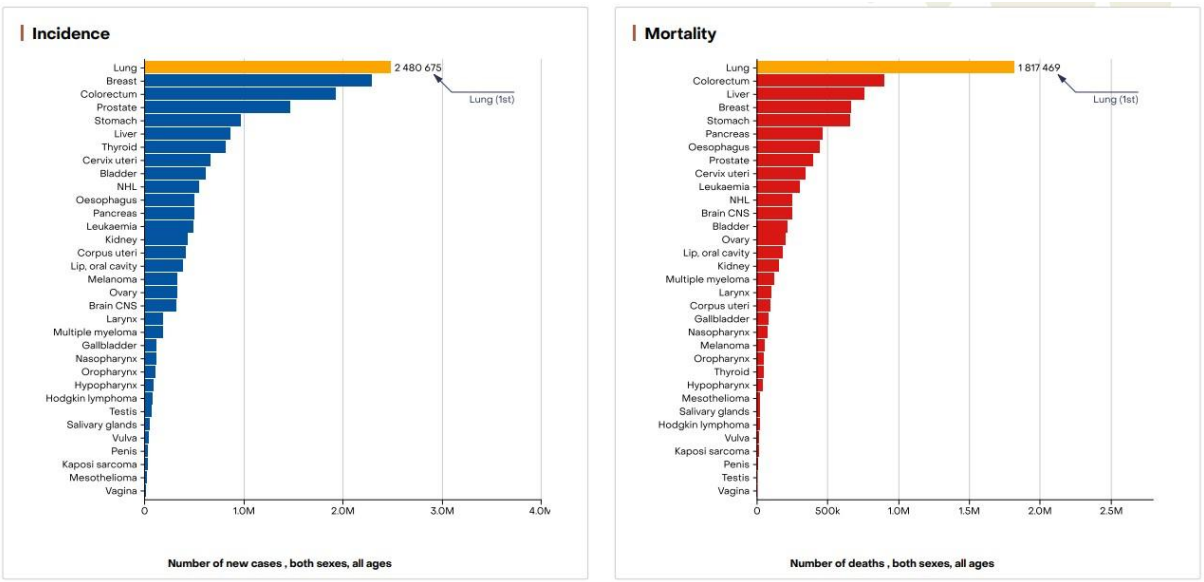

Figure 1.1 Global comparison of cancer incidence and mortality in 2022, for both sexes and all ages. The total new cases (left) and total deaths (right) are displayed per cancer type. Lung cancer accounts for the largest number of diagnoses and fatalities worldwide. Figure from [1].

1.2 Radiotherapy

Radiotherapy is a key component of modern cancer care. It is estimated that around half of all cancer patients will require radiotherapy at some stage of their illness, whether as part of curative treatment, in combination with surgery or systemic therapy, or for palliative care [4].

Radiotherapy treatments are based on damages that ionizing radiation induce to the deoxyribonucleic acid (DNA) of tumor cells, impairing their ability to reproduce and survive [5]. The main goal of radiotherapy is to increase tumor

control while sparing the surrounding critical organs at risk (OARs) and minimizing normal tissue complication probability.

In NSCLC patients the tumor is close to critical OARs such as the healthy lung, heart, and esophagus. Together with a direct damage to these organs the radiation-induced lymphopenia (RIL) is a severe and common side effect of radiotherapy for lung cancer patients. It is caused by the high sensitivity of lymphocytes to radiation, and it often leads to poorer overall survival and lower effectiveness of concurrent immunotherapy [6]. RIL is correlated with high doses to the heart, lung, and thoracic vertebrae. In addition, excess heart doses can result in critical heart failure after treatment and high doses to the base of the heart are correlated with lower survival [7]. Therefore, merely escalating the tumor dose, while improving local control, can highly impair survival [8], and dose conformity and precision become critical aspects of radiotherapy.

Among the available treatment methods for NSCLC, radiotherapy is considered a mainstay option. Still, the prognosis for lung cancer patients remains poor, and the increased cure rate is still unsatisfactory. Conventional radiotherapy with photons lacks the conformity required to safely escalate tumor doses with required OAR sparing. Ionizing radiation is a recognized risk factor for cancer, but this cannot limit the use of radiotherapy when indicated [9].

1.3 Carbon ion therapy for lung cancer

Compared with photons which produce the maximum dose at a shallow depth with slow exponential decrease after this maximum, charged particles, exhibit an inverse depth-dose profile, with characteristic sharp dose deposition and high peak-to-entrance dose ratio. This makes particle therapy an advanced form of radiotherapy [10], that combines enhanced tumor control with a decreased normal tissue toxicity [11].

Proton therapy has been widely adopted and over the last decades has become the main form of particle therapy [12]. However, for heavier ions, such as carbon ions, the even sharper dose deposition is coupled with a higher biological effectiveness. The radio-biological properties of carbon ions increase the damage to malignant cells, while their favorable dose deposition improves the sparing of healthy tissues [10].

These unique characteristics make carbon ion radiation therapy (CIRT) a promising treatment solution for radioresistant, metastatic and complex tumors such as NSCLC. Nevertheless, CIRT advantages can be fully exploited only if the precision of the dose distribution can actually be delivered to the tumor, which requires accurate and precise control over the beam range inside the patient. For tumors located in the lung, this is impaired by internal anatomical motion and lung tissue inhomogeneities, which degrade the final dose distribution, compromising both the tumor control and the OARs sparing [13], [14]. To mitigate this, precise modelling of the treatment dose inside the patient is mandatory.

Furthermore, best sparing of OARs also requires flexibility to select the most suitable beam angles for each patient. Yet CIRT gantries are rare and associated with significant challenges in construction and maintenance. These technological hurdles are significantly increased for heavy ion beams compared to proton beams [15].

The valuable advantages of CIRT, requiring maximum delivery precision, are penalized in NSCLC patients by anatomical and physiological features of the lung as well as technological challenges of the beam delivery system. Thus, to permit a significant spread of CIRT, the actual clinical impact of motion and lung inhomogeneities needs to be thoroughly investigated in gantry-based treatments together with advanced gantry-less therapy solutions, such as upright therapy.

1.4 Scope of this work

This thesis is situated within the multidisciplinary research field of CIRT for the treatment of NSCLC. It focuses on addressing the inherent anatomical and physiological complexities of lung radiotherapy, while also exploring upright radiation therapy as an advanced gantry-less technique, evaluating its potential clinical benefits for thoracic tumor sites.

Four research hypotheses, defining the scope of this thesis, are presented here.

1.4.1 Clinical impact of lung modulation and anatomical motion on carbon therapy of lung cancer

The anatomic motion of the lung region, due to breathing and heartbeat, affects both the tumor target and the surrounding OARs. Its dosimetric impact has been well studied and can be attributed to both the interference of beam and tissue motion, the so-called interplay effect, as well as motion-induced range changes in the heterogeneous tissue. Depending on the tumor location and motion amplitude, the dose degradation can be quite severe. Especially the interplay effect is known to be highly random and thus can be averaged out by repeated uncorrelated dose application [16], [17].
A second, less well explored aspect is the modulation of the sharp Bragg Peak (BP) in the microscopically heterogeneous lung tissue, which is not properly resolved in clinical CTs. While previous studies have shown that the magnitude of its impact on the target dose might be smaller than that of anatomical motion, this effect is systematic and will not be affected by repeated applications.
No study to date has systematically investigated both effects in conjunction, to quantify and evaluate their clinical relevance and impact.

The first aim of this thesis is to investigate the radiobiological effect of lung tissue inhomogeneities on carbon ion beams, through cell survival experiments and dosimetric simulations. To that end, the TRiP4D dose calculation engine makes it possible for the first time to assess the combined clinical impact of interplay and lung modulation effects.

Hypothesis I:
The effect of lung tissue inhomogeneities on carbon ions and its radio biological impact can be reproduced and investigated in cell survival experiments.

Hypothesis II:
Interplay and lung modulation effect can be comprehensively investigated through treatment planning studies, and their superposition will lead to clinically relevant dosimetric effects beyond the state of knowledge.

1.4.2 Upright and supine carbon therapy of lung cancer: a 4D dosimetric study

The second aim of this thesis is to investigate the potential use of upright positioning in CIRT to both greatly enhance the clinical applicability of existing installations and also show the rationale for novel, dedicated upright therapy centers. Most of the existing CIRT beamlines are fixed to either a horizontal or vertical beam direction, which greatly reduces their clinical value especially for lung cancer therapy. Retrofitting treatment chairs to these beamlines could be a cost-effective alternative to building new centers with the very large gantries necessary for CIRT.

While upright NSCLC therapy looks like a promising option especially for CIRT, the clinical experience almost exclusively results from treating supine patients. A framework to compare both modalities is therefore an essential basis to thoroughly investigate upright therapy as a novel treatment option.

Hypothesis III:
Clinical experience from supine therapy can be translated to upright therapy through a treatment planning study framework, which can show that upright therapy is non-inferior to supine therapy.

Hypothesis IV:
Lung cancer therapy also with carbon ions greatly benefits from a flexible beam angle arrangement, and it can be shown that upright patient positioning can provide this benefit.

1.5 Outline

Chapter 2 describes the principles of particle therapy, focusing on the physical and radiobiological characteristics of carbon ions in the context of lung tumor-specific challenges, namely internal tissue motion and tissue inhomogeneities. Gantry-based treatment deliveries are also described, and upright therapy is introduced as an advanced gantry-less solution for CIRT.
Chapter 3 provides a comprehensive overview of the methods used in this work, focusing on treatment planning optimization and dose calculation algorithms as implemented in the GSI treatment planning system (TPS) TRiP98 and its advanced version TRiP4D.
In Chapter 4, cell survival experiments, performed to describe the carbon ion radiobiological effect in the presence of lung tissue heterogeneities, are introduced. In addition, a treatment planning study is presented to assess the clinical impact of motion and tissue inhomogeneities, both individually and in combination.
The clinical impact of upright therapy is investigated in Chapter 5 with a treatment planning study. A framework to study 3D and 4D dose distributions was developed to robustly compare the clinical outcome of upright radiotherapy with standard supine treatments.

2 Particle therapy of lung cancer

2.1 Particle therapy

Particle therapy is an advanced form of external beam radiotherapy that uses charged particles, such as protons or heavy ions, to damage cancer cells while sparing the healthy tissue as much as possible. The physical characteristics of particle interaction with matter, different from those of photons, are exploited to deliver a high radiation dose at a specific depth in the body. For particles heavier than protons, such as carbon ions, together with the superior spatial precision, an increased radio-biological effectiveness is achieved. This makes CIRT a promising radiotherapy treatment for radio-resistant and deep-seated cancers, like thoracic and abdominal tumors. The treatment of tumors located in the chest or abdomen is challenged by the motion of internal tissues, which makes the application of scanned ion beam therapy more complex. The high curative potential of scanned ion beam therapy is coupled with complex and expensive technology that requires highly specialized equipment. Therefore, ongoing research aims to make the treatment more affordable and widely available.
In this section, the fundamentals of particle therapy are introduced, with a focus on the physical and radiobiological aspects as well as the beam delivery techniques.

2.1.1 Ionizing radiation

Ionizing radiation is defined as radiation transporting sufficient energy to remove bound electrons from atoms, resulting in the formation of ions. Ionizing radiation includes both charged particles (e.g., ions and electrons) and uncharged particles such as neutrons and photons (X-rays and gamma rays). Ionizing radiation transfers enough energy to break chemical bonds and ionize atoms and molecules within the irradiated medium. Chemical and biological effects, particularly relevant in radiobiological contexts, derive from these primary physical interactions.

The fundamental physical quantity used to define the energy released into matter by ionizing radiation is the absorbed dose (D), namely the ratio of the incremental energy dE deposited by the radiation to the corresponding mass unit dm of the target material:

$$D = \frac{dE}{dm}\ [1Gy = 1J/Kg] \quad (2.1)$$

In the following, the interaction mechanisms of photons, protons and ions with matter are described.

Photons

Photon interaction with matter occurs through three fundamental mechanisms: photoelectric effect, Compton scattering and pair production. Photons traversing the material interact with atomic electrons and ionize it through secondary electromagnetic interactions.

The attenuation of a photon beam is described as an exponential decay by the Lambert-Beer Law:

$$I(x) = I_0 exp(-\mu x) \quad (2.2)$$

It describes the dependency of the photon beam intensity at depth x, I(x), on the initial intensity I_0, and on the linear attenuation coefficient μ, a material and photon energy specific parameter.

The dose deposition profile of photons along the beam axis exhibits a characteristic build-up region, deriving from the interaction of secondary electrons and their increasing deposited dose. After a maximum is reached the dose decreases exponentially in depth (see Figure 2.*2*a).
In conventional photon radiation therapy, electrons in the energy range of 4-25 MeV are generated by linear accelerators and converted into photons in a broad spectrum of Bremsstrahlung. Because of the electron build-up, most dose is released before the target, and relevant doses also occur distal to the tumor volume. As a result, the dose conformality of photon therapy can only be achieved by cross-firing multiple beams or applying continuous arcs, making a gantry, or an upright positioning system, essential. The high dose to normal tissues surrounding the target has been significantly reduced by modern delivery techniques such as volumetric arc therapy, but large volumes of low to mid dose levels are unavoidable.

Ions

Charged particles mainly interact with matter through Coulomb scattering with the electrons of the traversed medium. Unlike photons, which exhibit a sparser energy deposition, ions continuously deposit energy along their path, emitting more lower-energy secondary electrons (δ-electrons) that cause a denser track of further ionizations.

The average energy loss (-dE) per unit path length (dx), called Stopping Power, is described by the Bethe equation:

$$-\frac{dE}{dx} = 4\pi \frac{e^4 Z_p^2}{m_e v^2} \frac{N_a Z_t \rho_t}{A_t} \left[l\,n\ \left(\frac{2m_e v^2}{\langle I \rangle}\right) - \left(1 - \frac{v^2}{c^2}\right) - \frac{v^2}{c^2} - \frac{C}{Z_t} - \frac{\delta}{2} \right] \quad (2.3)$$

where v and Z_p are the velocity and charge of the particle, Z_t, A_t, ρ_t, and ⟨I⟩ represent the atomic number, atomic mass, density, and mean ionization potential of the target; and m_e, e, and c are the electron mass, elementary charge, and speed of light, respectively. The formula is given in the relativistic version, including the shell correction term $\frac{C}{Z_t}$ and the density effect correction term $\frac{\delta}{2}$ [18]. The energy loss formulated in Equation 2.3 describes a very sharp dose deposition at the end of particles' range, known as the Bragg peak (BP). For an ion beam consisting of many particles, the statistical fluctuations of the energy loss in the medium result in a broadening of the BP. For many collisions the fluctuations are described by a Gaussian distribution, and a range straggling is associated with the variance of the energy loss straggling.
The Stopping Power is equivalent to the Linear Energy Transfer (LET) if the average energy deposited to the medium locally around the primary track is considered. Notably, the LET strongly depends on the particle charge (Z_p) and its velocity v, increasing proportionally to the charge and inversely to the particle velocity. The LET describes the ionization density that is typical of each type of radiation. Radiations can be divided into low-LET and high-LET, depending on the density of ionization events. Low-LET radiation, such as photons or electrons, are characterized by a mean distance between two ionization events of 100 nm, while this value is in the order of few nm for high-LET radiations, like carbon ions. The increased ionization density makes high-LET particles responsible for more severe damage to the traversed tissue [19].

The absorbed dose (D_{abs}) produced by particle interaction with matter can be related to the LET and the particle fluence (F) through the following formula:

$$D_{abs}[Gy] = 1.602 \cdot 10^{-9} \cdot F\left[\frac{1}{cm^2}\right] \cdot LET\left[\frac{keV}{\mu m}\right] \cdot \frac{1}{\rho}\left[\frac{cm^3}{g}\right] \quad (2.4)$$

Particles undergo a gradual energy loss along their path while their velocity is high, leading to a peak of energy deposition for the stopping particles at the end of their range, namely the BP. After the BP, the dose deposition

rapidly falls off, with only a small residual dose deriving from the statistical nature of particle range (Figure 2.*2*a). The final penetration depth, and the consequent BP position, depend on the initial beam energy and the stopping power of the medium. In clinical applications, multiple BPs with different initial energies are superimposed to create the so-called Spread-Out Bragg Peak (SOBP), with which the target volume is evenly covered in depth (see section 2.1.3 Beam delivery)**2.1.3 Beam delivery**.

Together with electromagnetic interactions, ions heavier than protons also interact with target nuclei, leading to fragmentation of both the projectile and the nuclei. The produced fragments travel in the medium as secondary charged particles with, in part, longer range and altered dose distribution. The probability of nuclear interactions increases with the geometrical cross section of the ion, and it results in a fragmentation tail depositing dose after the BP fall-off [20]. In the lateral direction, instead, the beam broadening is caused by elastic and inelastic nuclear scattering, which is more pronounced for lighter ions, such as protons [21] (Figure 2.*2*b).

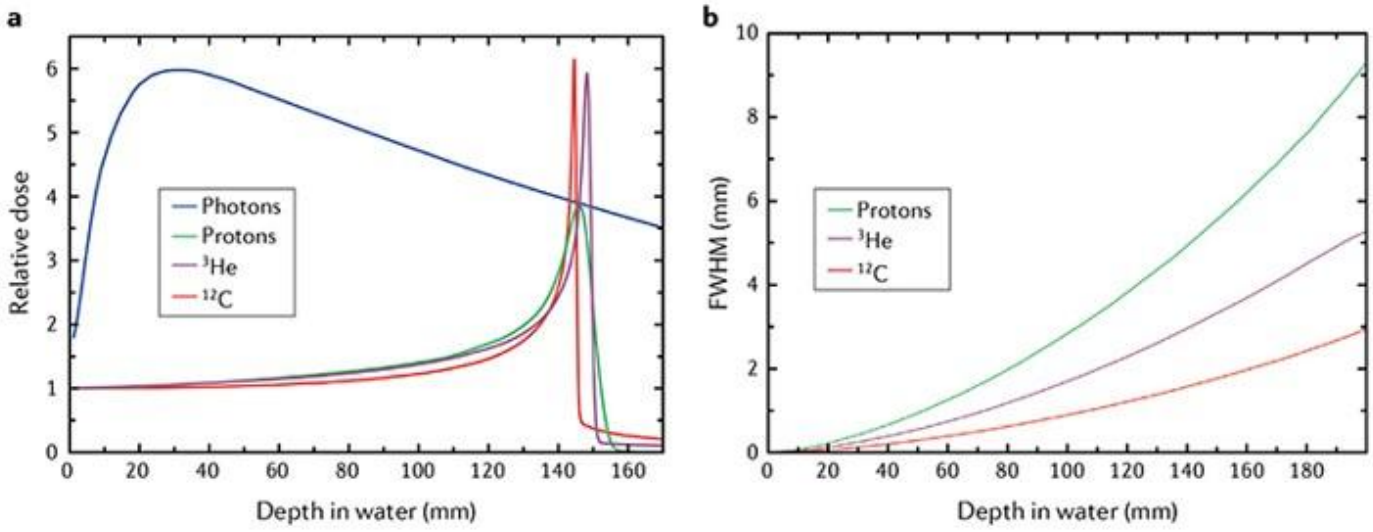

Figure 2.2. Depth-dose distributions showing the X-ray dose deposition, the Bragg Peak for different ions and the reduced straggling of heavier ions (a). The lateral broadening (full width at half maximum (FWHM)) of the same ions is shown (b). Figure from [21].

The described depth-dose profile of charged particles, characterized by low entrance dose, minimal exit dose and maximum energy deposition at a well-defined depth, allows for highly conformal dose distributions. Because of their physical properties, protons and carbon ions are a powerful tool for the treatment of complex tumors, able to provide optimal sparing of healthy tissues.

The effectiveness of particle therapy strongly depends on how the deposited energy translates into biological damage at cellular and subcellular level. Therefore, the understanding of the radiobiological mechanisms is paramount to define why particles allow for a superior clinical outcome.

2.1.2 Radiobiology

The goal of radiotherapy is to permanently damage tumor cells, by inducing damage to the DNA. Ionizing radiation causes direct damage via the secondary electrons, that break the DNA molecular bonds, and indirect damage through the production of reactive oxygen species (ROS), able to chemically modify the DNA. When complex DNA damage, such as multiple associated double-strand breaks (DSBs) occur, the cell undergoes apoptosis or loses its ability to divide [22].

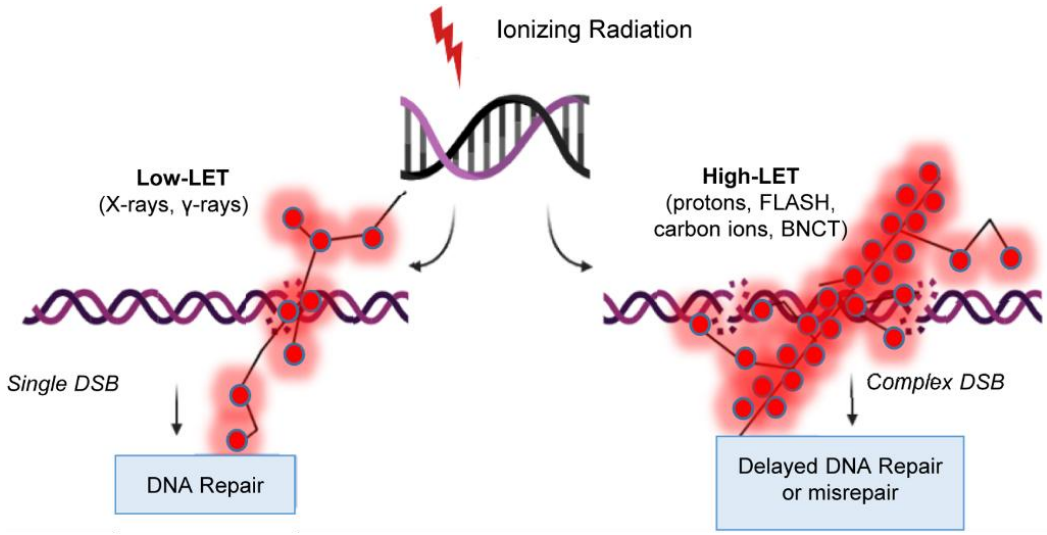

Figure 2.3 DSBs repair after low- and high-LET radiation. Adapted from [23].

The likelihood of lethal DNA damages increases with dose and high-LET particles, as shown in Figure 2.*3*. On a microscopic scale, the interaction of particles in the volume around the DNA follows a Poisson distribution. The probability of cell survival decreases exponentially with the dose and can be approximated with the Linear-Quadratic (LQ) model:

$$S = exp(-\alpha D - \beta D^2) \quad (2.5)$$

The linear component is described by the coefficient α [Gy−1] accounting for damages that the cell is not able to repair. The total fraction of surviving cells is then described by the term e−αD. The quadratic component, described by the coefficient β [Gy^{-2}], considers sub-lethal events that become lethal only when combined. In this case the fraction of surviving cells is defined by $e^{-\beta D^2}$. These two mechanisms are independent, and the complete model formulation is given by the product of the two surviving cell fractions [24], [25]. The linear and quadratic components depend on tissue and radiation type. Tissue radiosensitivity is described by the α/β ratio, which quantifies the ability of cells to repair after irradiation. Cell lines characterized by low α/β are more radioresistant, while higher α/β values describe larger radiosensitivity. High-LET radiations, because of the dense track structure, can cause complex DNA damage through single particle direct interactions. This enables them to produce an enhanced total radiobiological effectiveness with respect to low-LET radiations. This is quantified via the relative biological effectiveness (RBE), defined as:

$$RBE = \frac{D_{photon}}{D_{ion}}|_{Iso-effect} \quad (2.6)$$

where D_{photon} and D_{ion} are the doses necessary to achieve the same survival value, for different tissue types or radiation qualities (see Figure 2.*4*). A constant RBE of 1.1 is conventionally assigned to protons, while carbon ions RBE ranges from 2 to 5, depending on the tissue and particle LET [26], [27].

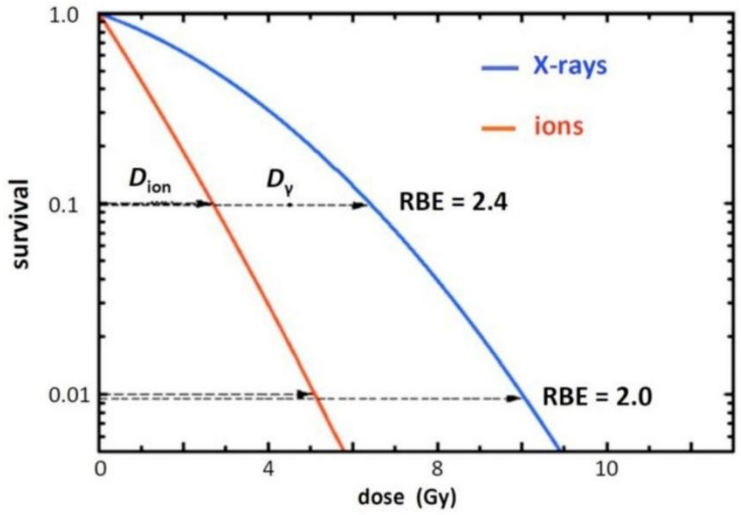

Figure 2.4 RBE values calculation from survival curves for X-rays (blue) and carbon ions (red). Figure from [28].

The superior radio-biological damage caused by heavy particles make them more effective in the treatment of radio-resistant tumors, achieving higher tumor control. However, increasing the particle mass is associated with a higher risk of toxicity in healthy tissues, particularly at the depth of the fragmentation tail for carbon ions but also at the entrance channel for very heavy ions, such as Neon or Argon. Carbon ions are considered an optimal compromise, balancing therapeutic advantage with acceptable normal tissue risk, while also preventing an excessive increase in technological challenges posed by the use of heavier particles [29].

The described physical and radiobiological characteristics of particles need to be implemented in TPS, and comprehensive biophysical models, like the Local Effect Model (LEM) [30], are used for these purposes. The LEM describes tissue specific responses to particle irradiation by calculating the RBE distribution, considering both LET and tissue characteristics variations along the beam path. Therefore, the RBE-weighted dose (D_{bio}) can be calculated in TPS as follows:

$$D_{bio}[Gy(RBE)] = D_{abs}(F,\ LET) \cdot RBE(F, LET, Z, cell) \quad (2.7)$$

In this way, physical and radio-biological characteristics are integrated into the treatment plan (see section 3.4 Plan optimization) [31].

Equation 2.7 shows the dependencies of radiobiological quantities (D_{bio}, RBE) from the physical quantities (D_{abs}, LET). A more detailed description is shown in Figure 2.*5*. LET and RBE distributions of different particles are shown relative to the optimized D_{bio}. The RBE increases along the beam path following the LET variations and its profile reaches a maximum at the target distal fall-off due to the combination of high LET values and low doses. Notably, the RBE non-uniformity inside the target depends on the tumor and normal tissue radiosensitivity (expressed by α/β). The LET and RBE magnitude increases for heavy particles, although the highest RBE peak occurs for protons, because of the extremely low doses at the target distal end [32].

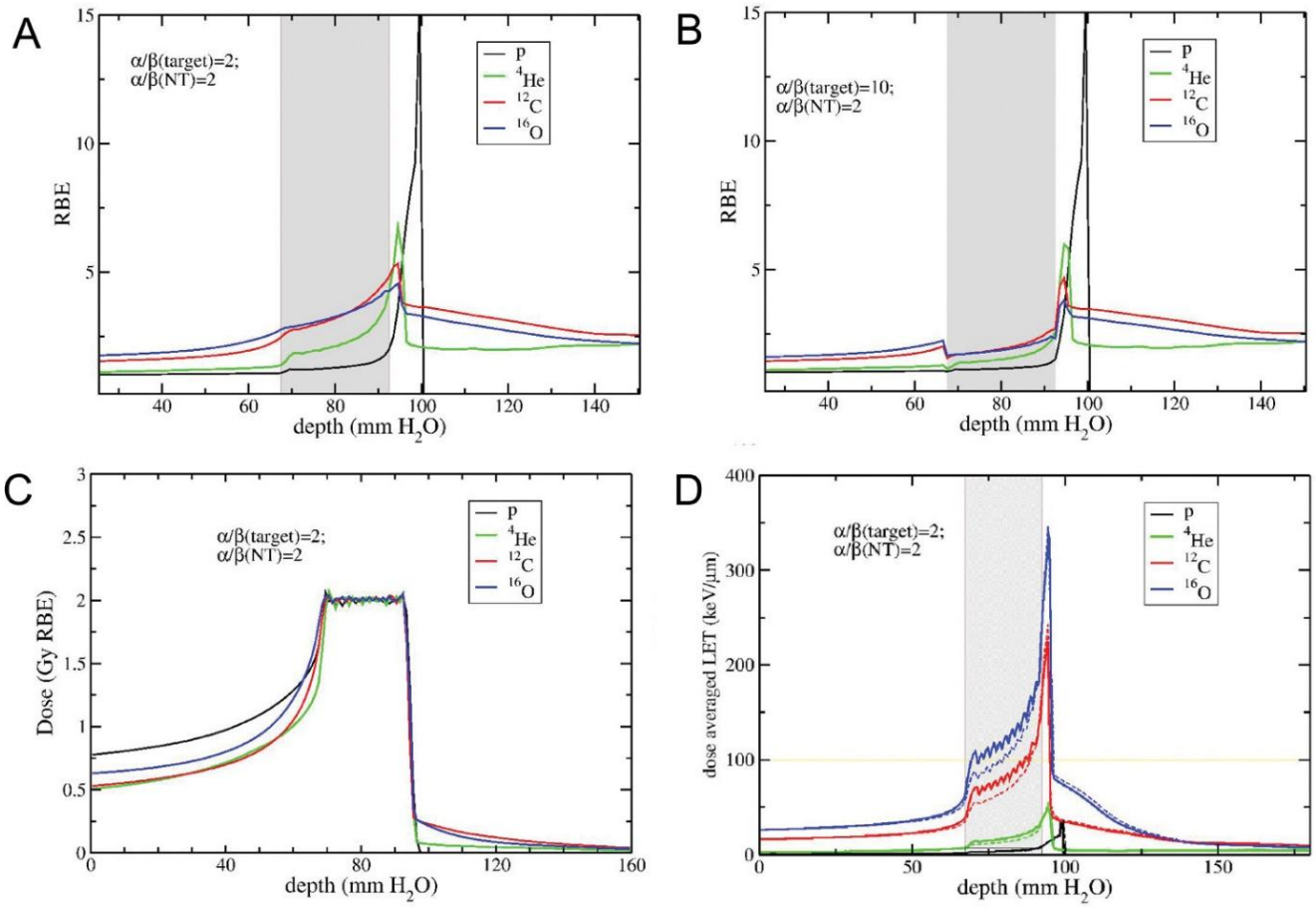

Figure 2.5 Dose, RBE and dose averaged LET distribution of different particles. The RBE (a,b) profiles are shown with respect to the target (grey area). The RBE distribution is calculated for two scenarios with uniform α/β of 2 for target and normal tissue (NT) (a), and α/β of 10 assigned to the target (b). RBE-weighted dose optimized on the target (c) and dose averaged LET for the uniform α/β scenario (d) are shown. The RBE is not constant inside the target, because of the variable LET. The same trend occurs for the healthy tissue before the target. At the distal fall-off all RBE lines exhibit a peak deriving from the combination of high LET and low doses. This is especially pronounced for protons and can be explained with very low local doses behind the tumor (d). Figure modified from [32].

A comprehensive understanding of the radiobiological mechanisms is fundamental to maximise the clinical benefit of particle therapy. For example, the difference in radiobiological sensitivity of healthy and malignant tissues is the basis of treatment fractionation.

Fractionation in radiotherapy

The delivery of radiotherapy treatments in multiple fractions, instead of a single session, is a strategy with both biological and technical rationales.

Normal tissue cells, characterized by low α/β, can repair sub-lethal damage between treatment fractions. An increased killing effect would occur in normal tissues for higher single doses, while the malignant cells, characterized by high α/β, are not directly affected by fractionation.

From a technical perspective, fractionation helps to reduce delivery uncertainties such as positioning errors, anatomical changes and beam range variations. If the total dose is delivered in multiple sessions, these uncertainties

can be averaged out, and the overall treatment robustness and accuracy improves. With the usual fractionation scheme, 2 Gy are delivered per fraction in a total of 30 fractions [33].

The increased precision and effectiveness of CIRT, coupled with advanced techniques for image guidance, beam delivery precision and conformity, have opened the possibility of hypo-fractionated, or even single-fraction treatments. However, a small number of fractions also reduces biological and statistical safety and has to rely on the precision and conformity of dose delivery [34].

2.1.3 Beam delivery

A specialized accelerator technology is required for the production and the delivery of particle beams in clinical applications. Particle accelerators generate high energy particles and direct them towards the patient with sub-millimeter accuracy.

Particle accelerators provide a beam in the energy range of 60-250 MeV for protons and 120-430 MeV/u for carbon ions, able to reach tumors located up to 30 cm inside the patient's body. Particularly, cyclotrons are commonly used for protons, and they produce a continuous beam at fixed energy, whose range is varied through energy degraders. Synchrotrons, instead, are required for heavy ions, which are accelerated in discrete packages and then extracted in so-called spills. Each extraction is followed by a spill pause for re-acceleration and exploited for active energy variation between spills.

The beam delivery technique was initially based on passive beam shaping. A thin pencil beam (PB) was enlarged and adapted to the target volume using scatterers, range modulators and collimators. Despite being technically simpler, passive beam deliveries provide poor dose conformity, increasing the dose to proximal normal tissues.

The active scanning delivery technique, on the other hand, ensures a uniform dose across the entire tumor volume. The method, shown in Figure 2.*6*, is based on the division of the target in multiple iso energy slices (IESs), corresponding to different depths inside the patient geometry. In each IES, the beam is moved through a grid of points to cover the whole area. Dipole scanning magnets are used to scan single PB over the grid spots following a meander-like shape. A different number of particles is delivered to each spot following the optimized treatment plan to achieve the prescribed dose (see section 3.4 Plan optimization). The sharp pristine BPs, especially in the case of carbon beams, are broadened using ripple filters, and multiple energy layers are superimposed to form the SOBP [35], [36].

The active beam scanning system provides an extremely conformal dose deposition for targets of any shape and dimension. To further increase the delivery flexibility, these active systems are mounted on a rotating nozzle, the gantry, that allows the delivery of the beam from multiple directions. With this strategy, the total treatment dose is delivered to the target, while a better sparing of normal tissues is achieved [10].

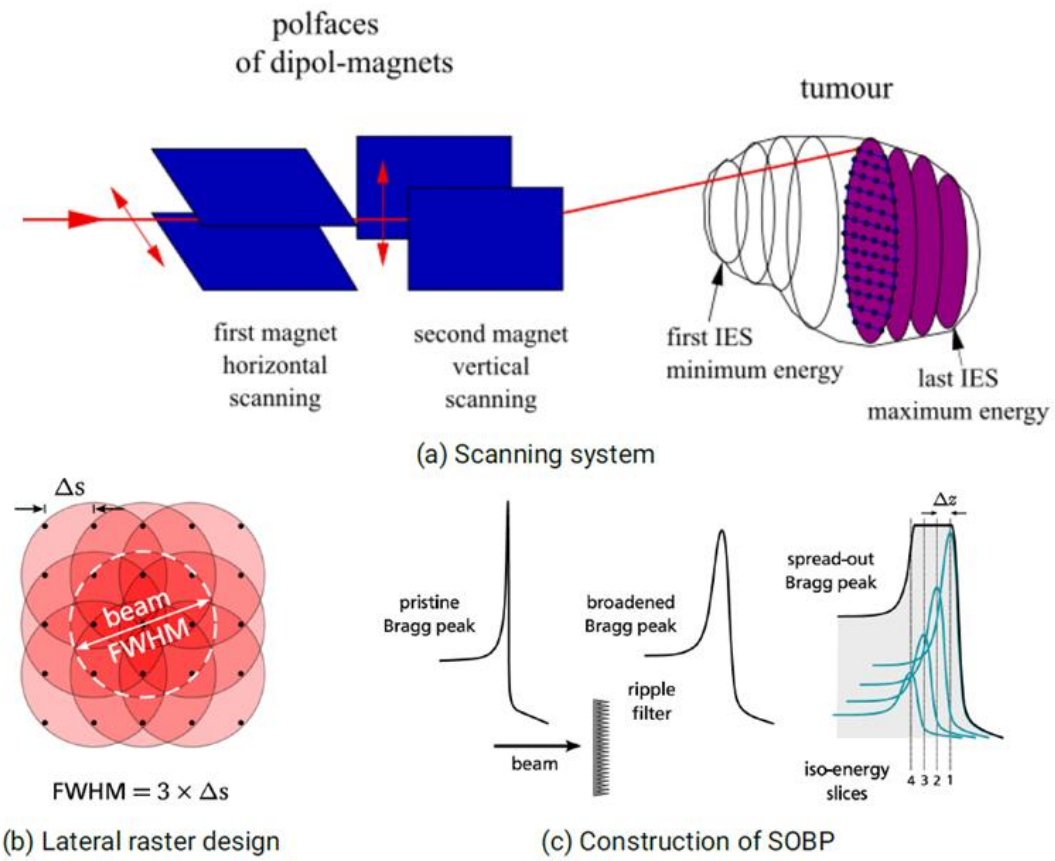

Figure 2.6. Active scanning delivery method in particle therapy. (a) Pencil beams (PBs) are deflected using scanning magnets. The volume is divided into iso-energy slices (IESs) that correspond to initial beam energies. A homogeneous dose distribution is achieved by overlapping single PBs (b) in lateral and (c) longitudinal direction. The beam weights are optimized to achieve the desired homogeneous spread-out Bragg peak (SOBP) as the sum of the single PBs. Figure (a) adapted from [37] with permission from Springer Nature and figures (b) and (c) from [38].

2.2 Tumor motion

The introduction of advanced particle therapy plans, and beam delivery strategies allows to maximize the therapy outcome, achieving highly conformal dose distributions. In principle, particle therapy is more conformal than photon therapy because of the BP, but its advantages are jeopardized if the range of particles cannot be precisely predicted inside the patient's body. Therefore, target motion, changing the density in the particle path, is a major challenge in radiotherapy, and it becomes critical in particle therapy.

2.2.1 Types of motion

Tumor motion can have multiple origins, both linked to treatment setup and patient anatomical changes. Setup and patient positioning errors represent a main cause of tumor misalignment and affect any treatment site. It is paramount to precisely and consistently position the patient at each fraction, to ensure high-quality treatment. The treatment plan is based on the patient geometry as it is described in the initial computed tomography (CT) image, and it is crucial to position the patient likewise at each beam delivery. To minimize these uncertainties, dedicated imaging techniques as well as positioning systems, able to provide high reproducibility, have to be employed.
Tumors located in the thorax and the abdomen are additionally subjected to anatomical motion, classified as follows:

Inter-fractional motion: it occurs on a time scale of days, between different fractions of the same treatment. Possible causes are gastrointestinal filling, bladder and rectal volume variations as well as treatment related changes such as weight loss and/or tumor shrinkage. These variations can affect the exact target position between fractions and adaptive plan strategies can be employed to maintain treatment quality [39].

Intra-fractional motion: it occurs on a time scale of seconds or minutes and takes place in the time span of a single fraction delivery. It arises from physiological mechanisms like breathing, heart beating, digestion. It mostly involves organs like lungs, liver, bowel and pancreas, in which a displacement up to 20 mm can occur mainly in the inferior-superior direction [40].

Tissue motion, independently of its origin, changes the density along the beam path producing unpredictable particle range changes and dose deposition in the patient's body.

2.2.2 Motion induced range changes

In particle therapy, tissue density variations are a main critical factor affecting the beam range and the resulting dose accuracy. The sharp BP makes particles highly sensitive to even small tumor positional errors (Figure 2.7). The BP shifts from inside the target volume to the surrounding normal tissues causing both target underdosage and harmful irradiation of healthy tissues.

The treatment plan is optimized to achieve a conformal dose and is based on the anatomical information deriving from planning CT scans (see section 3.1 Diagnostic imaging in radiotherapy). Significant inter-fractional changes can occur between the planning CT acquisition and each fraction, and intra-fractional motions can further affect patient geometry during the delivery. Additional margins are applied to the malignant volume at the stage of treatment planning to account for any motion error and mitigate dose uncertainties. Different types of margins are described in detail in section 3.2 Volumes of interest.

Range changes are particularly critical in low-density regions, such as the lung, where large density gradients occur between the healthy tissue and the tumor. In addition, thoracic tumors are highly affected by intra-fractional motion, where superposition with the motion of the actively scanned beam causes the so-called interplay effect.

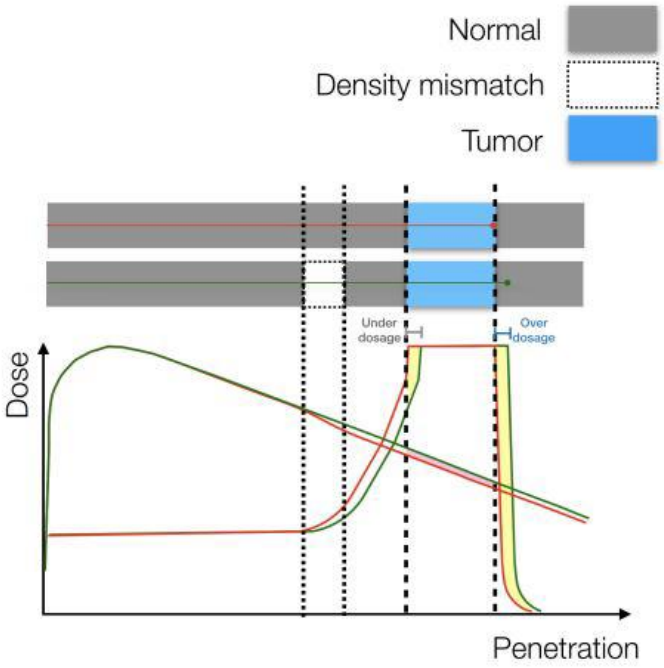

Figure 2.7 Effect of range variation on delivered dose. Planned dose (for photons and carbon ions) (red) and delivered dose (green) deriving from a density mismatch (white box) and leading to important local dose changes for particles (yellow area) [41].

2.2.3 Interplay effect

Active beam delivery systems provide extreme flexibility and dose conformity and have almost completely replaced passive systems. However, a critical hurdle derives from the dynamic interaction of beam motion and intra-fractional target motion. The dependency of the interplay effect on the scan path and the resulting heterogenous doses are shown in Figure 2.*8*. This effect strongly depends on the temporal correlation between the two motions, and without any synchronization strategy, the final dose distribution is unpredictable. Severe dose degradations can occur in a single fraction, but because of its random nature, the interplay effect averages out in multiple fractions [42].

It is possible to simulate multiple interplay dose distortions by correlating the start of the delivery with a different starting motion phase [43].

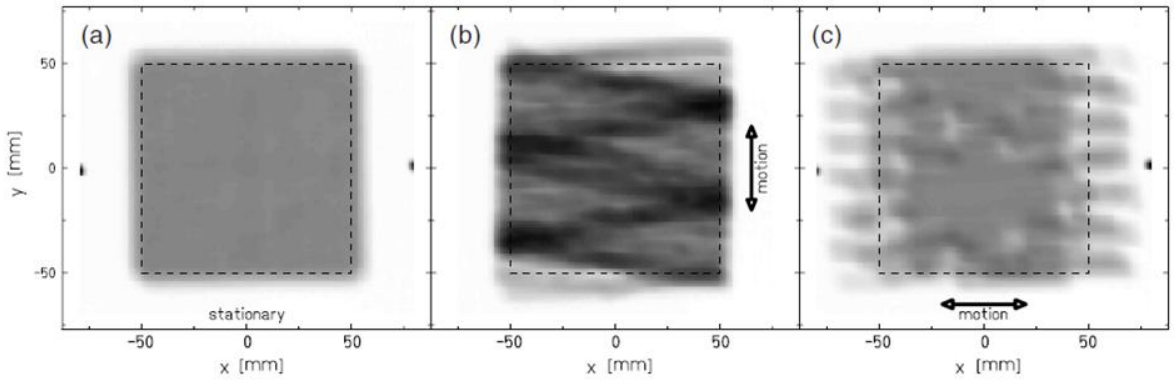

Figure 2.8 Interplay effect measured with a radiographic film. Same plan delivered with static (a), vertical (b) and horizontal (c) motion. Figure from [17]; permission conveyed through Copyright Clearance Center, Inc.

In addition to density gradients and physiological motions, the characteristic inhomogeneous structure of the lung is responsible for BP degradation resulting in the so-called lung modulation effect.

2.3 Lung tissue inhomogeneities

2.3.1 Lung anatomy

Human airway is a branching system that conducts air from the external environment to the lung with the main objective of gas exchange. Airway structure is divided into upper (nose, mouth, pharynx and larynx) and lower airway, depicted in Figure 2.*9*, including trachea, bronchi, bronchioles, and alveoli [44]. The lower airway represents the respiratory section.

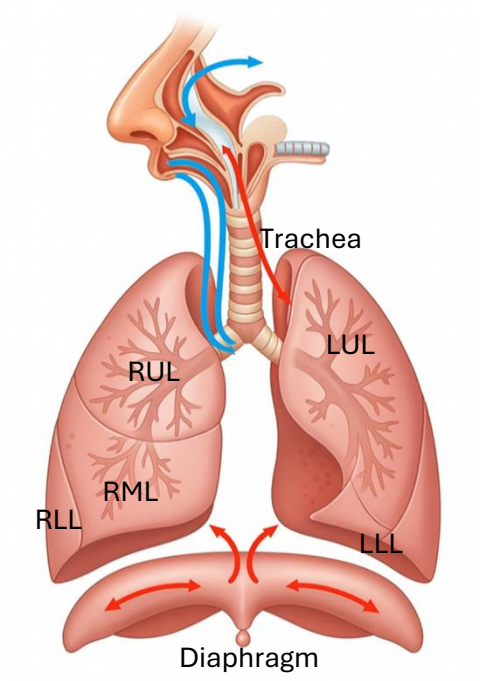

Figure 2.9 Schematic representation of the respiratory system. Trachea, diaphragm and lung lobes are labelled. Air flow in (red) and out (blue) of the system is shown with arrows. RUL=right upper lobe, RML=right middle lobe, RLL=right lower lobe, LUL=left upper lobe, LLL=left lower lobe. Figure from [45].

The trachea, first component of the respiratory section, divides into right and left main bronchi whose structural organization is comparable but not symmetrical. The right lung is divided in the right upper lobe (RUL), right middle lobe (RML), and right lower lobe (RLL). In contrast, the left lung is divided in left upper lobe (LUL) and left lower lobe (LLL). The oblique and horizontal fissures separate the three lobes in the right lung, the oblique fissure lies between the RML and RLL, while the horizontal fissure divides the RUL and RML. The left lung contains only an oblique fissure, which separates the LUL from the LLL. Figure 2.10 shows the anatomy of the respiratory section, going from the trachea to the alveolar sacs. After the trachea divides into the right and left lung, each subsequent division results in a progressively narrower but denser network of airways. The respiratory section is divided in 23 generations of which the first 16 represent the conducting zone, where air is transported but no gas exchange is performed. Gas to blood exchange occurs in the so-called respiratory zone (generation 17-23), that includes bronchioles and alveoli. The alveoli are air-filled structures with sub-mm diameter and length (see Figure 2.*10*).

Alveolar ducts and sacs are the main components of the respiratory zone, the functional tissue of the lungs, and constitute the lung parenchyma, representing up to 90% of the total lung volume. Therefore, a significant portion of lung volume is made of microstructures filled with air (density 1 mg/cm^3), surrounded by the interstitial tissue (density of ~1 g/cm^3), a dense network of cells and blood vessels [44].

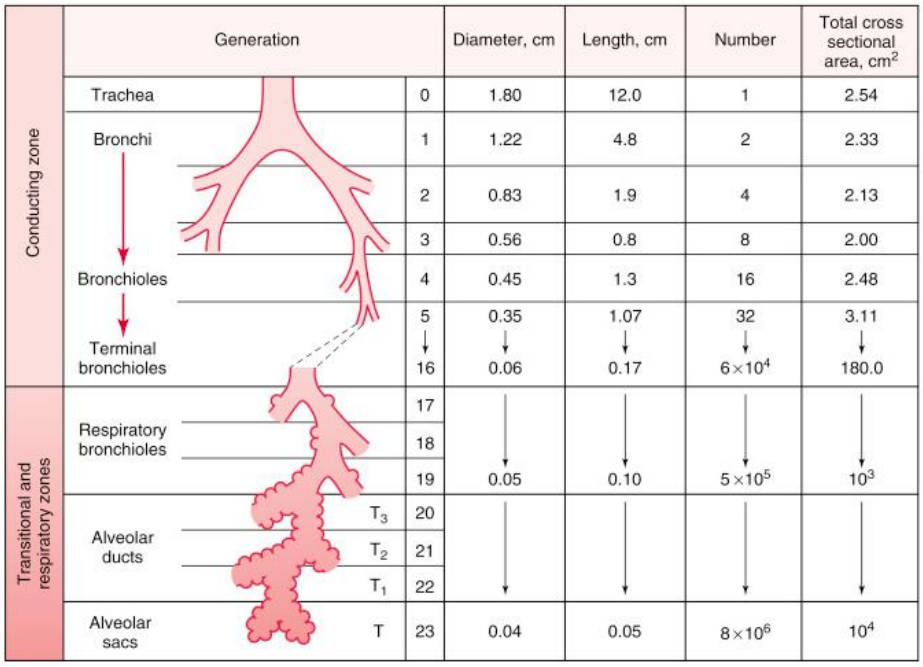

Figure 2.10 Lower air generations and their approximate dimensions. Figure from [44]; permission conveyed through Copyright Clearance Center, Inc.

The complex anatomical structure of lungs, with the coexistence of air and tissue, results in a highly heterogeneous material, that significantly influences particle interactions as they pass through it. Compared to homogenous materials, the energy deposition and the finite range of particles are subject to increased uncertainties, representing a possible cause of normal tissue toxicity in particle therapy treatments. Lung tissue inhomogeneities cause a characteristic BP degradation resulting in the so-called lung modulation effect.

In particle therapy applications, the sub-mm dimension of lung tissue inhomogeneities is not resolved in the clinical CT scans. Patient CTs have mm-size voxels that reproduce the lung tissue as a low-density homogeneous material, preventing the TPS from accounting for the lung modulation effect [14].

As already mentioned, particle beams are sensitive to density changes and inhomogeneities. Because of the even sharper dose profile and the increased radio-biological effectiveness, carbon ions show critical changes in their energy and dose deposition in lung treatments.

2.3.2 Protons and carbon ions in lung tissue

In lung treatments, internal tissue motion creates density changes along the particle path and tissue microstructure generates density heterogeneity. These effects compromise the advantages of particle therapy, producing range variations and straggling. Therefore, together with motion related uncertainties, a conformal dose distribution is jeopardized by a varying density composition. The lung modulation effect, arising from material inhomogeneities, has a physical impact on the final dose distribution, potentially degrading the treatment plan quality. For heavy particles,

like carbon ions, a radiobiological effect is also produced from the modulation of LET and RBE distributions that further increases normal tissue toxicity.

2.3.2.1 Physical impact

A particle beam traversing a heterogenous material experiences a different composition of low-density and high-density regions. In the case of lung tissue, the air-filled alveoli are alternated to a water-like tissue at a microscopic scale. This composition leads to energy loss and consequent range straggling, whose amplitude depends on the specific path particles take in the material. The modulating structure causes both a BP shift, due to the additional material placed in the beam path, and a BP broadening due to the density heterogeneity. The BP width, measured with the FWHM and the distal fall-off extent, increases because of the modulation effect [46]. The reduced BP maximum and the less steep fall-off translate into underdosage of the target and overdosage of the normal tissues distal to the tumor [47], [48]. Titt et al. [48] quantified the broadening of the distal fall-off up to 2 mm in water, meaning about 10 mm in lung, and a BP amplitude reduction of about 35%. A representation of the effect of different modulating materials on a pristine proton BP is shown in Figure 2.*11*.

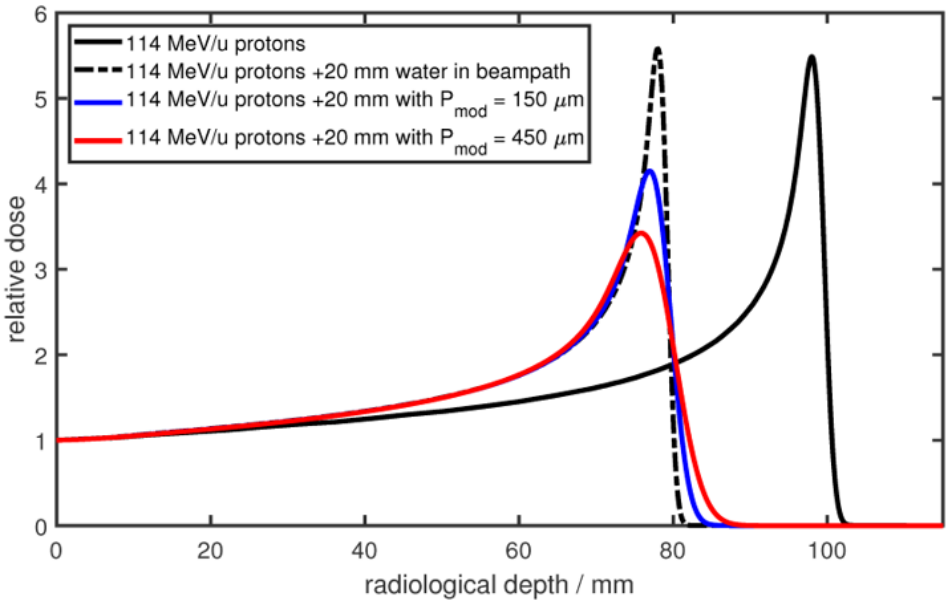

Figure 2.11 Depth dose distributions for a reference 114 MeV proton BP in water (solid black line) and with additional 20 mm of water in the beam path (dashed line). In blue and red are the BPs after traversing 20 mm of two different modulating materials. The modulating materials shift the BP in depth due to the additional material in the beam line and broaden the BP due to the heterogenous structure. Pmod=Modulation Power. Figure from [49].

The BP degradation is mathematically reproduced applying a convolution with a normal distribution whose kernel directly depends on the material modulation strength [50].

A voxelized geometry, made of randomly distributed low-density (0 g/cm^3) and high-density (ρ_{med}) voxels, is the basis of the mathematical model. The average density ρ_{mean} of the geometry is calculated from the product of the probability to have a high-density material voxel p and ρ_{med}. A particle traversing such structure exhibits a different range depending on the number of high-density voxels hit along the path, and the total water equivalent thickness (WET) can be derived knowing ρ_{med} and the voxel length d in beam direction. The probability that a path has a WET t' is described by the following normal distribution:

$$P(t' \mid \sigma, t) = \frac{1}{\sqrt{2\pi\sigma^2}} exp\left(-\frac{(t'-t)^2}{2\sigma^2}\right) \quad (2.8)$$

where t is the average WET of the voxelized geometry and σ quantifies the modulation strength of the material. From the parameters of the voxelized geometry:

$$\sigma^2 = t \cdot d \cdot \rho_{med}\,(1-p) \quad (2.9)$$

The degraded dose distribution $\mathrm{b} * (z)$ is obtained by a convolution between the normal distribution of Equation 2.8 and the unperturbed dose $\mathrm{b0}(z)$, as a function of depth z in water:

$$b * (z) = (P(t' \mid \sigma, t) * b0)(z) = \int_{-\infty}^{\infty} P(t' \mid \sigma, t)\; b_0(z + t')\, dt' \quad (2.10)$$

Conventionally, the $\mathrm{b0}$(z) shift does not refer to the BP maximum, but to the z_{p82} corresponding to the range at which the dose is 82% of the maximum, namely the mean range of particles [51].

From this analytical description, the new physical quantity Modulation Power (Pmod) can be derived as:

$$Pmod = \frac{\sigma^2}{t} = d(\rho_{med} - \rho_{mean}) \;\; [\mathrm{mmH_2O}] \quad (2.11)$$

Pmod does not depend on the physical and geometrical thickness of the material, but exclusively on its structure size d and the density difference between material components.
A schematic description of the mathematical model and its reproduction in a Monte Carlo (MC) set-up are depicted in Figure 2.*12*.

If the material density distribution is unknown, the Pmod can be measured downstream of the material, for example in water column experiments [52]. The Pmod is obtained by minimizing the difference between the measured modulated BP and the result of the convolution between measured pristine BP and the Gaussian function. The Gaussian σ and t values for which this minimum is found, are used to derive the material specific Pmod.

A direct Pmod calculation is not possible for lung tissue, because the density distribution is unknown, and measuring the Pmod remains challenging. In addition, the typical clinical CT resolution does not allow to resolve the lung microstructure, and the lung is represented in clinical images as a homogeneous low-density tissue. Flatten et al. [53] in their work proposed a method to estimate the Pmod from the patient CT density histogram. They demonstrated a clear correlation between the modulation strength of inorganic materials and the CT histogram kernel. However, the model shows its limits when applied to lung samples, because of the wide range of structure sizes strongly dependent on the specific lung region and air filling state.
These factors limit the introduction of the lung modulation effect in treatment planning processes resulting in an overestimation of the dose conformity. However, with the employment of high-resolution CT images an estimation of human lung tissue modulation strength is possible. The calculated Pmod values lie in the range from 50 μm to 300 μm [49].

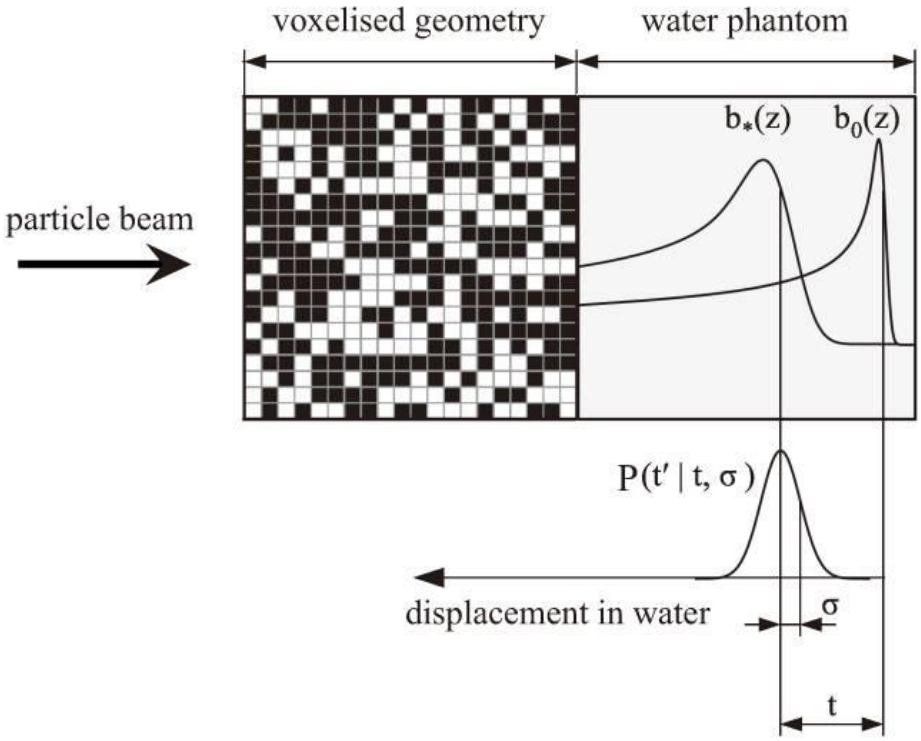

Figure 2.12 Schematic description of a particle beam degradation traversing a voxelized geometry and the relative Monte Carlo (MC) set-up. The voxelized geometry, composed of air (black voxels) and lung tissue (white voxels), is followed by a water phantom in which the dose distributions are scored. The unperturbed reference BP $b0(z)$ and the degraded dose distribution $b*(z)$ are shown in the water phantom. The $b*(z)$ is also derived by the convolution of $b0(z)$ with the normal distribution $P(t' \mid \sigma, t)$ in which t is the average WET of the voxelized geometry. The $b*(z)$ displacement is given by the mean value t and refers to the depth at which the distal fall-off is 82% of the maximum. Figure adapted from [52].

Porous materials and their dose modulation capabilities can also be beneficial in particle therapy, especially with carbon ions, to widen the sharp BP before it is delivered to the target. Ripple filters are used to broaden the pristine BP, reducing the energy steps necessary to cover the tumor volume in depth and to obtain a more homogeneous dose between single beam spots. Because of their modulation properties, porous materials such as the inorganic Gammex LN300 and LN450 phantoms (Tissue Characterization Phantom Model 467: User Guide 2004, used for the calibration of CT Hounsfield units (HU) in quality assurance) can be used as Ripple filters. The usage of porous materials as range shifters and modulators is feasible but is limited by the spread of the lateral dose penumbra. For very superficial tumors, or too thick modulators, the final dose distribution can present inhomogeneities [50].
From a physical point of view, protons and heavy ions undergo the same dose degradation process. However, for particles heavier than protons, an additional radiobiological effect has to be considered for a comprehensive understanding of the potential risk in clinical cases.

2.3.2.2 Radiobiological impact

The modulation effect derives from particle energy and range fluctuations. For low-LET particles, the tissue inhomogeneities mostly affect the physical dose distribution, but for high-LET particles, the shift in depth of primary ions also implies the modulation of LET and RBE distributions (see Figure 2.*5*). The displacement of primary high-

LET particles and RBE in depth increases the normal tissue toxicity distal to the target, requiring the characterization of this radiobiological effect.

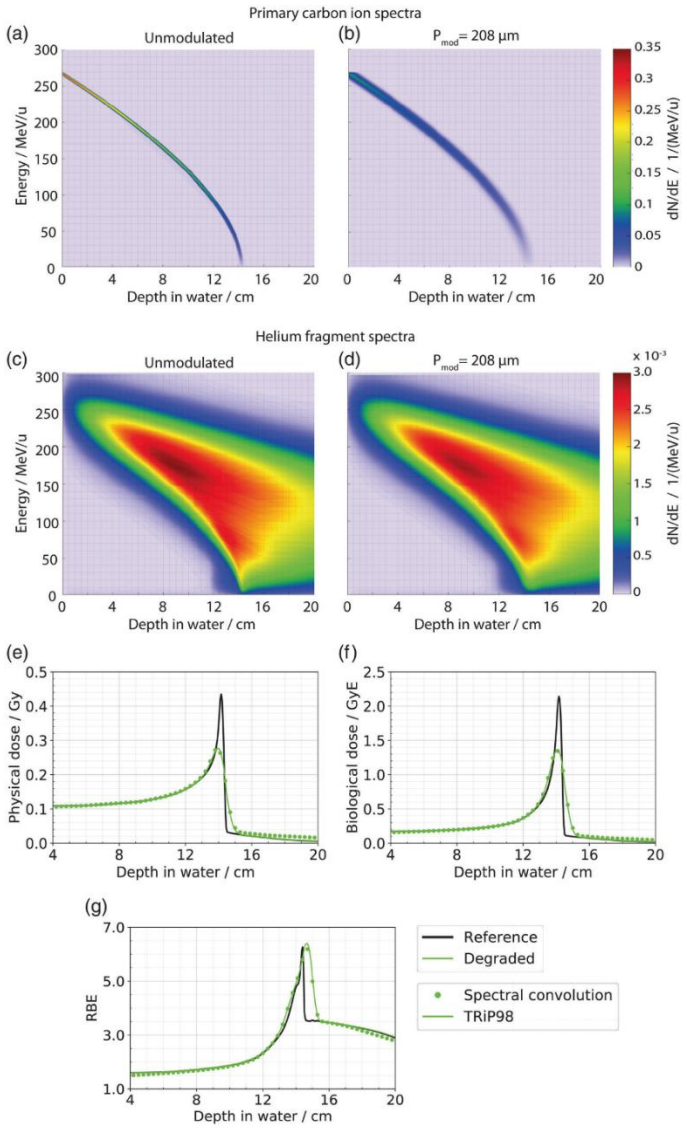

Figure 2.13 Spectral distribution of primary carbon ions (a,b) and produced helium fragments (c,d), both for the unmodulated (a,c) and modulated (b,d) case. The reference (black) and modulated (green) physical dose (e), biological dose (f) and RBE distributions (g) are shown. The spectral modulation (green circles) computed in Matlab and the TRiP98 prediction (green line) are compared. Figure from [54].

The analytical model of the lung modulation effect and the Pmod can be used to predict LET and RBE modulation of carbon beams in the presence of heterogenous materials [54], [55].

When a carbon ion beam traverses a homogeneous material, the RBE maximum coincides well with the BP [56], while Paz et al. [54] demonstrated that the RBE maximum shifts to greater depth as a consequence of the modulation caused by tissue heterogeneities. Paz et al. simulated in their study the changes of carbon beam spectra as well as the RBE broadening in the TPS by applying the mathematical model to the RBE-weighted dose calculation (see Figure 2.*13*). Complementarily, Zhao et al. [55] reproduced carbon LET variations applying the mathematical model to the dose calculation engines. Similarly to the dose, together with the LET profile shift in depth, a decrease of the maximum LET value occurs, and both effects are significantly more pronounced in longitudinal than lateral direction.

The understanding and investigation of physical and radio-biological aspects of lung tissue modulation effect, as well as its combination with motion related dose uncertainties are paramount to make CIRT a standard of care in radiotherapy of lung tumors. However, a significant spread of CIRT is also impaired by technological and economic challenges associated with the particle facility and delivery system, such as the gantry. Therefore, the emerging gantry-less solutions have to be included in the CIRT research objectives.

2.4 Gantry-less treatment for thoracic tumors

2.4.1 The gantry in radiotherapy

In the early stages of particle therapy, treatments were delivered by horizontal beam lines of large particle accelerators designed for research purposes which did not provide optimal beam delivery conditions for clinical applications. Patients were placed in front of the fixed beamline either in supine or upright position. The first proton treatment at the Lawrence Berkeley Laboratory (LBL) was realized in 1954 with patients in upright position in front of a horizontal beam [57]. When the first proton therapy centers were built, the gantry, already implemented for photon radiotherapy, was introduced to maximally exploit the intrinsic superiority of particle therapy. Because of the lack of upright imaging systems, the supine position became standard in particle therapy [19], and the gantry was developed as the mechanical support that permits the delivery of the beam from multiple angles around the patient.

In photon radiotherapy the gantry is relatively small compared to proton and heavy ions gantries that need to bend and focus high energy charged particles with large bending radii, requiring the use of high-field magnets [58].

After the particle accelerator, the gantry is the most complex, expensive and massive component of a radiotherapy facility. Its size is determined by the gyroradius ρ in the Lorentz formula of the magnetic rigidity:

$$B\rho = \frac{p}{q} = \frac{m_0 \gamma \beta c}{q} \quad (2.12)$$

B is the magnetic field, p the momentum and q the charge of the accelerated particle. The relativistic expression of the momentum describes its dependence on the particle mass m_0 and the relative velocity β. Therefore, the gantry size increases proportionally to the particle kinetic energy and the mass/charge ratio, which implies that the $B\rho$ for carbon ions is around three times bigger than for protons [10].

The first carbon gantry in the world with 360 degrees rotation capability was constructed in the Heidelberg Ion Beam Therapy (HIT) Accelerator and its sketch is depicted in Figure 2.*14*. It is a 25 m x 13 m structure with a total rotating mass of 670 tons. For comparison, the standard proton gantry is halved in dimension and has a weight smaller than 200 tons. With the employment of superconductive magnets, as for example the carbon gantry at the National Institute of Radiological Sciences (NIRS) in Chiba (Japan), a significantly smaller footprint is achieved with a total weight of about 300 tons [59].

Because of its complexity, only 4 carbon gantries are available worldwide, out of a total of 17 carbon therapy facilities. Most CIRT treatments are delivered through fixed beam lines, usually with a constant horizontal angle [60]. However, the horizontal fixed beam is not optimal for the treatment of thoracic tumors if the patient is lying on the couch. The anterior-posterior (AP) or posterior-anterior (PA) directions are optimal beam angle selection for lung treatments. The couch inclination along the horizontal axis partially enables the delivery of oblique and non-co-planar fields that

reduce the lung dose. However, the angle choice flexibility remains very limited if the patient is treated in supine position, and the gantry is not available.

While it provides increased flexibility in beam angle selection and the application of advanced techniques, the carbon gantry is associated with significant technological and economical hurdles, that overall limit the spread of heavy ion therapy. Therefore, ongoing research efforts aim to investigate gantry-less delivery systems, such as upright radiotherapy, in which the rotation of patient positioning devices replace the rotation of the beam delivery system [61]. In this way, increased beam angle flexibility is achieved, without the need for the gantry.

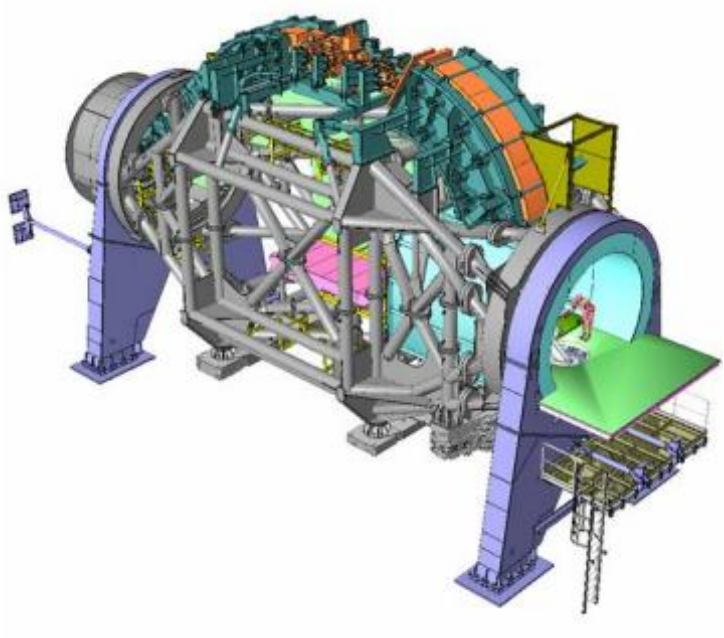

Figure 2.14 Sketch of the isocentric carbon ion gantry at the Heidelberg Ion Therapy (HIT) Accelerator. Figure from [62].

2.4.2 Upright radiotherapy

The shift of rotation capabilities from the beam delivery to the patient positioning system has the potential of reducing the gantry technological and economic hurdles, making gantry-less treatments a valuable alternative.
From enabling the first isocentric irradiation/photon imaging in the 1950s [63] and the introduction of thermoplastic masks in the 1980s [64], upright therapy rose again in the 2020s as a gantry-less treatment solution. The acquisition of CT images in radiotherapy, since their first implementation in 1971, is performed with the patient lying in a horizontal position. Therefore, the lack of dedicated imaging systems limited the development of upright therapy. The recent growth of upright patient positioning and imaging solutions, specifically CT scanners, has renewed the interest in this treatment modality [65], [66].

A gantry-less, upright radiotherapy system is composed of several essential elements designed to enable flexible and precise beam delivery. These systems are based on the use of a fixed radiation source that delivers the beam with a horizontal angle. Beam angular variability is achieved through a rotating patient chair, supported by a motorized platform or robotic arm, capable of 360 degrees rotation that allows the patient to be positioned relative to the fixed beam to achieve multiple treatment angles. To provide accurate tumor targeting, a six-degree-of-freedom (6-DOF) positioning system enables controlled translational and rotational patient movements. Integrated imaging guidance

systems, including vertical volumetric CT and orthogonal 2D X-ray imaging, are essential for positional verification, which helps to mitigate uncertainties in upright positioning.
Both the patient positioning and the vertical CT system have a variable tilt angle that allows the irradiation of the abdomen and pelvis region through the inclination of the chair backrest. The tilt angle varies from 2 to 30 degrees in the PCure system and between 0 and 15 degrees in the Leo Cancer Care system.
In addition, dedicated immobilization devices, including custom-molded supports (e.g. vacuum cushions) are incorporated to ensure reproducible setup and enhance patient comfort throughout the treatment process [67], [68], [69].

In the context of CIRT of lung cancer, upright therapy might have the potential not only to eliminate the necessity of the gantry but also to reduce internal tissue motion and related dose degradations. In the following, economic and technological motivations for upright therapy as well as its potential clinical benefits are discussed with a focus on carbon treatments of thoracic tumors.

2.4.2.1 Economical and technological motivations

Economic and technological advantages of upright therapy are applicable to multiple treatment modalities (from photons to heavy ions). Gantry-less treatments are inherently resource-efficient because of the reduced equipment, room size and cost. It has been estimated that the cost of a new proton treatment room can be reduced from an average of $40 million to about $10 million, if the chair system replaces the rotating gantry. An even further cost reduction would be achieved for carbon treatment rooms [70].
Upright positioning systems are extremely compact (see Figure 2.*16*) and light compared to the massive gantries. The total weight is usually less than 3 tons, almost 100 times lighter than a carbon gantry [71]. Upright systems provide positioning accuracy comparable to supine couches, and, thanks to the employment of 6-DOF support structures, a high flexibility is achieved. These characteristics make them suitable for multiple treatment sites, from the head and neck to the pelvis [67], [68], [69]. Examples of upright positioning solutions are depicted in Figure 2.*15*.
Furthermore, a positioning system able to rotate in front of a fixed beam enables a significant reduction of shielding costs because only one primary beam direction is available. As a result, the total volume of concrete shielding is lowered. In addition, a fixed beam line is simpler, more robust and can provide easier access to individual components, making maintenance and upgrades more feasible. Indeed, rotating the beam with a gantry means that multiple factors can degrade beam precision, so that robustness requires additional verifications and testing [61].

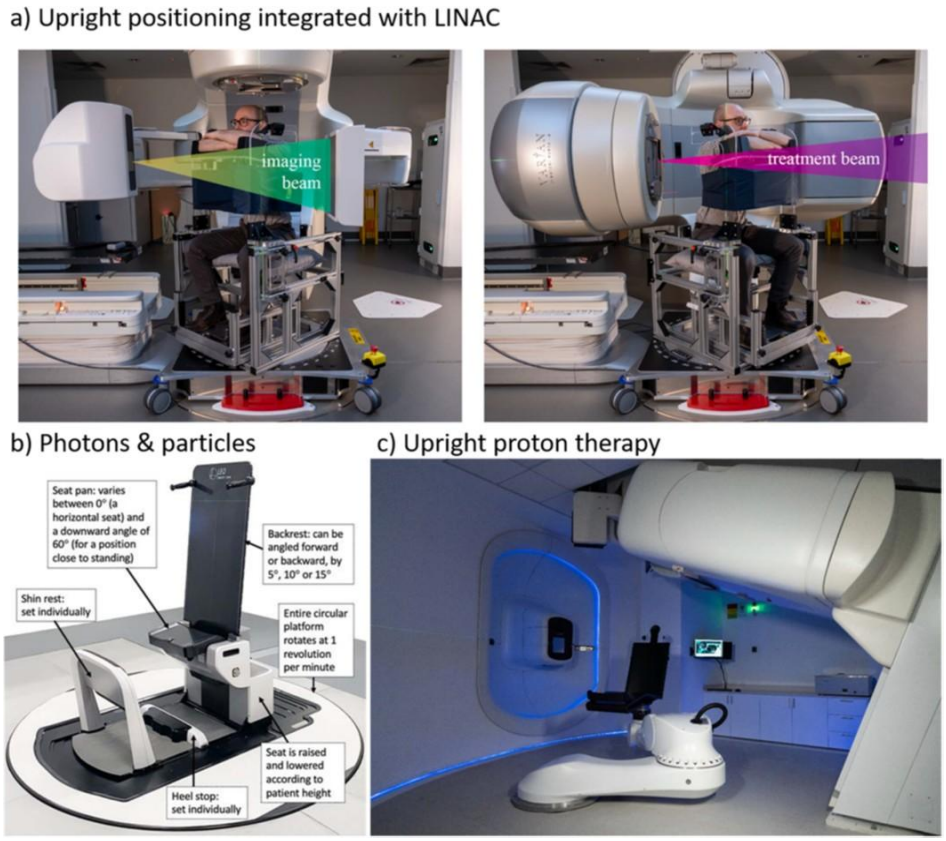

Figure 2.15 Upright patient positioning systems examples. Prototype of the positioning integrated with a LINAC at the Peter MacCallum Cancer Center (Melbourne, Australia) (a). Commercial positioning system from Leo Cancer Care Ltd (Smallfield, UK) developed both for photon and particle therapy. Reproduced from [72] CC BY 4.0 (b). Upright proton therapy facility at the Hadassah Medical Organization by P-Cure Ltd (Shilat Industrial Zone, Israel) (c). A previous version of the system has been in use at the Northwestern Medicine Chicago Proton Center (Chicago, Il, USA) since 2016. Figure from [61].

The flexibility and modularity of a fixed beamline open up opportunities for novel treatment techniques. For example, the application of particle arc therapy, with high potential for increasing plan conformity, is limited in supine treatments by the dynamic switching of gantry magnet parameters and the uncertainties of the numerous gantry positional changes [73]. Moreover, the additional space behind the upright positioning system in beam direction, can be exploited for advanced treatment and range verification methods, such as ion imaging or positron emission tomography (PET) activation imaging [71].

The use of a compact system permits its integration into existing radiotherapy treatment rooms. However, the integration with existing imaging, beamline components and quality assurance (QA) equipment, might become a limiting factor. If multiple rooms are available in the facility, the design of a dedicated room for upright system would be possible with much lower expenses than a gantry-based system [74] (see Figure 2.*16*).

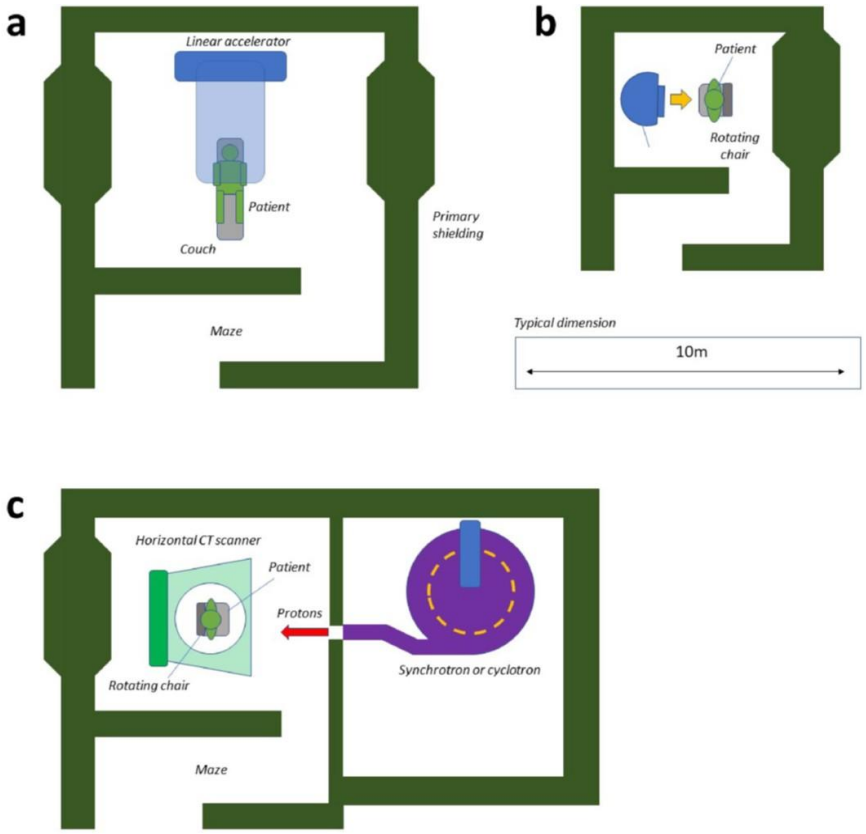

Figure 2.16 Schematic design comparison of typical radiotherapy treatment rooms. Conventional bunker for a medical linear accelerator with gantry mounted at the isocenter (a). Bunker for an upright therapy delivery system with fixed MV beam source (b). Bunker for a proton accelerator, stationary beamline, rotating upright positioning system and horizontal CT scanner above the patient (c). Figure from [61].

The benefits of upright treatment extend to the enhanced patient comfort and overall tolerance of radiation therapy. Furthermore, the total access time for an upright CT scanner can be halved with respect to a supine scanner, increasing patient comfort but also making the whole treatment more time-efficient and therefore cost-efficient if a larger number of patients can be treated [75].

From the clinical perspective, significant anatomical changes occur if the upright chair system replaces the supine couch. This might play a role in reducing soft tissue motion and drifts and may change physiological processes, such as breathing motion and pattern.

2.4.2.2 Clinical motivations

Adopting an upright posture, rather than the standard supine position, can lead to significant changes in patient anatomy. As a result, the lack of upright imaging systems that account for these anatomical changes in the treatment plan optimization, prevented the spread of upright therapy in the last decades. For this reason, the upright position was mainly employed for ocular tumor therapy [76]. Tumors located in the head are only minorly affected by posture changes and seated treatments are possible even if only supine CT scans are available [61], [77].

This is not the case for tumors in the thorax or abdomen, where the action of gravity changes the anatomy of tissues and organs such as bowel, stomach, liver and lung. As depicted in Figure 2.*17*, because of the ribcage displacement, the lung volume increases (about 17% and 10% for left and right lung [78]), more air flows in the lung and the overall

respiratory cycle becomes more stable [79], [80], [81]. Excursion of the diaphragm is reduced in the upright position, but more air volume is inhaled because of the movement of the lower ribs and the overall outward movement of the thoracic cage [82]. The reduction of intra-fractional motion, and consequent interplay effect, can be impactful in particle therapy of lung tumors (see section 2.2 Tumor motion). The WET as key in particle therapy should not be affected by increased air volume in the lung, but a lower density might reduce dose conformity because of increased beam modulation. Moreover, if more air volume is inhaled a larger perfusion occurs in lungs, to maintain proper gas exchange and lung function. Therefore, more blood might also be present in the lung and can potentially receive dangerous doses [74], [83].

A reduced diaphragm displacement also influences motion of abdominal organs (see Figure 2.*18*). For example, the liver mostly moves in inferior-superior (IS) direction following the respiratory cycle and its displacement might be reduced by several mm by positioning the patient in an upright position [84].

In the abdomen, the internal tissue motion also derives from organ drift that takes place during irradiation. Since patients spend most of their day in an upright position, increased consistency is achieved with the seated treatment posture which diminishes tissue drift in a time span of a single fraction [84], [85], [86]. Furthermore, a better sparing of the heart and abdominal organs might be achieved when lung tumors are targeted, because of the action of gravity displacing all the organs in the inferior direction [87]. Nevertheless, studies supporting these findings underlined that this effect may vary between patients and needs to be assessed for single cases [78].

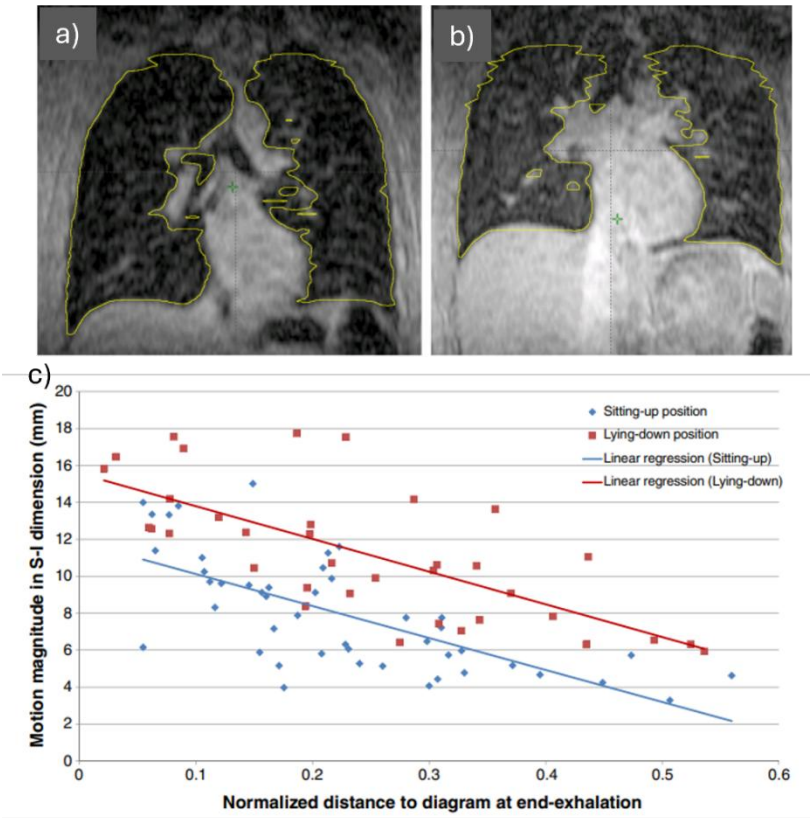

Figure 2.17 Supine and upright lung volume (a,b) and lung landmarks motion amplitude comparison (c) for one volunteer. The lung volume at the end-exhalation is compared between supine (a) and upright (b) CT. The upright lung volume is significantly larger. Lung landmark motion in inferior-superior direction at the end-exhalation (c). The linear regression analysis indicates an average decrease of 4 mm for the upright position. Figure from [81]; permission conveyed through Copyright Clearance Center, Inc.

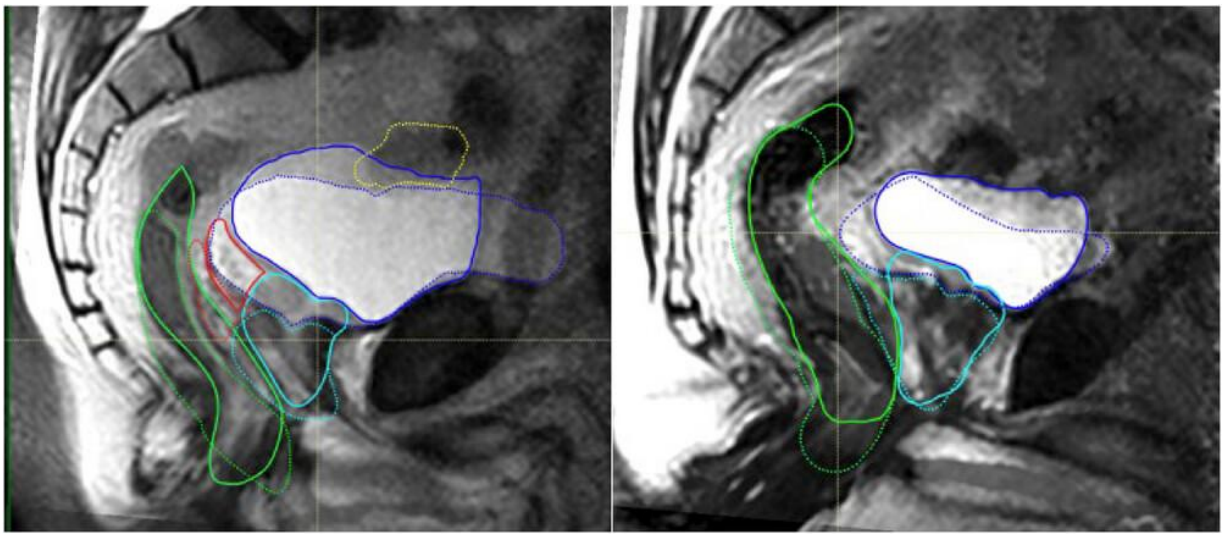

Figure 2.18 Supine (solid lines) and upright (dotted lines) magnetic resonance imaging (MRI) of two volunteers. The rectum (green), prostate (light blue), bladder (blue) and small bowel (yellow, only left panel) are shown. Figure from [86].

Ultimately, the upright posture is more comfortable and able to increase patient involvement throughout radiotherapy session [72], [80], [88]. Furthermore, some patients may find it difficult to maintain a recumbent position if disease conditions arise, such as breathing issues, dyspnea or phrenic nerve injury [80], [81], [89] and the upright posture becomes the only possible treatment modality.

It emerges that upright therapy provides enhanced stability and patient comfort. However, the net clinical effect is likely patient specific and needs to be further evaluated through dedicated treatment planning studies. The current lack of clinical evidence impairs the translation of upright therapy to standard clinical practice, and the comparison with supine treatment has to be performed in dosimetric studies for a comprehensive assessment of the treatment quality (see Chapter 5).

3 Treatment Planning

Treatment planning is the design of an optimal radiotherapy plan for a patient. It ideally delivers the prescribed dose to the target, releasing no dose to normal tissues. In analytical TPS, like the in-house GSI TRiP98 [30], [90] used in this work, the treatment plan is the result of an optimization process, based on the minimization of a cost function. TRiP98 optimization and dose calculation algorithms are described in this chapter, together with diagnostic imaging modalities, target and volumes of interest (VOI) definitions, image registration and plan quality evaluation methods.

3.1 Diagnostic imaging in radiotherapy

Diagnostic medical imaging has a central role in modern radiotherapy, and its development has been fundamental for the improvement of treatment precision and conformity. The invention of CT in 1971 enabled precise tumor visualization and normal tissue sparing, by replacing 2D X-ray with volumetric 3D imaging [91]. Diagnostic CT images represent the backbone of radiotherapy planning, as they offer consistent geometric reference for patient setup and provide electron density information required for conformal 3D dose calculation. Treatment planning strongly relies on X-rays absorption in patient tissues which is measured with CT images. The absorption coefficient (μ) is assigned to the image unit (voxel) in HU and then converted into tissue stopping power. The resolution of a typical clinical CT is in the order of millimeters in the three spatial directions, and the position of the BP can be identified in the patient using center-specific calibration curves and the given particle energy.

Four-dimensional CT (4DCT) extends the anatomical description capabilities of the 3DCT by capturing internal motion. In particular, the 4DCT allows clinicians to account for the movement of the tumor and organs over the breathing cycle and to include this information in plan optimization and/or dose calculation (see sections 3.4.2 and 3.5.1). A 4DCT is a set of 3DCTs each representing a different phase of the breathing motion (see Figure 3.*19*). The breathing cycle is usually divided into 10 phases of which the end-inhale and end-exhale are the most representative ones and are considered the reference phases. A 4DCT is the result of multiple 3DCTs recorded over time and then sorted to be assigned to the correct breathing phase [92].

The CT is the principal 3D (or 4D) imaging modality used for dose calculation. However, some disadvantages are present, like the additional exposure to ionizing radiation and the limited soft tissue differentiation. A better soft tissue contrast can be obtained with the introduction of magnetic resonance imaging (MRI) in treatment planning. MRI improves target and normal tissue delineation compared to CT images alone, and this becomes relevant for the abdomen, pelvis and brain tumor sites. MRI can also give functional insights through techniques like diffusion-weighted or perfusion imaging. Additionally, the use of PET images provides metabolic or molecular activity information to be added to the anatomical patient description given by CT and MRI. Multimodality imaging techniques that combine CT, MRI and PET are often chosen to define the best treatment strategy and achieve the best clinical outcome.

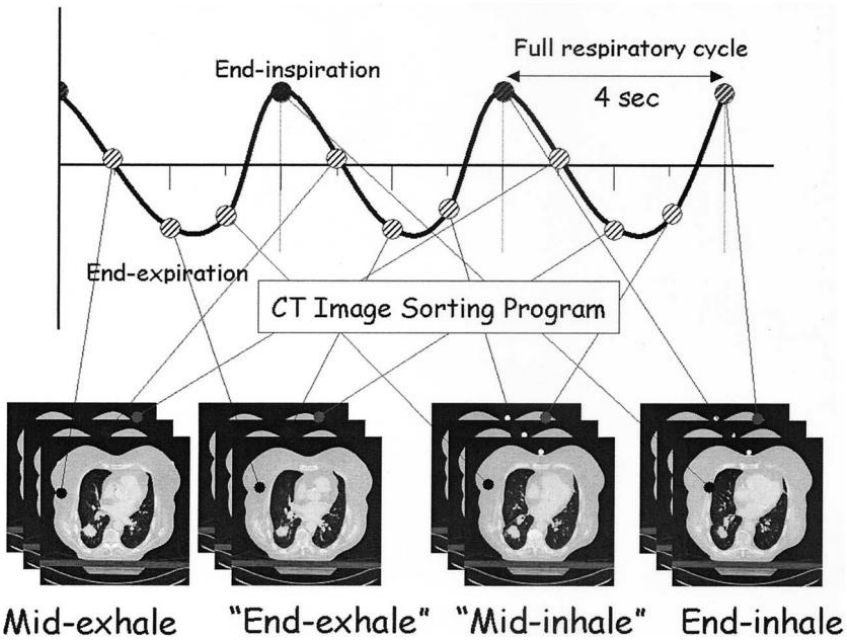

Figure 3.19 Schematic representation of the respiratory phase "bin" generation from four-dimensional computed tomography data. Figure from [92].

Therefore, the availability of CT scanners is fundamental in treatment planning and the further access to MRI and PET images significantly improves the treatment precision.

The lack of dedicated imaging systems represented the main limitation to the development of upright radiotherapy in the last decades. The first upright CT scanner was developed at the Japanese Keio University School of Medicine in 2012 [75], as a standing CT prototype for the scan of the whole body. In 2025, they released the first multi-position CT capable of scanning in supine, upright and standing positions.

However, these are single center prototype systems and only with the development of commercially available upright 3D and 4DCT scanners [65], [66] a renewed general interest in upright therapy was possible. The technical evaluations of these novel CT scanners are still ongoing to prove their feasibility in radiotherapy simulations and treatment planning [93], [94].

Similarly, only a few upright MRI [95] and PET [96] imaging systems are available worldwide, but none is implemented in the clinical workflow.

A wider spread of upright imaging systems would open the possibility of precise patient anatomy delineation, and the investigation of anatomical and physiological patterns changes with respect to the supine position.

3.2 Volumes of interest

Starting from the patient's anatomical information provided by the CT, a precise delineation of target volumes and OARs is fundamental to define the optimal plan. Standardized definitions of target volumes are provided by the ICRU report 93 of the International Commission on Radiation Units and Measurements [97]:

- **Gross Tumor Volume (GTV)**: the gross palpable or visible volume of the malignant growth, identified on diagnostic images.
- **Clinical Target Volume (CTV)**: the volume around the GTV where malignant cells are expected to be found. The whole CTV has to be treated to avoid tumor recurrence.

- **Internal target volume (ITV)**: the CTV expanded by internal margins, to account for anatomical variations and motion. The ITV can be defined as the geometrical union of the CTVs in different phases of the respiratory cycle (IGTV) or the union of CTVs previously transformed to the water-equivalent space along the beam path (range-ITV) [98].
- **Planning Target Volume (PTV)**: the volume to which the dose is assigned, built as the CTV extended by setup and internal margins.
- **Organs at Risk (OARs)**: the healthy organs around the PTV that have to be spared from radiation doses.

The described structures, shown in Figure 3.*20* are the VOIs in treatment planning and are traditionally segmented manually by radiation oncologists. An automatic segmentation is also possible with the use of algorithms powered by Artificial Intelligence (AI). Manual segmentation is a time-consuming, subjective and error prone process that largely benefits from the use of automatic tools, with which the human input is limited to the QA phase [99].
While the delineation of GTV, CTV and OARs is based on clinical anatomical criteria, ITV and PTV can vary with treatment modality, beam direction and patient positioning. The addition of margins can be directly included in the optimization process with a method called robust optimization (see section 3.4.1 Robust optimization) [100].
For moving targets, the volume delineated on a static anatomy can occupy different spatial positions over time. In 4D optimization (see section 3.4.2 4D optimization) the whole patient anatomy and target volumes across various motion phases are incorporated in the optimization process, implicitly defining the ITV [98].

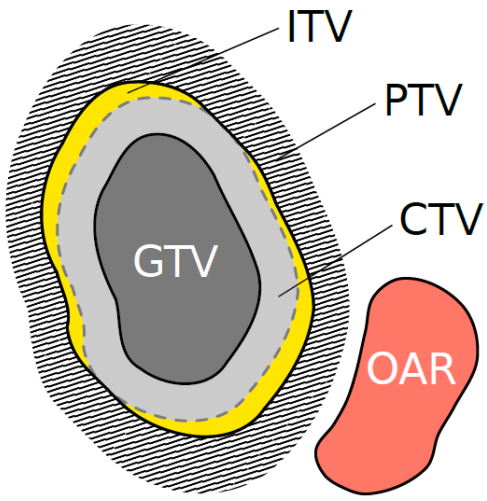

Figure 3.20 VOIs schematic representation. Gross tumor volume (GTV) expanded to form the clinical target volume (CTV), that has to receive the prescribed dose. The internal target volume (ITV) is defined to include motion variations while the planning target volume (PTV), the plan optimization objective, accounts for geometrical uncertainties. The sparing of Organs at risk (OARs) in the vicinity of the PTV has to be included in plan optimization. Figure from [38].

The use of functional images (MRI and PET) in combination with the CT enables an optimal VOI delineation, especially when enhanced soft tissue contrast is required. Image registration is a fundamental step to align images of different modalities or acquisition times and precisely identify VOIs but also positioning error and anatomical changes.

3.3 Image registration

Image registration is a process that incorporates many techniques and represents an essential component of modern radiotherapy. It allows to align, integrate and fuse medical images of the same patient acquired at different times, with multiple imaging modalities, or under different patient conditions, such as body posture [101], [102], [103].
In clinical practice, image registration has applications in image-guided radiotherapy (IGRT), adaptive radiotherapy (ART) and dose accumulation. Multiple imaging modalities (CT, MRI, PET) can be merged for a comprehensive anatomical and functional understanding of the treatment site [104]. Moreover, registration allows for accurate patient positioning, evaluating and quantifying patient intra- and inter-fractional changes [105].

The registration process is based on a spatial transformation that deforms a moving image I_A to a reference image I_B, maximizing image similarity through an optimization process. From a set of candidate solutions, the optimal one minimizes spatial differences between the two images, producing as output a 3D matrix or a 3D deformation vector field (DVF) able to map each voxel from image I_A to image I_B.
A generalized registration framework, applicable to multiple registration models, is presented in Figure 3.*21*.
Registration modalities can be classified following multiple criteria, for example, rigid image registration (RIR) and deformable image registration (DIR) methods are defined.

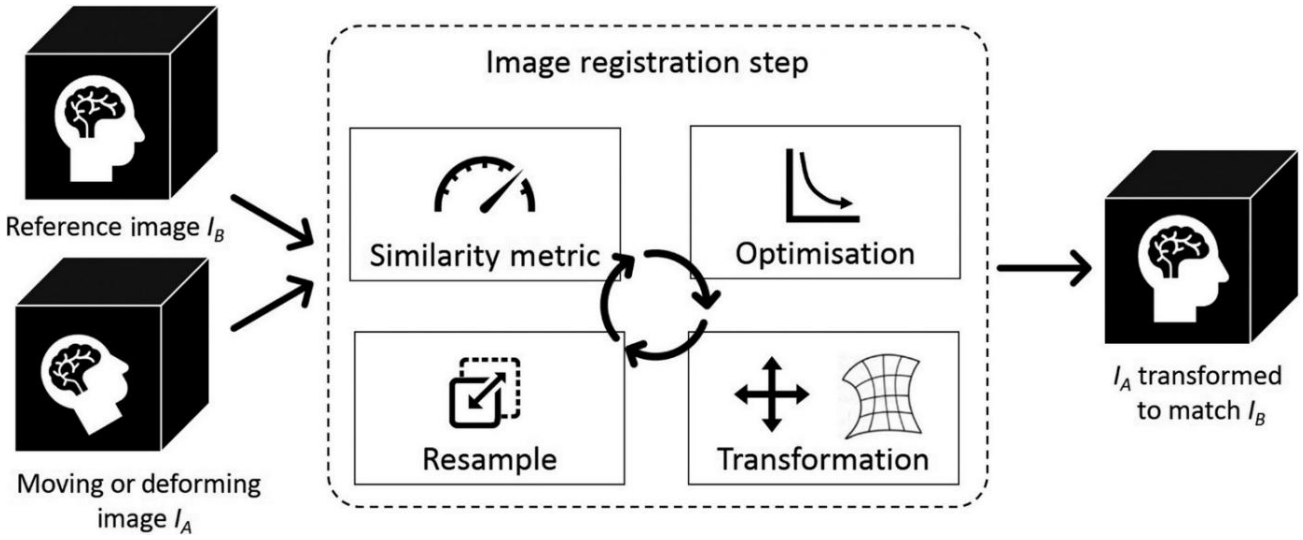

Figure 3.21 Sketch of the image registration process. A moving image I_A is transformed to match a reference image I_B. Rigid image registration (RIR) and deformable image registration (DIR) follow the same process; however, different similarity metrics, optimization and transformation algorithms are used. Figure from [106].

The RIR assumes that image differences can be described through translational and rotational movements, and that no shape and size changes occur. The deformation algorithm is computationally efficient and robust since it is limited to the optimization of six parameters (three translations and three rotations). The main applications are the multi-modality image fusion and patient setup verification, where the assumption of a constant geometry is usually applicable.
If significant soft-tissue motions and deformations take place between images, non-rigid anatomical variations have to be described through DIR methods. Non-linear deformations occur because of internal tissue motion, changes in patient positioning, tumor volume variations or any anatomical modification happening during therapy. The DIR is

usually applied in ART, VOI propagation or dose accumulation, through complex and computationally demanding optimization algorithms. DIR accuracy depends on factors like image quality, algorithm choice as well as parameter tuning. To obtain a superior result, RIR can be applied prior to the DIR, to account for systematic variations between images, so that the DIR only focuses on non-rigid deformations.
Further approaches classify the registration based on the used image information (intensity-based vs feature-based) and the chosen deformation model, for example the free-form deformation (FFD). FFD models are based on a grid of control points overlaid on the image and the interpolation of the deformation between these points using smooth basis functions, typically B-splines.
DIR algorithms can be generally divided into multiple steps. In the initialization step a grid of evenly distributed control points is arranged across the volume. The control points can be placed at variable distances, allowing for flexible deformation precision. Then, a deformation field is computed and applied to I_A. The target cost function is evaluated by comparing the warped I_A with I_B, and after updating the control point displacements the next iteration begins. Registration cost functions are regulated to ensure transformation smoothness and limited complexity, synonymous with anatomically and physiologically plausible movements. A regularization term is added to the objective function to guide the optimization towards a solution that is both representative of the data and overall smooth. FFD and B-splines inherently generate smooth displacement fields characterized by vectors whose direction and magnitude change gradually.
When the target function reaches a predefined minimum threshold or converges, the final configuration of control points is returned as the optimal solution [107], [108], [109].

Image registration, and in particular DIR, is a complex process that has a critical role in multiple aspects of radiotherapy. Therefore, it is paramount that a high quality and reliable solution is provided by the registration optimizer. Multiple QA methods exist and can be classified into deformation field evaluation metrics and anatomical correspondence evaluation metrics [110], [111].
Deformation field evaluation metrics quantify the physical characteristics of the DVF. Examples are the inverse consistency error (ICE), which assesses the consistency between the DVF and its inverse, the Jacobian of the deformation field, to validate its physical behavior and the harmonic energy of the deformation field to quantify the regularity of the spatial transformation.
Anatomical correspondence metrics, instead, assess registration quality through the similarity of predefined contours or treatment planning VOIs. Examples of evaluation metrics are the dice similarity coefficient (DSC) and the Hausdorff distance (HD) [112], [113].
The DSC is calculated by overlapping the predicted VOIs, propagated from I_A to I_B by means of the DVF, with the ground truth, which is the structure delineated on the reference image. The quality of this superposition is quantified as the harmonic mean of sensitivity and precision:

$$DSC = \frac{2TP}{2TP+FP+FN} = \frac{2(A \cap B)}{A+B} \quad (3.13)$$

where true positive (TP), false positive (FP) and false negative (FN) are extracted from the confusion matrix. Geometrically, it is equivalent to the ratio of structure intersection and union. DSC can vary between 0, for completely non-overlapping VOIs, to a maximum of 1 for perfect overlap [111]. Values above 0.9 are considered excellent in medical imaging applications.

The HD is a spatial distance-based metric that measures the distance between boundaries of the predicted and ground truth segmentation. Usually, the symmetric average HD (AHD) is calculated as the maximum between the AHD $d(A,B)$ calculated starting from I_A to I_B, and its reverse $d(B,A)$, calculated from I_B to I_A:

$$d(A,B) = \frac{1}{N}\sum min \parallel a - b \parallel_{a\in A, b\in B} \quad (3.14)$$

$$AHD(A,B) = max\big(d(A,B), d(B,A)\big) \quad (3.15)$$

In Equation 3.14, $\parallel a - \mathrm{b} \parallel$ represents the Euclidean distance [111]. The symmetric AHD, ideally equal to 0, is considered acceptable for values smaller or comparable to the image unit dimension, namely the CT voxel size.
DSC can be biased towards big structures, because inner voxels are usually easier to predict than voxels at the border, but in the DSC formula this distinction is not present. Therefore, the DSC could provide good results even in case of low-quality deformation. On the other hand, AHD can be biased towards small structures. For thin structures, the AHD could still return a good value even if the propagated VOI misses part of the ground truth. Thus, it is important to look at both metrics for a solid registration QA [114].
In radiotherapy applications, the structures contoured on the reference image can be subject to errors and are strongly dependent on the clinician who delineates them. This is true for OARs but becomes critical for GTV and CTV definitions. Therefore, the determination of a ground truth, on which anatomical correspondence metrics are based, is nontrivial and non-unique.

In this thesis, CT and VOI visualization and processing, image alignment, DSC and AHD calculation were performed in 3DSlicer, an open-source software platform developed for medical image visualization and processing [115]. The image registration was instead performed with Plastimatch, an open-source software for image computation [116].

Image acquisition, VOI delineation and image registration represent the starting point of the treatment planning process, which ultimate goal is the definition of the optimal treatment plan.

3.4 Plan optimization

The determination of the optimal treatment plan is achieved through dedicated software, like the TPS TRiP98 developed at GSI and used in this work. TRiP98 uses an "inverse" planning approach, which aims to find the best superposition of multiple pencil beams with individual energy, position and particle number, in order to deliver the prescribed dose. The optimal plan is obtained with an iterative process based both on physical and biological models. Physical models provide the TPS with information about the delivery system, primary and secondary particle interactions in water, and measurement of X-ray absorption in tissue. The biophysical model LEM, instead, enables biological dose calculation in TRiP98, through RBE distribution prediction in each position of the treatment field (see section 2.1.2 Radiobiology). In this work, RBE tables calculated with LEM I were used in treatment planning studies (see section 4.2 and Chapter 5), while LEM IV was adopted for experimental applications (see section 4.1 Experimental validation of lung modulation radio-biological effect). LEM I is currently implemented in clinical practice, allowing direct comparison of these results with clinical results and the existing literature. For experimental studies, such comparability is not required; therefore, the updated version of the model was employed.
The plan optimization process in TRiP98 is based on the definition of a set of parameters: particle energy, lateral pencil beam position and particle number N. Among these, the particle number N of each pencil beam is the objective of the following cost function

$$F_{PTV}(\vec{N}) = \sum_{i \in PTV} w_{PTV}\left(D_i^{act}(\vec{N}) - D^{prescr.}\right)^2 + \sum_{j \in OARs} w_{OARs}\ \Theta\left(D_j^{act}(\vec{N}) - D^{limit.}\right)\left(D_j^{act}(\vec{N}) - D^{limit.}\right)^2 \quad (3.16)$$

The optimization process minimizes the difference between actual (D^{act}) and prescribed ($D^{prescr.}$) absorbed dose in each voxel (see Equation 2.4). The first term regulates the dose to the PTV, while the second term ensures the OAR dose does not exceed the limit D^{limit}. Tumor control probability (TCP) and normal tissue complication probability (NTCP) are balanced in the cost function through predefined weights w_{PTV} and w_{OARs}.

In a clinical scenario, the plan is usually delivered through multiple fields that reach the tumor from different directions. In the single field uniform dose (SFUD) approach, each field is optimized on its own and provides a homogeneous fraction of the prescribed dose. The intensity modulated particle therapy (IMPT) technique, instead, optimizes all fields simultaneously, allowing for better normal tissue sparing, but decreasing plan robustness in the presence of setup errors or misalignment.

Plan robustness against setup and positioning errors and anatomical changes can be included at the optimization stage through the implementation of robust optimization techniques. 4D optimization methods are robust techniques in which intra-fractional motion uncertainties are implicitly considered.

3.4.1 Robust optimization

Treatment delivery, setup and patient positioning errors are accounted for in treatment planning through margins (see section 3.2 Volumes of interest). Including these margins during the optimization process increases plan robustness. A robust optimization algorithm based on the worst-case evaluation approach was implemented in TRiP98 [117]. The absolute error is modelled by evaluating different scenarios, through which intrinsic margins are defined. In a standard approach, nine scenarios are considered: tumor in the nominal position (1 scenario), tumor displacement in the three negative and positive spatial directions (6 scenarios), range changes in beam direction, modelled via CT density scaling (2 scenarios). The worst-case scenario is assessed for each voxel, assigning a penalty in case of doses lower than $D^{prescr.}$ and larger than D^{limit} for target and OARs, respectively.
The CTV to PTV expansion is commonly in the order of millimeters, and a ±3.5% CT density scale is applied for range changes. These values, currently used in clinical applications, derive from experience and population-based analyses [118], but might vary depending on treatment site or case-specific requirements. For non-standard treatment modalities, such as upright therapy, which change patient posture as well as positioning and imaging systems, the application of these margin recipes needs to be investigated and eventually revised.

3.4.2 4D optimization

With the increasing number of centers treating moving targets, it became fundamental to develop planning techniques able to consider the impact of organ motion in clinical applications. Critical dose deformations especially occur if moving targets are treated with scanned particle therapy, because of the interplay effect (see section 2.2.3 Interplay effect).
Motion management strategies can be divided into methods that compensate for motion with the use of external devices (breath-hold, abdominal compression) and methods that adapt the treatment during planning and/or delivery (tracking, rescanning, gating). 4D optimization strategies belong to the second category, since they include patient

motion in the optimization algorithm and do not require external devices. In clinical practice, a motion amplitude exceeding 5 mm is used as threshold for the application of motion management methods [119].
4D optimization methods are a form of robust optimization where anatomical variations are included in the optimization via multiple image sets.
Starting from the 4DCT, the internal motion can be reconstructed and tracked and IGTV as well as range-ITV can be created for single patients. For the ITV definition, the target position in each phase of the 4DCT needs to be known. Initially, the target is delineated on the reference phase and then propagated to the other phases by means of DIR. The DVFs obtained from DIR are also used to propagate and cumulate doses between phases, resulting in the so-called 4D dose distributions (see section 3.5.1 4D Doses). The determination of the IGTV allows motion uncertainties to be accounted for in 3D optimization strategies. However, when a 3D plan is optimized to the IGTV some of the target voxels belong to the lung in the reference CT. Therefore, density override of the target with the HU value of the average tumor density is employed to calculate the correct beam range. This strategy was applied to all the 3D plans of this thesis, applying a 70 HU density override inside the IGTV.

TRiP4D is the 4D architecture of TRiP98 developed to compute 4D optimization and 4D dose calculations [120], [121].
As an advanced form of robust optimization, 4D optimization methods directly include motion and range variations at the planning stage. Therefore, an extended version of the presented cost function is implemented, in which the dose is calculated for each voxel as well as each motion phase. The result is a 4D cost function that is the sum of the cost functions in all motion phases. DIR is performed between 3D images of a 4DCT to propagate VOI voxels across phases.
This 4D optimization method is called "4D-ITV" in TRiP4D, to be distinguished from other 4D plan methods, and it is employed in this work [122].

3.5 Dose calculation

The determination of the dose distribution on patient geometry is the last step of the plan optimization process. In "inverse" treatment planning the optimization process starts from a prescribed dose distribution. Once an optimal solution is found, the number of beam spots, the assigned particles number as well as their spatial and energy distribution are known. The physical dose distribution, calculated for each CT voxel, directly depends on the beam spot locations and particle numbers, and RBE-weighted doses (biological doses) are derived by computing the product with RBE distributions (see Equation 2.7).
Static (3D) dose calculations are performed on single CT (reference 3DCT, average CT, mid-ventilation CT) to assess the quality of the plan, but multiple doses can be computed to evaluate different sources of uncertainty. In this section, the features available in TRiP98 (and TRiP4D) and used in this study to simulate motion and lung modulation dose degradation, are described.

3.5.1 4D Doses

4D doses are calculated and compared to static dose distributions to assess motion-related plan distortions.
The Task Group Report 290 of the American association of physicists in medicine (AAPM) provides the following definitions [123]:
- **4D accumulated dose or 4D dose (4DD)**: the average of the doses calculated on individual selected 3D volumes of the 4DCT, using the planned delivery sequence.

- **Dynamically accumulated 4D dose (D4DD)**: considers both the time-dependent delivery sequence and the representative anatomic motion.

4DD are computed in TRiP4D as the accumulation on the reference CT of the dose distributions calculated on each phase of the 4DCT set. DIR is computed between the reference phase CT and all the other CTs, to allow for dose propagation and accumulation. The time-dependency of beam delivery is not considered, and the interplay effect, as superposition of beam motion and tumor motion, is neglected.
The interplay effect is reproduced via D4DD calculation. The plan delivery time sequence is simulated in TRiP4D via a GSI in-house beam delivery simulator [120]. The simulator reproduces accelerator and beamline characteristics of clinical facilities such as the HIT, Marburg Ion Beam Therapy Center (MIT), and Shanghai Proton and Heavy Ion Therapy Center (SPHIC). If the original patient-specific breathing motion is not available, artificial motion functions are used as a surrogate for the breathing pattern [124].
To reproduce patient respiratory cycle variations over time, motion surrogates with different period lengths can be chosen to increase results variability and similarity with real cases. Similarly, different breathing phases can be selected as starting delivery phases to reproduce the random nature of the interplay effect. The motion amplitude information, on the other hand, is directly extracted from DIR of 4DCT phases. Notably, motion characteristics extracted from a single 4DCT set are representative of the respiratory cycle at the moment of the image acquisition. Breathing patterns are subject to changes over time and the 4DCT acquired at the beginning of the treatment (planning 4DCT) may not properly describe the patient motion on a different treatment day. Moreover, because of the significant additional dose released into the patient, it is possible to acquire a limited number of 4DCTs. Usually, only planning or weekly 4DCTs are acquired.
Treatment adaptation strategies were also developed to account for the impact of motion irregularities that occur during treatment delivery and that are not available at the planning stage [125], [126], [127].
The interplay, deriving from the interaction of two motions, is an intrinsically random effect. Interplay doses are characterized by hot-spots and cold-spots that mainly degrade target coverage but can also result in unwanted overdose of the surrounding normal tissues. Because of its randomness, interplay doses tend to converge to the 4DD when multiple deliveries or fractionation are considered via D4D doses accumulation.

3.5.2 Lung modulation doses

The lung modulation effect is the other cause of dose degradation considered in this study. The modulation physical and radiobiological impact, as well as its mathematical representation, are described in detail in section 2.3.2.
The mathematical description enables the reproduction of plan degradation in dose calculation engines, through two distinct methods. The first method is based on the manipulation of the input image. A new CT is produced by changing the density value of all the voxels that belong to a specific VOI, usually the lung structure. This procedure is repeated multiple times (~100) for statistical purposes and generates several images of the same patient. The newly assigned density for each voxel follows a Gaussian distribution, in which the kernel is determined from the original voxel density and the assigned Pmod. Therefore, following this method and predefining a Pmod, any image can be manipulated to reproduce the lung modulation dose degradation. This method, based on target image manipulation, was implemented both in MC based dose engine [52] and in deterministic pencil beam algorithms [128].
The second method, instead, manipulates the BP curves to reproduce their degradation downstream of heterogenous materials. A direct convolution between the unperturbed BP and a Gaussian function is performed in each voxel, based on the total path-length through the modulating material and the assigned Pmod (see Equation 2.10). The total path-length is a voxel-specific quantity extracted with ray-tracing algorithms, which implies that for each dose

calculation point a unique convolution is performed. Thus, the whole process is time-consuming and computationally demanding, depending on the depth in the patient, dose grid resolution and target volume.
This second approach was chosen for the implementation of lung modulation doses in TRiP98 [54].
The modulated doses are obtained following these steps:

1. Voxels in the density range -900 HU to -500 HU are identified as lung parenchyma.
2. Constant Pmod value assigned to each of the identified voxels.
3. Gaussian modulation function constructed from $\sigma(z) = \sqrt{P_{mod} * t(z)}$ (see Equation 2.11), where t(z) is the WET of lung tissue traversed by the beam.
4. Convolution between the Gaussian kernel and the pristine BP (at depth z) to obtain the modulated dose.

Lung modulation doses were implemented for the first time in biological dose computations in TRiP98. To generate modulated RBE-weighted doses, the convolution has to be performed for the full particle energy spectrum, which further increases the computational time. To make the process more efficient, the convolution in each spot of the dose grid is performed with the dose-averaged α, β and LET distributions. To further improve the calculation speed, a Fast Fourier Transform (FFT) was employed to carry out the convolution. It was possible to exploit the symmetries of the FFT, because of the involvement of real valued functions, evaluating two functions in a single FFT operation. The possibility to account for the lung modulation effect in biological doses becomes significant for heavy-ion therapy, like CIRT, due to its non negligible radiobiological effect [54].
This approach, based on pristine BP manipulation, has the advantage of reproducing the degradation model already at the optimization step, also enabling its compensation.

Both methods rely on *a priori* determination of the lung Pmod. From porcine lung experiments and micro-CT simulation studies, plausible Pmod values for the human lung tissue were found in the order of 50-300 μm [49] (see section 2.3.2 Protons and carbon ions in lung tissue). However, this approximation might not be representative of the patient-specific case. As previously described, the modulation strength of a material directly depends on the heterogeneous structure size, and the resulting modulation effect increases with the size of the heterogeneities. In clinical applications, the CT resolution, in the order of few millimeters, makes it possible to resolve the biggest air cavities responsible of larger dose degradation. Therefore, the most relevant modulating structures are considered in TPS for plan optimization and dose calculation purposes [129].
In contrast to the interplay, the lung modulation effect systematically affects the dose distribution in multiple treatment fractions. Thus, the dose distortion accumulates over the treatment course, increasing its harmfulness for a larger number of fractions.

The last fundamental step of treatment planning is the plan quality evaluation. Regardless of the optimization and dose calculation method, plan quality needs to be assessed either for plan approval in clinical practice or for treatment strategy evaluation and comparison in simulation studies.

3.6 Plan quality evaluation

Treatment planning is a complex process which goal is the definition of the optimal plan. A radiation oncologist defines the prescribed dose to be conformally delivered to the target, as well as the limit doses that the surrounding OARs can receive. This prescription guides the plan optimization process, and a comprehensive plan quality evaluation is paramount before the plan can be delivered to the patient.

Plan quality evaluation also plays an important role in treatment planning studies, where treatment strategies are compared with each other and/or with the state-of-the-art method.
Qualitative and quantitative analyses are performed to assess the quality of a treatment plan, both in terms of plan conformity and plan robustness [130], [131], [132].
Plan conformity is evaluated in relation to target and OARs dose. A qualitative analysis is based on visual verification of the volumetric dose distribution on patient CT. This is usually done via slice-by-slice evaluation in sagittal, coronal, and axial view, which serve as an intermediate between 2D and 3D distributions. This allows for a direct plan quality analysis, and the localization of eventual hot- and cold-spots. In this thesis, the qualitative plan QA was performed in 3DSlicer.
The dose volume histogram (DVH) is a 2D representation of the 3D dose distribution. Dose values are plotted against target and OARs volumes either in absolute (Gy and cm^3) or in relative (%) units. Dosimetric metrics are extracted from the DVH and usually expressed as the dose released to a specific VOI volume (Dyy) and the volume that receives a specific dose (Vxx). Metric examples for the target are $D_{95\%}$, $D_{50\%}$ and $V_{95\%}$ for target coverage, Conformity number (CN) and Homogeneity index (HI). CN was defined by Van´t Riet et al. in 1997 [133] as:

$$CN = \frac{V_{T,P}}{V_T} \times \frac{V_{T,P}}{V_P} \quad (3.17)$$

$V_{T,P}$ is the portion of the target volume that receives a dose equal to or greater than the prescribed one, V_T is the target volume and V_P is the total volume that receives a dose equal or greater than the prescribed one. A CN equal to 100% represents perfect target coverage. The normal tissue irradiation is intrinsically included through the term $V_{T,P}/ V_P$. Usually, the isodose line at 95% of the prescribed dose is set as lower limit to define the dose delivered and received by the target volume [133].
HI can be expressed as:

$$HI = D_{5\%} - D_{95\%} \quad (3.18)$$

HI permits to identify hot- and cold- spots inside the target. Low $D_{95\%}$ values occur in the presence of target underdosage, while $D_{5\%}$ increases in presence of target hot-spots. Therefore, for highly homogeneous plans an HI of 0 is returned, meaning that the prescribed dose is perfectly delivered to the target volume. The maximum HI value threshold is usually set to 10%.
The lower limit threshold of $D_{95\%}$ and $V_{95\%}$ is usually set to 95% or 98%, to ensure proper tumor control.
The OARs constraint definition used in this work refers to the "Quantitative Analyses of Normal Tissue Effects in the Clinic" (QUANTEC) studies that provide anatomical structure clinical tolerances based on DVH metrics [134]. This thesis refers to the work from Marks et al. [135] that proposes a "clinician's view" on using the QUANTEC. The reference metrics can define either a mean dose or a maximum dose, depending on the OARs classification into parallel and serial organs. An organ is considered parallel if it loses its functionality when the whole volume, or at least the majority of it, is damaged. In this case a dose constraint is set to the mean dose. Conversely, for a serial organ, the damage to a small volume can already compromise the functionality of the whole structure. The metric of interest is therefore the maximum dose. The lung is an example of a parallel organ, and the reference metric is the V_{20Gy} to assess mean ipsi- and contra-lateral lung dose and should not exceed 30%.
The heart is considered a mixed organ, since some of its substructures show serial behavior, but as a whole it is considered a parallel organ. For this second case, the average dose metric V_{25Gy} is used, and the upper limit is set to 10%.
The presented OARs constraints were defined for the standard 2 GyRBE/fraction in a treatment of 30 fractions. In this work, 3 GyRBE/fraction dose delivered in 20 fractions was optimized. Although the same total dose of 60 GyRBE is achieved, a larger single fraction dose is more effective, increasing tumor control but also normal tissue

toxicity. Therefore, the 20 Gy and 25 Gy dose lung and heart limits were converted into the correspondent values of the fractionation scheme used in this work. The conversion is based on the Equivalent dose in 2Gy fraction (EQD2) formula [33]:

$$EQD2 = D\frac{d+\frac{\alpha}{\beta}}{2+\frac{\alpha}{\beta}} \quad (3.19)$$

Where D is the total dose and d is the single fraction dose.
In this thesis, an $\frac{\alpha}{\beta}$ of 2Gy was assigned both to the tumor and the OARs, and the EQD2 inverted formula was used to derive the new dose limits of 16 GyRBE and 20 GyRBE for lung and heart, respectively.

The DVH and extracted metrics are used for quantitative plan quality assessment, but the spatial information is lost. Therefore, both the qualitative and quantitative methods are necessary for a comprehensive analysis.

A high-quality plan also has to show robustness against multiple sources of error, such as set-up, intra- and inter-fraction motion uncertainties. The usual approach is based on the definition of CTV to PTV expansion margins. This can be done either prior to plan optimization or can be included in the optimization algorithm by means of robust optimization (see section 3.4.1 Robust optimization). Regardless of the chosen method, it is possible to perform a robustness analysis (RA), evaluating how the dose distribution changes in each of the error scenarios, compared to the nominal dose distribution. Therefore, a plan is considered robust if both target dose conformity and OARs constraints are met in all of the evaluated scenarios.

4 Clinical impact of the lung modulation effect in carbon therapy of lung cancer

4.1 Experimental validation of lung modulation radio-biological effect

4.1.1 Introduction

Material inhomogeneities have been investigated as a source of uncertainties in particle therapy as early as 1986 [46]. In thoracic treatments, the highly heterogeneous lung tissue microstructure causes changes in the energy spectrum which broadens the sharp BP. As described in section 2.3.2.1 Physical impact, the density inhomogeneities along the beam path produce a degraded dose distribution with reduced target dose and broadened dose distal to the target [14], [46].

The higher biological damages induced by heavy ions deserves particular investigation in the presence of dose deposition uncertainties. As described in section 2.3.2.2 Radiobiological impact, the lung modulation effect causes a shift in depth of the primary high-LET carbon ions [55], which implies a consequent shift of the RBE maximum [54]. This represents a potential underestimation of the damage to normal tissue located at the distal edge of the tumor. While the modulation effect on the absorbed dose has been studied and its modelling was experimentally validated, the additional effect of altered RBE patterns remains understudied.
The radio biological effect and its potential harm to normal tissues can be validated through cell survival experiments. Cell irradiation downstream of porous lung substitute material experimentally reproduces the RBE-weighted dose, LET, and RBE degradation allowing to assess the impact on cell survival. By comparing cell survival after reference and modulated dose depositions, the radio biological impact of the modulation effect can be reproduced and quantified.

4.1.2 Materials and methods

Experimental setup

The radio-biological effect of carbon ions in presence of lung substitute materials was investigated through V79-4 (Chinese hamster lung fibroblast) cell survival experiments performed at MIT and simulated with GSI TPS TRiP98, for comparison.

In Figure 4.*22*a the experimental setup and its reproduction in 3DSlicer are shown. Two cell phantoms [136] were used for cell irradiation, allowing to simultaneously irradiate multiple slides with cell monolayers at different depths of the carbon ion SOBP. The phantom is a 5 cm x 10 cm x 16 cm acrylic glass (density 1.16 g/cm^3) box with frontal and distal (in beam direction) walls of 5.9 mm thickness and lateral holders to fix a maximum of 30 polystyrene (density 1.04 g/cm^3) cell slides. Each slide has a thickness of 1.2 mm and the distance between two slides is 3.8 mm, which defines the minimum phantom resolution in depth of 5 mm.

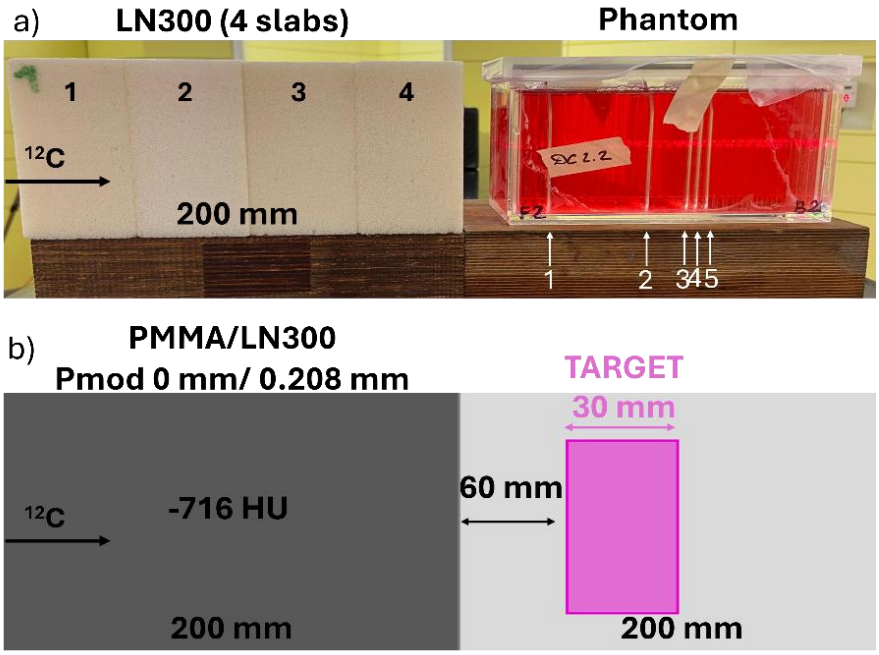

Figure 4.22 Experimental setup (a) and its reproduction in 3DSlicer (b). The experimental setup comprises four slabs of lung substitute material (LN300), for a total of 200 mm, placed in front of the cell phantom. Five cell slides are positioned in the phantom at different depths along the beam axis. For plan optimization, a CT with two sub-volumes was created. The first 200 mm reproduce the LN300 slabs (-716 HU) with an assigned Pmod of 0.208 mm [50]. The following 200 mm of water-like voxels (0 HU), reproduce the phantom, medium and cells. The carbon ion SOBP was optimized in TRiP98 on a target of 30 mm length and placed 60 mm in depth in the water-like CT.

A reference and a degraded SOBP were used to irradiate V79-4 cells, and the survival curve differences were investigated. As shown in Figure 4.*22*a, dose modulation was produced by delivering the reference carbon SOBP through 200 mm (4 slabs of 50 mm thickness) of the commercially available Gammex LN300 porous lung surrogate material (density 0.3 g/cm^3), with an experimentally calculated Pmod of 0.208 mm [50], [54]. Polymethyl Methacrylate (PMMA) with the same total WET (60.1 mmH_2O) of the LN300 slabs was employed in unmodulated dose profile irradiations.

TRiP98 simulations

The experimental setup was reproduced in TRiP98 and displayed in 3DSlicer (see Figure 4.*22*b) to prepare a carbon ion SOBP plan for the experiment, as well as predict its outcome. For this purpose, a CT with 2 mm x 2 mm x 2 mm voxel resolution was generated and divided in two main volumes of length 200 mm each. A density of -716 HU was assigned to the first volume, reproducing lung substitute characterization as performed by Paz et al. [54], followed by 200 mm of water (0 HU) representing phantom, medium and cell density. The SOBP was optimized on a 37 mm x 64 mm x 30 mm target structure placed at a depth of 60 mm in the water-like volume.

SOBP optimization for 5 GyRBE dose (10% V79-4 expected survival [137]) was performed, considering a 3 mm ripple filter and MIT beam physical characteristics. The optimized 30 mm-wide-SOBP is characterized by 18 IESs with energies ranging from 258 to 294 MeV/u. The RBE of carbon ions was reproduced through LEM IV tables calculated from photon V79-4 cell survival curves, for a total α / β of 2.79 Gy (α = 0.067 Gy^{-1}, β = 0.024 Gy^{-2} see Figure 4.28). To consider the previously measured uncertainties in the V79-4 cells response to the X-rays [137], [138],

[139], resulting in fluctuations of respective α and β coefficients, additional four RBE tables were calculated. A new plan was optimized for each of the new tables, and the resulting survival curves were compared to the experimental results. To obtain these RBE tables, the α parameter was detuned from photon survival data after varying it by ±10% and ±45%, and the new β parameters were then extracted from the resulting survival curves.
After SOBP optimization, dose calculations were performed in TRiP98 on a 1 mm x 1 mm x 1 mm dose grid. The modulated dose was calculated by assigning a Pmod of 0.208 mm to the virtual LN300 and then compared with the reference dose. Together with absorbed and RBE-weighted dose profiles, TRiP98 output includes RBE as well as survival distributions.

Cell processing

Cell plating was conducted approximately 24 h before irradiation, plating 50,000 V79-4 cells inside a 0.5 ml drop of medium at the center of each slide. After cell attachment, DMEM growth medium [Gibco™ number 31966021] supplemented with 10% fetal bovine serum and 1% penicillin-streptomycin was added to prevent cells from drying. On the day of irradiation, a total of five cell slides were inserted in each phantom into the desired slots (see Figure 4.*22*); afterwards, the phantom was filled completely with DMEM medium and sealed using Parafilm M tape to ensure sterility during the irradiation. Between irradiations, the medium in the phantom was exchanged before inserting the new cell slides. After each irradiation, the slides were extracted from the phantom, rinsed with buffer solution and incubated with 1 ml of Trypsin for 5-8 minutes to allow the cells to detach. Following that, the cell suspension from every slide was prepared by collecting the cells and transferring them into respective 15 ml Falcon tubes containing 3 ml of DMEM medium each. Cell concentration was counted using the Casy counter. Lastly, cells were re-seeded in triplicates (biological replicates) into 25 cm^2 flasks pre-filled with 5 ml of medium and were left to incubate for 7 days for a colony forming assay. The number of cells to be re-seeded, for each position of the slide in the phantom, was based on expected survival values, extracted from TRiP98 simulations (Figure 4.*25*a) and the expected value of plating efficiency (0.7).

Dosimetry

Prior to cell irradiation, the phantom wall, cell slides and LN300 WET were measured with a monoenergetic (199.7 MeV/u) carbon ion BP in a water column (PTW PeakFinder [140]). First, both empty phantoms were placed between the nozzle and the water column, so the resulting WET measurement included both the entrance and exit walls. Next, two cell slides were inserted into phantom #1, and the WET of the empty phantom was subtracted from the new measurement to determine the WET of the two slides. Each of the four LN300 slab were measured both individually and together. The resulting WET represents the mean (μ) of the Gaussian function in the modulation mathematical model (see section 2.3.2.1 Physical impact). With the LN300 Pmod of 0.208 mm, the standard deviation σ was extracted (see section 3.5.2 Lung modulation doses). Thus, a convolution between the measured reference BP and the Gaussian curve was performed and the result was compared with the measured modulated BP. By matching the convolved and measured curves, the Pmod value of the LN300 was verified. An additional measurement of the LN300 WET was performed right before cells irradiation, and the result was used as the reference experiment value during cell experiments.

Additionally, depth dose distributions were acquired downstream of PMMA and LN300 with an Ionization Chamber (IC) (PTW Markus Chamber) to precisely measure the reference and modulated absorbed dose profiles. A total of 15 points were acquired for each dose profile, of which five corresponded to the cell plates depths.

Cell irradiation

The position of the cell slides in the phantom was determined, prior to cell irradiation, by comparing the reference and modulated survival distributions in output by TRiP98. The modulation effect was quantified in terms of survival values to find the depth at which the maximum difference between the two plans occurs. Cell plates were then positioned at this depth and in its vicinity. A total of five cell slides were positioned in each phantom, at the SOBP entrance channel (1 slide) and plateau (1 slide) for comparison, and at the distal fall-off (3 slides), as highlighted by white arrows in Figure 4.*22*a. The fourth slide was ideally positioned at the depth where the maximum of the survival difference occurs.

At the SOBP steep distal fall-off, minimal shifts in depth result in significant dose changes. Therefore, to increase the phantom resolution in this area two different cell slide configurations, depicted in Figure 4.*23*, were defined: the first characterized by the beam traversing the slide and then the cell layer, the second with the beam traversing the cell layer and then the slide. By flipping the cell slide, it was possible to sample the survival curves, in the vicinity of the identified depths of interest with a resolution of 1.2 mm (slide thickness).

A total of eight irradiations were performed one after the other: reference (downstream of PMMA) and degraded (downstream of LN300) SOBP, for both configurations and the whole sequence was repeated twice for statistical purposes.

Differences between the reference and modulated experimental results were compared for each of the 10 depths (5 slots for 2 cell slide configurations) along the irradiation axis. The experimental results are presented at each depth as the mean and the standard error (SE) over six values, deriving from three biological replicates (see section 4.1.2) for each of the two irradiations.

The experimental results were also compared with TRiP98 simulations.

In both cases, the differences were statistically evaluated with a T-test (statistical significance for $p<0.05$).

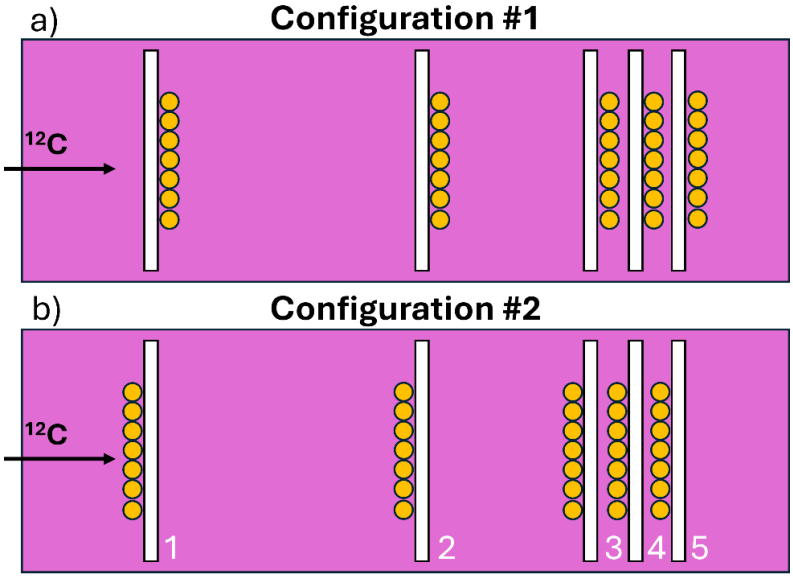

Figure 4.23 Schematic representation of cell slides configurations. In configuration #1 the beam traverses the slide and then the cell layer (a), while in configuration #2 the beam first traverses the cell layer and then the slide (b).

4.1.3 Results

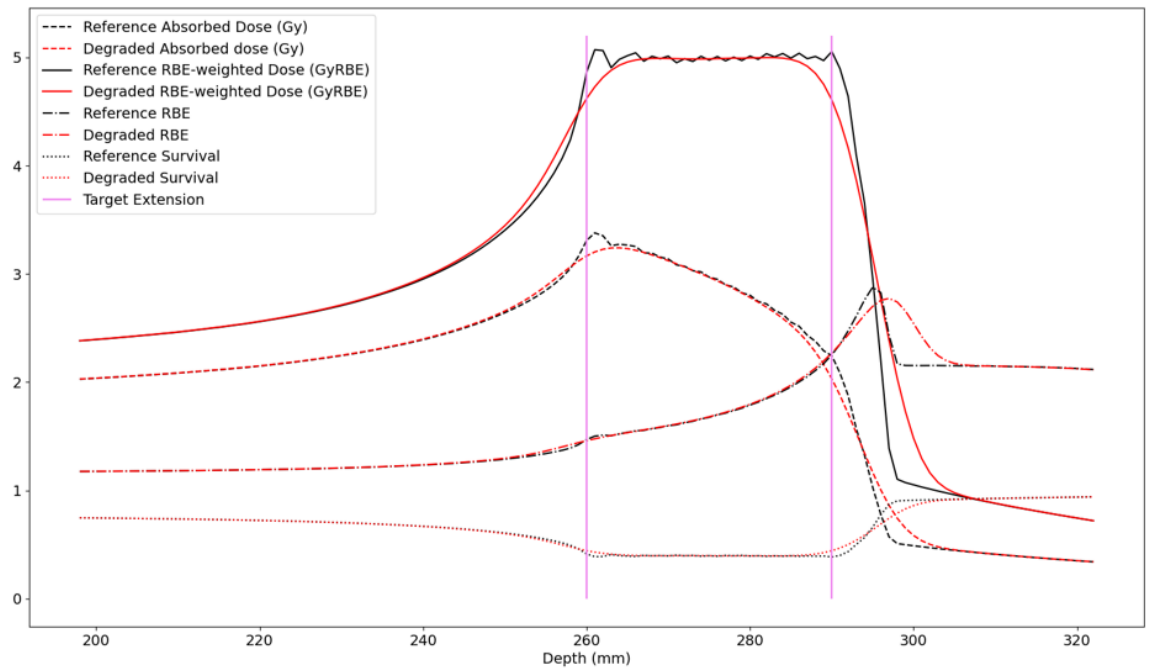

Figure 4.24 TRiP98 simulation output for the reference (black) and degraded (red) case. The RBE-weighted dose (solid line) absorbed dose (dashed line), RBE (dash-dot line) and survival (dotted line) distributions are shown. Proximal and distal edges of the target are marked with violet lines.

Figure 4.*24* shows TRiP98 absorbed dose, RBE-weighted dose, RBE and survival curves in CT geometry coordinates both for the reference and the degraded case. The modulation effect mainly affects each quantity at the target distal end and SOBP fall-off, where the reference and modulated plans show the largest difference. Particularly, the physical and biological doses decrease inside the target both at the proximal and distal edge and exhibit a broadened SOBP fall-off. Quantitatively, the distal fall-off width (DFW) is 10 mm and 12 mm for the unmodulated and modulated RBE-weighted SOBP, respectively. As shown in the RBE-weighted dose profile, the smearing effect caused by material inhomogeneities broadens each carbon BP composing the SOBP, creating a much smoother SOBP plateau. The modulated RBE distribution is broadened, its maximum decreased from 2.9 to 2.8 and shifted in depth by 2 mm. RBE and doses displacement affect the survival distribution that diminishes with respect to the reference case at the same depths where increased biological doses occur.

In Figure 4.*25* the maximum survival difference of 12.8% at a depth of 299 mm is shown together with cell plates positions from both configurations alongside the RBE-weighted dose curves.

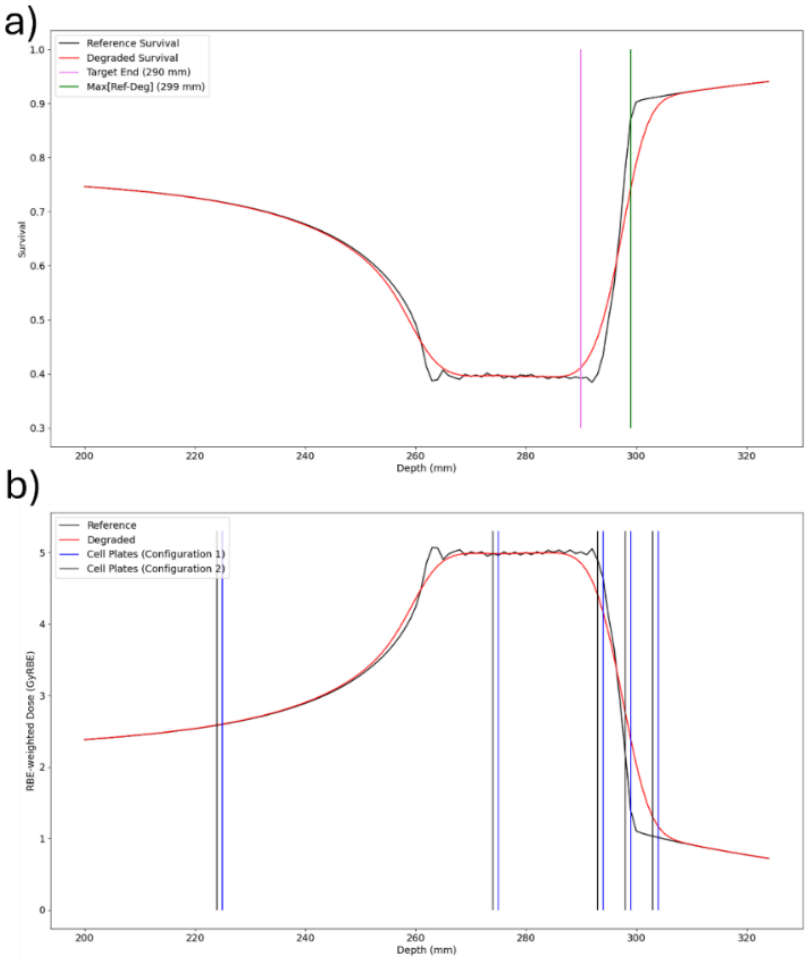

Figure 4.25 Survival (a) and RBE-weighted dose (b) profiles from TRiP98. Reference (black) and degraded (red) survival profiles compared to detect the depth at which the maximum difference occurs (green vertical line). The physical end of the target is marked with a violet vertical line (a). Starting from the maximum difference depth, the position of five cell slides was defined and plotted alongside the RBE-weighted dose profile. Both cell plates configurations (Figure 4.23) are depicted in blue (c1) and black (c2).

Water column measurements were performed prior to cell irradiations to precisely assess the WET of the different components. Table 4.*1* lists measurement results, namely the proximal (p) and distal (d) R80 (range at 80% of the peak dose), the peak depth and width (pR80-dR80) as well as the WET, calculated after beam traversal of a specific item. The four single LN300 slabs measurements returned an average WET of 14.54±0.30 mm. Then, all the slabs were positioned in front of the beam, and the measurement was repeated twice for an average WET of 59.34 ± 0.14 mm. In the last row of Table 4.*1*, the additional measurement of 20 cm LN300 performed on the day of cell irradiation is shown, for a total WET of 60.1 mm. This is the reference value used for cell irradiation. It is important to specify that the SOBP optimization was performed on the CT whose characteristics were based on results of Paz et al. [54]. Namely a value of -716 HU, corresponding to a WET of 57.6 mm, was assigned to the lung substitute material voxels. However, for the WET of 60.1 mm, 2.5 mm larger than the result of Paz et al. work, the correct CT number would be -700 HU. To compare experimental and simulated results (see Figure 4.*29*), survival curves were re-calculated on a new CT phantom with the correct HU values.

Measurement	Proximal (p) R80 (mm)	Distal (d) R80 (mm)	Peak (mm)	Width [pR80-dR80] (mm)	WET [dR80ref-dR80] (mm)
Phantom #1	71.96	72.57	72.25	0.88	13.58
Phantom #2	71.58	72.47	72.13	0.89	13.68
2 slides (in Phantom #1)	69.05	69.93	69.61	0.88	16.22
LN300 1	64.41	69.47	67.49	5.06	15.06
LN300 2	65.33	70.26	68.35	4.93	14.27
LN300 3	65.14	70.15	68.12	5.01	14.38
LN300 4	64.9	70.05	67.98	5.16	14.48
LN300 1-4	15.65	25.29	21.31	9.64	59.24
LN300 1-4	15.77	25.09	21.01	9.32	59.44
LN300 1-4	16.0	26.05	22.33	10.05	60.1

Table 4.1 Water column measurement results. Peak Finder measurement returns proximal (p) and distal (d) range at the 80% of the maximum (R80), from which the peak width (pR80-dR80) is calculated. WET of the phantoms (#1 and #2), cell slides, single and combined LN300 slabs were measured as difference between dR80 of the reference BP (dR80ref) and specific dR80. In the last column the total LN300 WET measured before cell irradiation is given. This value was used for cell slides positioning.

Water column results are shown in Figure 4.*26* for LN300 slab 1 measurement (row 5 of Table 4.*1*) and slabs 1-4 (row 10 of Table 4.*1*). The reference BP is depicted alongside the reconstructed Gaussian curve which kernel is obtained as described in Figure 4.*26* and in section 4.1.2 Materials and methods. The result of the convolution and the degraded BP, acquired downstream of the LN300 samples, are in perfect agreement, confirming the material Pmod of 0.208 mm. The Gaussian kernel quantifies the BP distal fall-off shift (μ) and broadening (σ), and the DFW was also calculated (dR20-dR80) resulting in 1.38 mm, 2.96 mm and 5.82 mm for the reference, the 1 slab and 1-4 slabs BPs, respectively.

In Figure 4.*27* the IC acquisition results are compared with the TRiP98 simulation outcome. The TRiP98 reference absorbed dose profile is in perfect agreement with the experimental data, while a 2% amplitude difference was found when comparing measured and simulated values at the degraded SOBP fall-off. This might derive from the LN300 material characterization, and the density assigned to the LN300 CT in TRiP98. If a denser material is placed in the beam path, not only is the particle range smaller, but also the dose is reduced because of the increased stopping power and scattering [141]. The variations in WET that were found between multiple water column measurements reflect the LN300 density uncertainty.

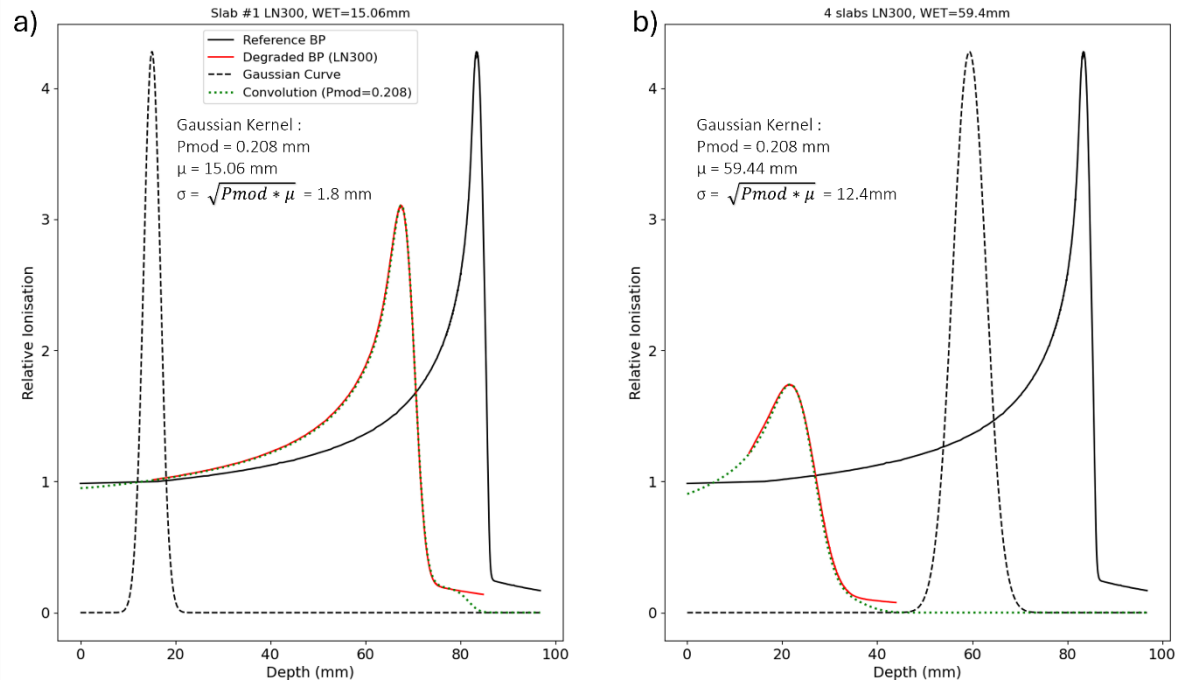

Figure 4.26 Water column measurements of LN300 slab 1 (a) and 1-4 slabs (b). For both cases the reference BP (solid black) is plotted alongside the degraded BP (dotted green), the Gaussian curve (dashed black) and the convolution result (red solid). The superposition of the calculated and measured degraded curve confirms the LN300 Pmod of 0.208 mm.

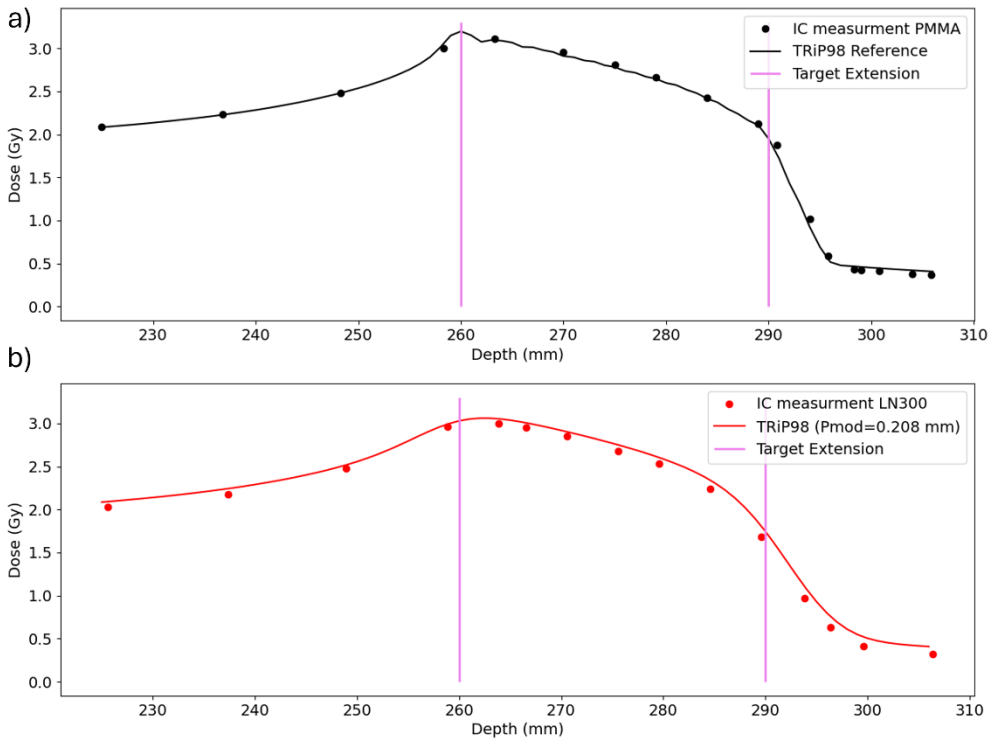

Figure 4.27 IC measurements results. The reference (a) depth dose distribution from TRiP98 is plotted alongside the acquired points, measured downstream of PMMA plates. Same comparison is shown for the degraded (red) depth dose distribution, measured downstream of the LN300. A 2% amplitude difference was found between measured and simulated dose profiles. Target extensions are marked with violet vertical lines.

The experimentally defined variability of the radiosensitivity of V79-4 is accounted for by deriving multiple α/β values and corresponding RBE tables. Figure 4.*28*a shows the linear (α) and quadratic (β) components as well as the corresponding survival as a function of dose, which values are listed in Table 4.*2*. Correspondent RBE tables were created in LEM IV and used to calculate survival distributions in TRiP98 as a function of depth (see Figure 4.*28*b). For α ±10% cases, the survival changes in the SOBP plateau are within 1%, while starting from a reference survival of 40%, the values become 45% and 39% for α ±45%, respectively.

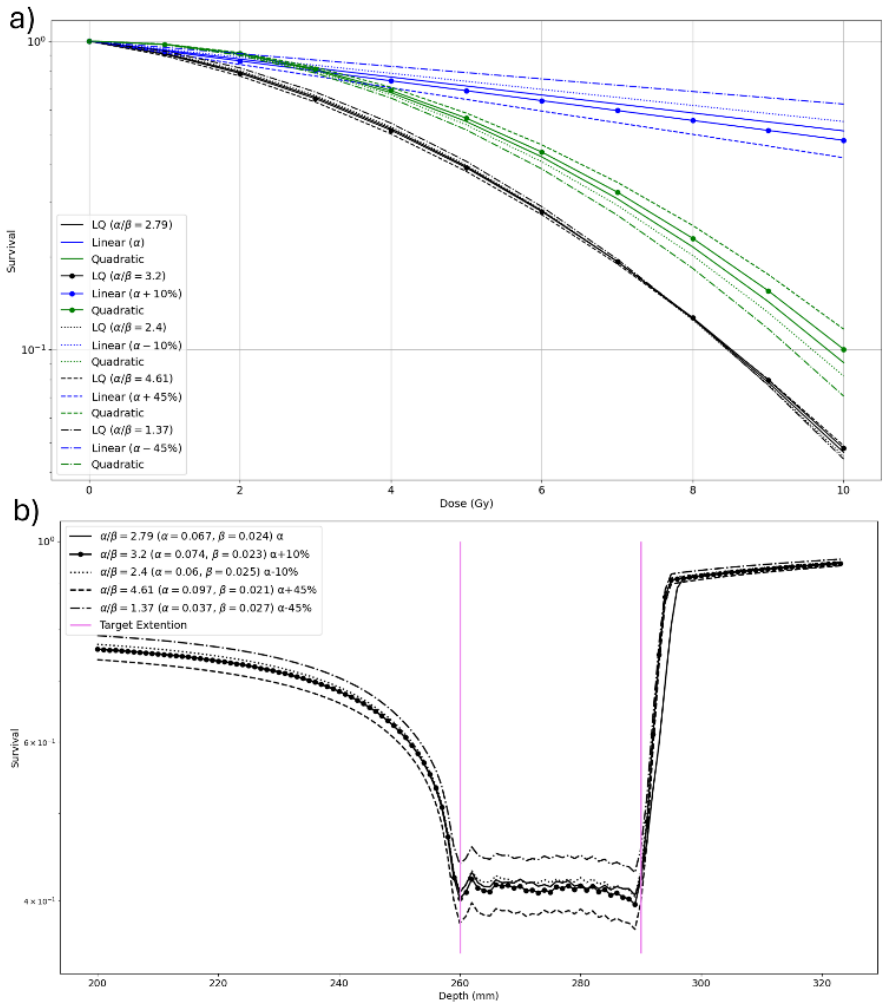

Figure 4.28 V79-4 survival curves for different LQ model parameters, as a function of dose (a) and depth (b). The reference linear parameter α was extracted from photon experiments. A variation of ±10% and ±45% was applied to α (blue) and used to derive the quadratic parameter β (green) and the survival as a function of the dose (a). RBE tables were computed in LEM IV from the new LQ parameters and the resulting survival TRiP98 curves are plotted as a function of depth (b). Target extensions are marked with violet vertical lines. LQ=linear quadratic.

	Linear α (Gy^{-1})	Quadratic β (Gy^{-2})	α/β (Gy)
Photon experiments	0.067	0.024	2.79
α+10%	0.074	0.023	3.2
α-10%	0.06	0.025	2.4
α+45%	0.097	0.021	4.61
α-45%	0.037	0.027	1.37

Table 4.2 V79-4 LQ model parameters for the reference case (photon experiments) and the additional cases computed varying the linear component (α) by ±10% and ±45%. The corresponding quadratic component (β) was detuned from the survival of the photon experiment.

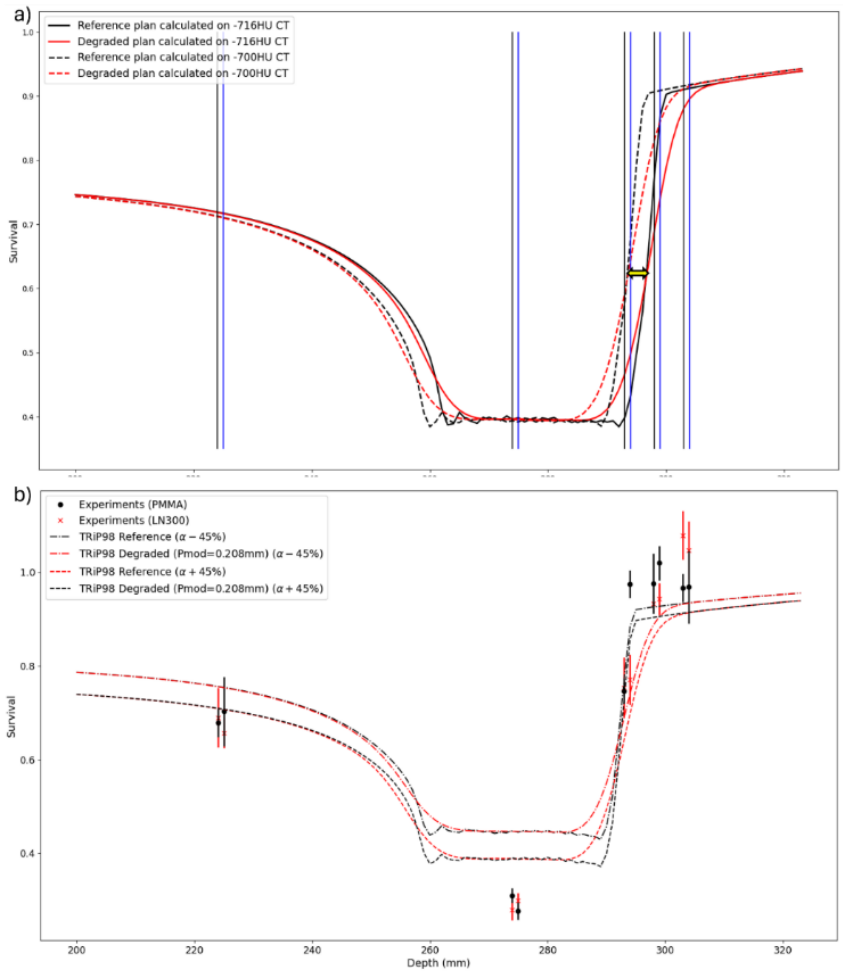

Figure 4.29 Survival experiment results compared with TRiP98 prediction. Survival curves calculated in TRiP98 on the planning CT (-716 HU) and the updated CT (-700HU), matching the WET of 60.1 mm (a). Reference (black) and degraded (red) survival for extremes of the RBE tables range (α±45%, see Table 4.2), plotted alongside experimental results (b). Average and standard error (SE) over six values (experiment repeated twice, three biological replicates per slide) for ten depths (5 slides, 2 configurations). Values are listed in Table 4.3.

Figure 4.*29* shows experiments results compared with TRiP98 survival prediction. Survival curves calculated on the planning CT (-716 HU) and the updated CT (-700 HU), matching the reference WET of 60.1 mm, were compared.

Experiment and simulation values are listed in Table 4.*3*, for each phantom slot (numbered from 1 to 5) and for both cell slides configurations (see Figure 4.*23*).
No modulation effects were found at the entrance channel (slot 1), and a good agreement exists between experimental and simulated data. However, a 10% difference occurs in correspondence of the SOBP plateau (slot 2), between TRiP98 and the experimental outcome. The experimental data show enhanced differences between the two configurations at slot 3, which is most likely due to the steepness of the distal fall-off. Particularly, at depth 293 mm (c2) the reference and degraded results are identical, while a difference of 20% (from 97% to 77%) occurs 1 mm deeper (c1). Notably, the maximum survival difference of 12.8%, calculated by TRiP98, was expected to occur at depth 299 mm, 5 mm deeper than what was found experimentally. At slot 4, TRiP98 plans difference is in the order of 5% and 3% for configurations 2 and 1, respectively. This difference was no longer present at slot 5. Discrepancies between TRiP98 results and the experimental data also occur at slots 4 and 5. The magnitude of this difference is about 7% and 5% for the reference case of slots 4 and 5, respectively. It changes to 5% and 9% for the modulated results at slot 4 and 5, respectively. None of the differences between reference and degraded cases, as well as the simulated and acquired results, were statistically significant ($p>0.05$).

Depth (mm)	Phantom slot, Configuration	Experiment Reference (AV±SE)	Experiment Degraded (AV±SE)	TRiP98 Reference (Range)	TRiP98 Degraded (Range)
224	1, c2	0.68±0.03	0.69±0.06	0.71-0.76	0.71-0.76
225	1, c1	0.70±0.07	0.66±0.03	0.71-0.76	0.71-0.75
274	2, c2	0.31±0.02	0.28±0.02	0.40-0.45	0.39-0.45
275	2, c1	0.28±0.02	0.30±0.01	0.39-0.45	0.39-0.45
293	3, c2	0.75±0.03	0.75±0.06	0.73-0.77	0.64-0.69
294	3, c1	0.97±0.03	0.77±0.05	0.86-0.88	0.70-0.74
298	4, c2	0.98±0.06	0.93±0.02	0.90-0.93	0.86-0.89
299	4, c1	1.02±0.04	0.94±0.03	0.91-0.93	0.88-0.90
303	5, c2	0.97±0.03	1.08±0.05	0.91-0.93	0.91-0.93
304	5, c1	0.97±0.08	1.05±0.06	0.91-0.93	0.91-0.93

Table 4.3 Experiment and TRiP98 survival values listed for each phantom slot (numbered as in Figure 4.23) and for both cell slides configurations (c1 and c2). The experiment results are reported as average (AV) and standard error (SE) over six values. TRiP98 results for the RBE tables extremes range (α±45%, see Table 4.2) are listed.

4.1.4 Discussion

In this work, the radiobiological effect of lung modulation was experimentally validated. The shift in penetration of primary carbon ions and the consequent broadening of RBE maximum are potentially dangerous for the normal tissues at the tumor distal edge. To evaluate the measurable impact of these effects on the biological effectiveness of CIRT, this thesis conducted cell survival experiments under simple and well-controlled conditions. Survival experiments were performed at MIT, irradiating V79-4 cells in a carbon ion SOBP. To simulate therapy conditions, a cell phantom, enabling simultaneous irradiation of multiple cell slides at different depths, was used. 20 cm LN300 lung substitute material was employed to reproduce SOBP degradation and the SOBP optimization was computed in TRiP98, together with RBE-weighted dose, absorbed dose, RBE and survival distribution calculations. The latter were compared to cell survival experiment outcome. In addition, this work included the uncertainty in the intrinsic radiosensitivity of V79-4 cells into the analysis by using a range of α/β ratios for the RBE calculation.

LN300 lung substitute material was previously used to reproduce the heterogeneity of lung tissue [50], [54], [55]. Particularly Paz et al [54], utilized the same LN300 slabs used in this experiment and characterized them with a total WET of 57.6 mm and a Pmod of 0.208 mm. Performing water column experiments, a WET of 59.4 mm and 60.1 mm in multiple repetitions were obtained. Notably, the last value, used for conversions in cell irradiation experiments, differs by 2.5 mm from the result of Paz et al. A 0.7 mm discrepancy was also found between measurements performed on different days. This is probably due to the multiple paths particles can take inside the porous material, defining a different WET already during the same experiment, as well as measurement errors between different experiments. A Pmod of 0.208 mm, obtained as described in the work by Ringbaek et al [50], was confirmed by the water column experiments.

The impact of the modulation effect on cell survival, caused by the shift in depth of high-LET primary carbon ions, was mainly investigated in this work. The experiment results show no differences between reference and degraded survival at the entrance channel, the SOBP plateau, and where the two curves cross (293 mm), right after the end of the target. However, only 1 mm more in depth (294 mm), cell survival decreases from 97% to 77%. This is due to the modulation effect, as predicted by the simulations and previously investigated [54], [55], but such a large difference also derives from the superposition of biological and positioning errors as discussed below. The survival values converge further along the SOBP tail.
The same trend is observed in TRiP98 survival curves, but a mismatch happens between the simulated and the experimental data. From TRiP98 simulations, the maximum survival difference of 12.8% is found at depth 299 mm, where also one of the cell slides was placed. However, the experiment results show a maximum survival difference of 20% at depth 294 mm. The results indicate that TRiP98 simulations may underestimate the effect of lung modulation on cell survival, net of biological and positioning errors.

TRiP98 calculations were performed on a CT of which the characterization was based on the WET measured by Paz et al., therefore the planned positions underestimated the target location of the largest survival difference. The 2.5 mm difference in WET values contributes to the 5 mm shift between survival maximum difference depth calculated in TRiP98 and those resulting from the experiment. The remaining 2.5 mm can derive from multiple sources of uncertainty: biological uncertainties, positioning error and biophysical model inaccuracy.

The biological uncertainties always play a significant role in cell experiments, and to reduce their impact, the full experiment was repeated twice on the same day, and from each irradiated cell slide three biological replicates were obtained.

The setup and positional errors, because of the extremely steep gradient at the SOBP distal fall-off, could highly affect the result too. At the target distal edge, 1 mm variation in depth can cause up to a 5% difference in cell survival. Ideally, to obtain a finely sampled survival curve, cell plates should be positioned at 1 mm intervals along the depth. To increase the resolution at the depths of interest two cell plate configurations were used. An even finer resolution could have been achieved by placing thin (~ 1 mm) PMMA slabs in front of the phantom to shift in depth the whole dose profile. However, to avoid multiple setup changes, the cell slides within the phantom were flipped, thus reducing the possibility of positioning errors deriving from variations of the material placed in the beam path. In addition, to perform a large number of cell irradiations, implies that cell processing and data analyses workload increases proportionally.

Ultimately, the simulated and experimental data mismatch could derive from inaccuracies of the biophysical model used to simulate V79-4 cell line radio biological behavior. The V79-4 cell line photon response has been investigated in multiple studies [137], [139], and summarized in the PIDE database [138]. Results show the high variability of α/β

values varying from 2.8 Gy [142] to 23 Gy [139]. The α and β parameters, and derived reference RBE tables, were obtained from photon experiments performed at MIT with the same V79-4 cells used for the irradiations of this work. This was important to minimize potential sources of error deriving from different biophysical maintenance conditions in the laboratory. The obtained α/β was in accordance with most of the reported results, but to provide a comprehensive cell line radio biological description, additional α and β parameters, and consequent RBE tables, were calculated. By applying a variation of ±10% and ±45% to the α parameter, a range of survival curves with extremes going from 39% to 45% survival in the SOBP plateau, was defined.
The V79-4 radiobiological variability increased the sources of uncertainty and affected the biophysical model precision. In a multi-center study, Sokol et al. [139] investigated V79-4 survival after proton irradiation, using the same phantom for cell positioning in the SOBP. Their results confirm the significant spread of α/β values of photon data and highlight the variability of survival results at the SOBP distal fall-off. The phantom was designed to evaluate cell survival at different depths within the SOBP during single irradiations. However, cell plates are typically not positioned at the proximal or distal fall-off regions due to the steep dose gradients. Nonetheless, the modulation effect, and its influence on cell survival, manifests in the distal region beyond the SOBP.

It is also important to comment on the observed survival values greater than 1 at slot 4 and 5, indicating an increase in cell survival, as it would not be expected after cell irradiation. This typically derives from inherent biological variability in radiobiology experiments, particularly when high biological uncertainty is not mitigated by a sufficiently large sample size. To address this, the experiment was repeated twice, with three biological replicates per cell plate, yielding a total of six data points for each depth of interest.
In addition, these results can be attributed to positioning inaccuracies. The number of cells seeded in each plate was determined based on expected survival values obtained from TRiP98 simulations (see section 4.1.2 Materials and methods). However, the expected survival is directly related to the expected dose at a specific depth, and any deviation from the planned position would affect the delivered dose. Specifically, if a cell plate was placed more in depth than planned, it would have been exposed to a lower dose, leading to increased cell survival.
While biological or procedural errors cannot be excluded, the increased radioresistance (IRR) effect also represents a possible explanation [143]. The IRR effect was described for low-dose ranges (0.5–1 Gy), which correspond to the dose values experienced by cells in the most distal cell plates (located ~10 mm beyond the target). IRR describes a radiobiological effect in which cells, exposed to small radiation doses exhibit enhanced resistance. Since the initial cell seeding density and survival outcomes are normalized for the baseline radioresistance of V79-4, namely the plating efficiency (0.7) calculated after photon experiments (see section 4.1.2 Materials and methods), an increased radioresistance due to the IRR phenomenon could inflate the final survival values above 1.

Notably, both the simulated and experimental data show an increased cell mortality at the distal edge of the target caused by beam degradation. Nevertheless, this effect was not statistically significant and a good agreement between simulated and experimental survival trends could not be found.

The goal of this study was to assess and quantify the harm to normal tissue cells distal to the tumor, and its potential impact in a real clinical scenario. However, some limitations are present. In the patient's body, the target would be surrounded by lung tissue and would be only few cm deep inside the lung. Furthermore, treatment plans are optimized and beam directions chosen to minimize the length of the path particles take inside the lung. In this experiment, a total of 20 cm LN300 material was employed to enhance the degradation effect, in the attempt of overcoming the intrinsic biological uncertainties of cell experiments. Therefore, it is important to investigate the actual clinical effect in treatment planning studies, like the one presented in section 4.2 Dosimetric study of lung modulation and interplay effect, that comprehensively reproduces the lung modulation in patient-like scenarios.

4.1.5 Conclusions

We performed lung fibroblast survival experiments, with carbon beam irradiation downstream of LN300 lung substitute material to experimentally reproduce the lung modulation effect. Survival experiments were compared to TRiP98 simulations, to validate the radiobiological model of the modulation. Both TRiP98 and experimental results highlight a cell survival decrease a few mm after the SOBP end, at the distal fall-off. However, relevant differences were observed between survival experiments and simulations, both in the total effect magnitude and its location along the SOBP fall-off. Multiple sources of uncertainties have been identified but a good agreement between TRiP98 outcome and experimental data could not be found. Nevertheless, the survival experiment results confirm the increased mortality in the distal region of the SOBP, where primary carbon ions are shifted in depth towards the normal tissue distal to the target.

The observed survival reduction was not statistically significant and therefore it does not allows any conclusion as to whether the modulation effect would or would not be harmful in a real clinical scenario. Moreover, other meaningful sources of error, such as target motion, would be present and would interact with the modulation effect that was studied here in isolation. The clinical impact of lung tissue inhomogeneities and its combination with interplay effect dose degradation were investigated in a treatment planning study, presented in the following section.

4.2 Dosimetric study of lung modulation and interplay effect

A version of this section is available on ArXiv [144].

4.2.1 Introduction

The advantageous characteristics of CIRT require extremely precise and predictable dose deposition, which is impaired in lung treatments by range and energy straggling, deriving from setup uncertainties, breathing motion and lung tissue inhomogeneities. The lung modulation and interplay effects were investigated in this work as main causes of plan quality degradation.

Intra-fractional motion and the interplay effect represent the main causes of dose degradation for moving targets treated with active beam scanning particle therapy (see section 2.2 Tumor motion). Multiple mitigation techniques such as gating, breath-hold, tracking and rescanning were investigated and, with the exception of tracking, introduced in clinical practice. Patient-specific motion is accounted for in treatment planning through 4DCT (see section 3.1 Diagnostic imaging in radiotherapy), motion included target safety margins (see section 3.2 Volumes of interest), 4D optimization and dose calculation strategies (see section 3.4.2 4D optimization and 3.5.1 4D Doses).

The lung modulation effect, whose physical and radio biological aspects were comprehensively described (see section 2.3 Lung tissue inhomogeneities and 4.1 Experimental validation of lung modulation radio-biological effect), is not considered in clinical applications and only sparsely investigated in simulation studies. Dose calculation methods developed to reproduce the lung modulation effect (see section 3.5.2 Lung modulation doses) were employed in phantom studies [145] and patient CT studies [54], [128], [146] to investigate lung modulation in patient-representative scenarios. However, only Paz et al. [54] investigated carbon ion RBE-weighted doses and the modulation-associated shift of the RBE in a single patient.

Additionally, to fully model a comprehensive clinical scenario, the lung modulation effect needs to be considered also in the context of breathing motion, i.e. considering the interplay effect. To date, a treatment planning study

considering both intra-fractional motion and tissue heterogeneities is still missing but it is crucial to understand the importance of lung modulation in clinical CIRT of lung tumors. Therefore, the lung modulation model was extended to integrate it into TRiP4D, allowing us to perform such a dosimetric study [54]. Briefly, the convolution of dose-averaged α, β, and LET distributions of the reference BP with the Gaussian function is computed in each voxel for the specific depth z and the assigned breathing motion. Therefore, it was possible to compute D4D RBE-weighted doses with the superposition of the lung modulation effect. Comparing these D4D modulated doses with the D4D doses allowed to assess the combination of both effects, mimicking what would happen in a real clinical scenario.

This work presents the largest treatment planning study investigating the clinical impact of the lung modulation effect in CIRT of lung tumors. The modulating effect of lung tissue was assessed both alone and in combination with the interplay effect, as the main source of plan degradation in scanned PT of thoracic tumors, on a cohort of eighteen patients. 3D and 4D-optimizations and dose calculations were performed in TRiP4D and effect-specific parameters such as the motion amplitude for the interplay effect and the strength of the Pmod for the modulation effect, were investigated. In addition, following the phantom study by Flatten et al. [145] and the patient CT study by Ringbaek et al. [128], the correlation between target depth in lung and modulation effect amplitude was investigated.

4.2.2 Materials and method

Patient Data

The dataset comprises 4DCTs from eighteen NSCLC patients, available from "The Cancer Imaging Archive" (TCIA), an open-access database of medical images for cancer research. Patients with good quality 4DCT and contoured VOIs were selected from the "4D-Lung" collection [147]. 4DCT images with available contoured VOIs were selected. 4DCT images were acquired on a 16-slice helical CT scanner (Brilliance Big Bore, Philips Medical Systems, Andover, MA) as respiration-correlated CTs with 10 equal breathing phases (0% to 90%, phase-based binning), with slice thickness of 3 mm and 512 mm x 512 mm axial resolution (~1 mm pixel size) [148]. The field of view is 500 mm. DIR was computed in Plastimatch between the reference phase CT (end-inhale, 0% respiratory cycle) and all other 4DCT phases. DIR, based on three B-spline registration stages without preliminary RIR, returned the DVF. Targets and OARs, delineated by a single radiation oncologist, were also available for all 4DCTs. Ipsi- and contra-lateral lungs as well as the heart were evaluated for this study. The GTV position and volume together with its depth in lung are the main patient characteristics of interest for this study and are listed in Table 4.*4*. The CTV displacement was calculated as the average magnitude of the DVF correlating the target voxels from the end-inhale (0% respiratory cycle) to the end-exhale (50% respiratory cycle) phase. In addition, the distance between the GTV and the lung contour was calculated in 3DSlicer. The depth of the tumor in the lung was calculated in the central slice of the GTV in axial view of the reference phase CT. Given the complex and non-uniform geometry of the GTV, the distance in lung was calculated for each field direction.

Patient	GTV position in lung	GTV volume (cc)	CTV motion (mm)	GTV depth in lung (mm) Field1/Field2
P1	RUL	100	2.9	59/55
P2	RUL	46	6.1	59/56
P3	LUL	196	2.4	72/65
P4	LLL	40	6.0	64/48
P5	RUL	167	3.7	37/37
P6	LUL	47	3.7	0/0
P7	RUL	19	5.5	94/61
P8	RLL	23	8.3	44/46
P9	RUL	74	3.1	32/90
P10	LUL	23	3.4	10/65
P11	RUL	15	1.1	40/42
P12	Mediastinum	393	4.1	15/83
P13	RML	75	7.5	23/81
P14	RLL	118	11.9	0/82
P15	RUL	32	1.1	0/0
P16	Mediastinum	85	5.6	0/0
P17	RLL	218	9.6	16/96
P18	RUL	8	3.9	6/65

Table 4.4 Patient characteristics. The target position in the lungs, volume, motion amplitude, and distance in lung for both fields are listed. Target motion was obtained from DVF amplitude between end-exhale and end-inhale CT. The depth in lung was computed from the central slice of the GTV in the reference phase CT. RUL=right upper lobe, RML=right middle lobe, RLL=right lower lobe, LUL=left upper lobe, LLL=left lower lobe, GTV= gross tumor volume, CTV= clinical target volume.

Treatment planning

3D plans were optimized on the reference phase CT, for 3 GyRBE/fraction uniform dose to the IGTV. For a correct beam range computation, a density override was performed inside the target volume (see section 3.4.2 4D optimization). RBE distributions of carbon beams were computed with LEM I, assigning a global α/β ratio of 2 Gy. 4D-optimizations (see section 3.4.2 4D optimization) were computed on the IGTV [122] for a sub-group of eight patients that exhibited a target motion greater than 5 mm. For all plans, two coplanar fields were optimized, and robust optimization was computed with 3.5% range uncertainty and setup uncertainty varying from 3 mm to 7 mm, to define patient-specific margins. Larger margins were used to achieve proper target coverage in the presence of larger target motion and/or volume.

3D-optimized plans were computed for each patient, and used as a starting point for dose calculations, both including (modulated doses) and neglecting the lung modulation effect. The TRiP4D dose engine was employed for the computation and comparison of static (3D), 4D and interplay (D4D) RBE-weighted doses, both considering and neglecting the lung modulation degradation. A more detailed description of TRiP4D dose computations is presented in section 3.5 Dose calculation.

In particular, motion related dose degradations were quantified by comparing the 3D doses with 4D as well as D4D doses. D4D doses quantify the impact of the interplay effect, while the comparison with 4D doses permits to evaluate if the planning strategy (i.e. density override and margins) is adequate against the breathing motion alone. The comparison between 3D doses and 3D modulated doses enabled to evaluate the lung modulation effect alone.

The lung modulation model, as implemented in TRiP4D (see section 3.5.2 Lung modulation doses), is based on the application of a global constant Pmod to each CT voxel identified as lung parenchyma. In this way, the lung modulation variability over different patients and lung regions is not considered. To mitigate this approximation, lung modulation doses were computed using two different Pmod strategies:

1. Pmod of inflated lung, experimentally validated in previous studies [129], [146], [149], [150] and described by a Gaussian distribution (0.200 mm ± 0.067 mm). For a realistic assessment of the lung modulation impact, for each patient, three Pmod values were randomly sampled from this normal distribution. Results of the associated three dose calculations are referred to as "Gaussian Pmod".
2. An "Extreme Pmod" value of 0.750 mm was used to evaluate a maximum lung modulation effect, following the approach of Winter et al. in their study [146].

Furthermore, the investigation of interplay and lung modulation effects superposition was performed by comparing D4D and modulated D4D plans.

Ultimately, 3D and 4D-optimization strategies were compared in terms of 4D doses as well as D4D and D4D modulated doses.

Data analysis

Plan evaluation was performed both qualitatively and quantitatively, as described in section 3.6. Metrics of interest were $D_{95\%}$, the mean dose $D_{50\%}$, $V_{95\%}$ and HI to quantify the target coverage. V20Gy and V16Gy were used as reference metrics for the heart and the lung, respectively.

Target coverage differences were assessed with paired T-tests and Wilcoxon signed rank tests, considering $p<0.05$ as statistically significant. In particular, when comparing 3D and 4D optimization strategies, because of the reduced sample size, the Wilcoxon signed rank test was used.

A linear regression analysis was computed to evaluate the association between the target coverage (i.e. $D_{95\%}$) degradation and the target depth in lung. The difference between $D_{95\%}$ of the reference and modulated 3D plans was plotted as a function of target depth in lung. For each patient, the average target depth in lung of the two fields (average of the two values of Table 4.*4*), was used. The analysis was computed for the "Gaussian Pmod" and the "Extreme Pmod" case.

To investigate the interplay and lung modulation combined effect, the target coverage degradation was investigated as a function of motion amplitude, both for D4D (Pmod=0 mm) and D4D modulated ("Gaussian Pmod" and "Extreme Pmod") doses. Therefore, a linear correlation analysis was computed for the difference between 3D and D4D doses($D_{95\%}$) and the target displacement.

The superposition of interplay and modulation effects was further investigated in terms of target coverage convergence over multiple fractions. For the sub-group of eight patients with motion larger than 5 mm, D4D doses were calculated by selecting each of the 4DCT phases as the starting phase of the motion surrogate, for a total of 10 different D4D doses (see section 3.5.1 4D Doses). These doses were summed up to reproduce 20 fractions, for a total cumulative dose of 60 GyRBE. Four treatment courses were computed by randomly sampling the D4D doses from the available data, and for each fraction, the averaged values were computed. The above-described method was performed both for D4D and D4D modulated ("Extreme Pmod") doses, to evaluate the difference in plan convergence. The convergence speed is defined as the number of fractions necessary to achieve the metric plateau

(+/-1%), which ideally is above/below the minimum/maximum clinically acceptable limit for the specific metric (i.e. 95% for $D_{95\%}$).

4.2.3 Results

4.2.3.1 Isolated effect study

In the following, the simulations of the interplay and lung modulation effect in isolation are presented, to estimate their magnitude independently.

Interplay effect

P14 and P15, characterized by the maximum (11.9 mm) and minimum (1.1 mm) motion amplitude, were chosen as representative cases, and shown in Figure 4.*30*. Patient P14 showed more severe target dose degradation, quantified by $D_{95\%}$ and $V_{95\%}$ decrease of 5.6 pp and 13.9 pp, respectively, and an HI increase of 8.8 pp. Despite the small motion amplitude, patient P15 $D_{95\%}$ and $V_{95\%}$ still diminished by 2.7 pp and 3.1 pp, respectively, and HI increased by 4.9 pp.

On average, the D4D target dose decreased by 5.2±1.5 pp and 12.1±5.9 pp for $D_{95\%}$ and $V_{95\%}$, respectively, while it increased by 8.3 ±2.4 pp for HI. All these differences were highly statistically significant ($p<0.001$). Interplay dose deterioration mainly affects the target, without significant changes to OAR doses. Indeed, on average the lung V16Gy changed by 1.1±2.6 pp and the heart V20Gy changed by 0.3±0.3 pp. These differences were not statistically significant ($p>0.05$).

When the target displacement is considered alone and 4D doses are compared to the reference 3D doses, $D_{95\%}$, $V_{95\%}$, and HI varied by 1.7±1.2 pp, 1.4±2.1 pp and 0.6±1 pp, respectively. No statistical significance was found ($p>0.05$). Notably, the plan deterioration magnitude is much larger when the interplay effect is considered, which demonstrates that the planning strategy, including density replacement, was adequate.

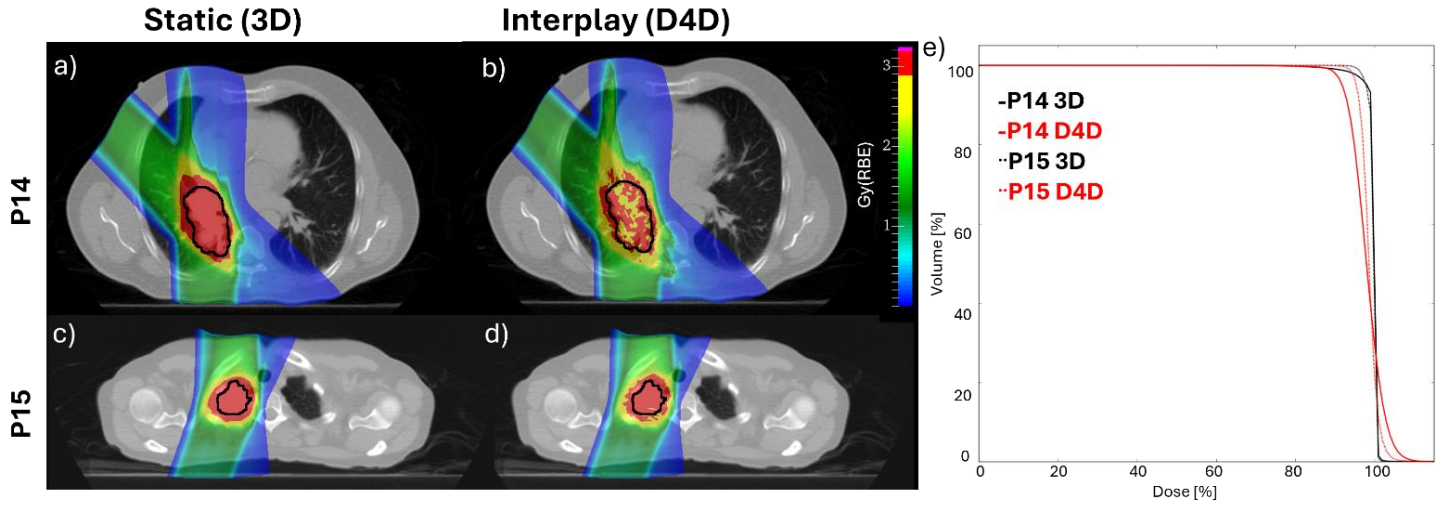

Figure 4.30 Interplay effect dose degradation. 3D (a, c) and D4D (b, d) doses for patient P14 (a, b) and P15 (c, d); the patient with the maximum and minimum target motion amplitude. DVH of static (black) and interplay (red) cases for patient P14 (solid line) and P15 (dotted line) (e). The interplay effect magnitude is larger for higher target motion but severely impacts the plan quality also for small motion. D4D= Dynamic 4D.

Lung Modulation effect

In Figure 4.*31*, the DVHs of patient P4 are shown as representative cases. The 3D dose was compared to the 3D modulated doses, both for the "Extreme Pmod" and the three "Gaussian Pmod" cases. Notably, the difference between DVH lines of the three "Gaussian Pmod" doses is not visible. The OAR metrics (V16Gy for ipsi/contra-lateral lung and V20Gy for heart) show no differences, while increased variations are visible when comparing CTV lines of the reference and modulated cases. Patient P4 3D modulated dose degradation is quantified by 2 pp, 1.2 pp decrease of $D_{95\%}$ and $V_{95\%}$ respectively, for the "Extreme Pmod" case. No changes are present for the HI metric. For the "Gaussian Pmod" cases, instead, patient P4 showed a decrease of 1.6±0.04 pp and 0.3±0.04 pp for $D_{95\%}$ and $V_{95\%}$, respectively. Patient P4 $D_{50\%}$ decreased by 2 pp and 1.7±0.05 pp, for the "Extreme Pmod" and "Gaussian Pmod" case, respectively.

The target degradation of 3D modulated doses for the "Extreme Pmod" case, calculated for the whole patient cohort, is quantified by an average statistically significant ($p<0.001$) decrease of 1.4±0.9 pp and 0.6±1.1 pp for $D_{95\%}$ and $V_{95\%}$, respectively, and non-significant difference ($p=0.06$) 0.3±0.9 pp increase for HI. The $D_{50\%}$ instead decreased on average by 1.1±0.7 pp, and the difference was statistically significant ($p<0.001$). The depth dose profile degradation caused by lung inhomogeneities, not only diminished the dose inside the target, but also shifted it in depth. However, this only affected normal tissues distal to the tumor. In fact, when the 3D modulated doses were compared to the 3D doses, no meaningful lung V16Gy and heart V20Gy changes were found.

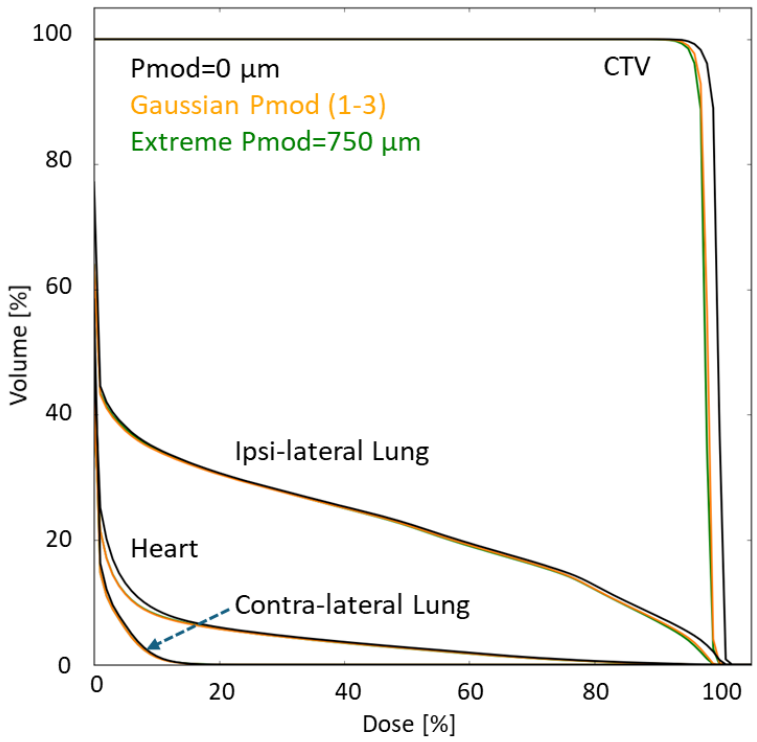

Figure 4.31 Lung modulation dose degradation. DVHs of 3D plans of patient P4 for reference (black), "Gaussian Pmod" (orange) and "Extreme Pmod" (green) cases. OARs (Heart, ipsi-/contra-lateral lung) and target (CTV) lines are plotted. Lung modulation minorly affects target coverage, while diminishing the mean target dose. Small differences are visible for different Pmod values. CTV=Clinical Target Volume, Pmod=Modulation Power

The correlation analysis between the modulation effect magnitude and the target depth in lung was performed as described in section 4.2.2 Materials and method, and results are shown in Figure 4.*32*. The linear correlation analysis showed a moderate positive correlation, quantified by a correlation coefficient R of 0.5 (p=0.03) for "Gaussian Pmod" and 0.6 (p=0.01) for "Extreme Pmod". Notably, for patients with 0 mm target depth in lung no dose degradation occurs, independently of the assigned Pmod value (see Figure 4.*37*). When the analysis was performed excluding these patients, the variable became moderately negatively correlated (R = -0.3 and R = -0.4 for "Gaussian" and "Extreme Pmod", respectively) and the correlation was no longer statistically significant (p>0.05). These results demonstrate that the (0 mm, 0%) points are significantly driving the positive correlation between $D_{95\%}$ worsening and tumor depth in lungs.

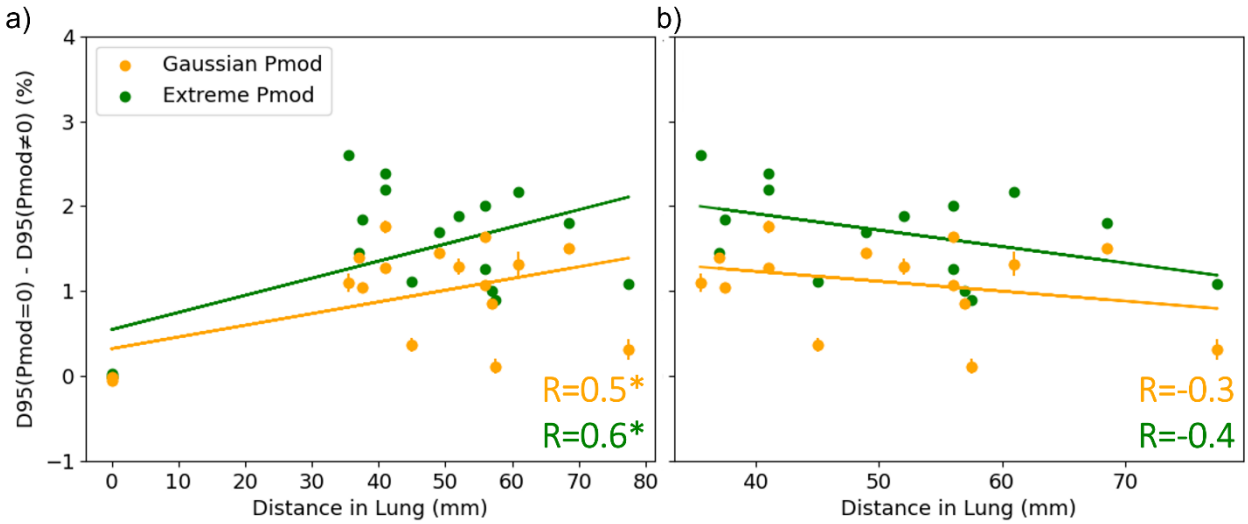

Figure 4.32 Linear correlation between $D_{95\%}$ of 3D plans (Pmod=0 mm) and 3D modulated (Pmod≠0) plans difference and target depth in lung. The correlation is computed for the "Gaussian Pmod" (orange) and "Extreme Pmod" (green). The analysis with (a) and without (b) the (0 mm, 0%) values are shown. "Gaussian Pmod" values are plotted as average (dot) and standard deviation (bar) over three values. Correlation Coefficients (R) are written, and statistical significance (p<0.05) is marked with a asterisk (*).

4.2.3.2 Combined effect

In Figure 4.*33*, 3D, D4D and D4D modulated dose distributions are displayed in axial view for patient P14. The dose broadening caused by tissue inhomogeneities smooths the dose reducing hot- and cold-spots inside the target. This is qualitatively shown by comparing Figure 4.33b and 4.33c and confirmed by the quantitative analysis. In fact, the D4D modulated dose degradation, calculated on the whole patient cohort for the "Extreme Pmod" case, is quantified by an average increase of 1.1±1.8 pp and 4.9±7.3 pp for $D_{95\%}$ and $V_{95\%}$, respectively, and 3.0±2.8 pp decrease for HI, compared to the D4D dose. The D4D modulated doses of the "Gaussian Pmod" case, showed an average increase of 0.8±1.9 pp and 3.7±7.5 pp for $D_{95\%}$ and $V_{95\%}$, and 1.9±2.9 pp decrease for HI, compared to D4D doses. These differences were all statistically significant (p<0.001), while no meaningful (p~1) lung V16Gy and heart V20Gy changes were found.

The target motion amplitude is one of the main factors, together with range changes [98], contributing to the interplay effect magnitude. Therefore, a correlation analysis was computed between the target coverage degradation and the target displacement. The linear correlation result is shown in Figure 4.*34*. Correlation coefficients of 0.7 (p=0.01) and 0.6 (p=0.04) describe the positive correlation between motion amplitude and D4D and D4D modulated ("Gaussian

Pmod") doses, respectively. When the "Extreme Pmod" is applied to interplay doses, the correlation coefficient decreases to 0.4 (p=0.07). Therefore, the target displacement has a diminished influence on dose degradation when also considering the lung modulation effect, and the influence further decreases for larger modulation values.

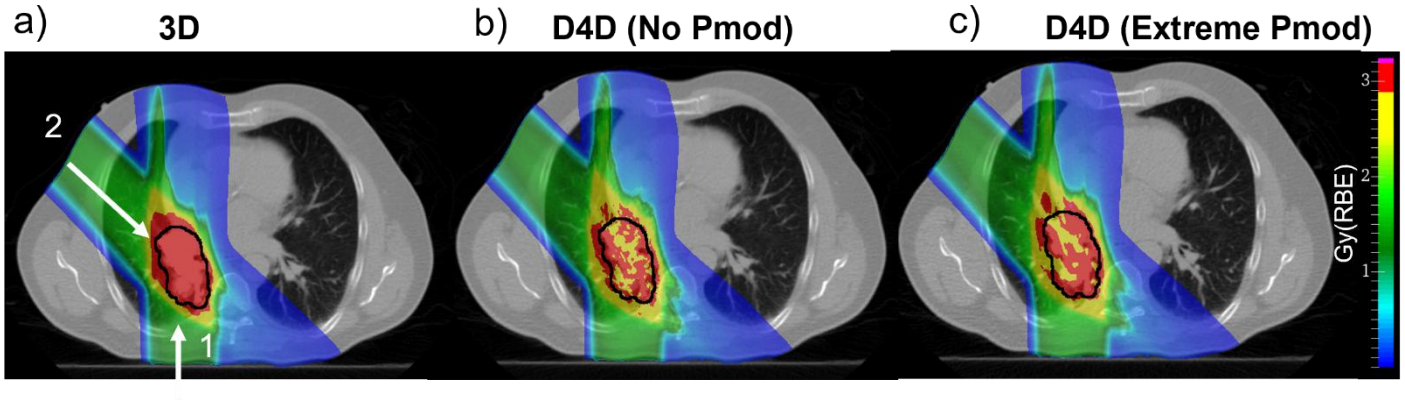

Figure 4.33 Interplay and lung modulation combined effect. 3D (a), D4D (b) and D4D modulated ("Extreme Pmod") (c) dose distributions of patient P14. The combination of lung modulation and interplay effect partially recovers interplay dose distortions. D4D=Dynamic 4D, Pmod=Modulation Power.

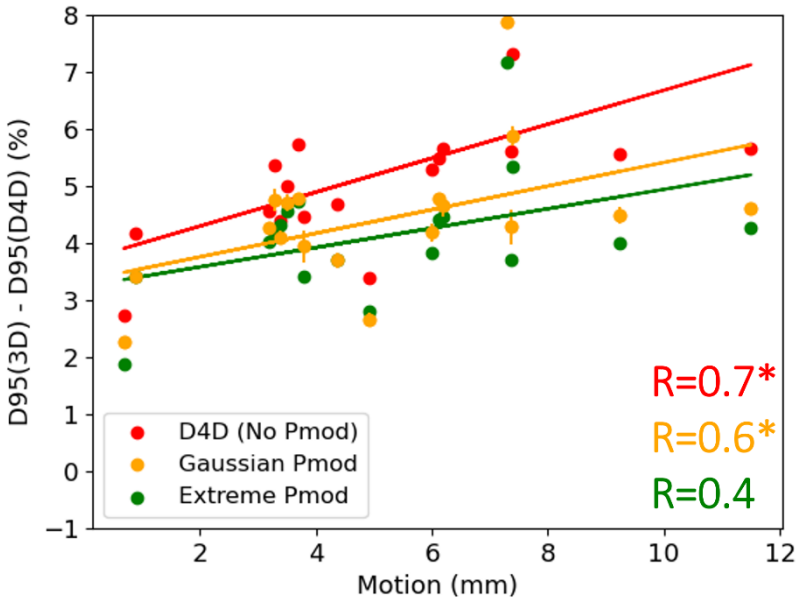

Figure 4.34 Linear correlation between the $D_{95\%}$ difference of 3D and D4D doses and target motion amplitude. The analysis was computed for D4D (red) and D4D modulated doses of the "Gaussian Pmod" (orange) and "Extreme Pmod" (green) case. "Gaussian Pmod" values are plotted as average (dot) and standard deviation (bar) over three values. Correlation coefficients (R) are given, and statistical significance is marked with an asterisk (*).

In Figure 4.*35* the target coverage convergence over 20 fractions is displayed in terms of $D_{95\%}$, $V_{95\%}$ and HI metrics, both for D4D and D4D modulated ("Extreme Pmod") doses. For every fraction, the average and the standard deviation of the four treatment courses for the eight patients are plotted. The lung modulation contribution, reducing hot- and cold-spots inside the target, positively affects the target coverage at the beginning of the treatment. After half of the treatment (~10th fraction) the interplay is averaged out, and the lung modulation remains as a small and systematic negative effect. The HI of the D4D modulated dose is consistently lower throughout the whole treatment

course. For both cases, the cumulative dose of the target converges to the final value after the first ten fractions. Notably, the inter-patient variability was large and no statistically significant difference ($p>0.05$) was found between the D4D and D4D modulated doses.

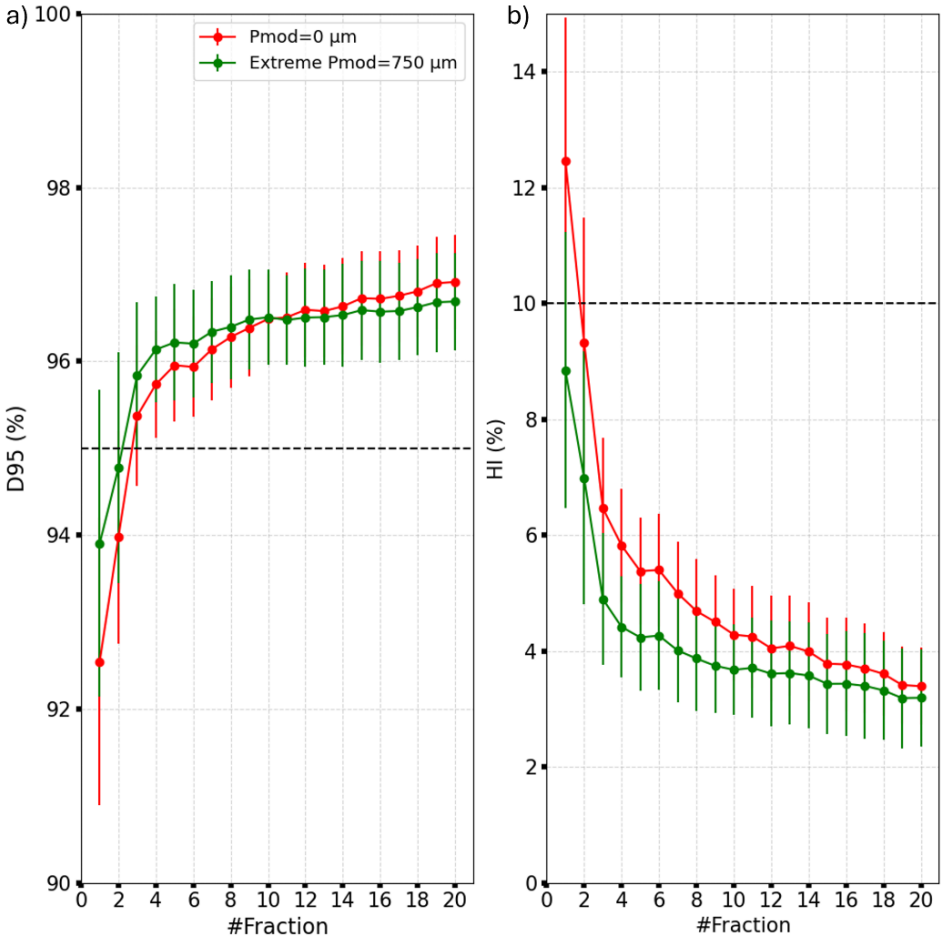

Figure 4.35 Target D4D dose convergence over 20 fractions for the patients with motion larger than 5 mm. D4D (red) and D4D modulated doses of the "Extreme Pmod" (green) case were compared in terms of $D_{95\%}$ (a) and HI (b). For each fraction the average (dot) and standard deviation (bar) are plotted for the four treatment courses simulated for the eight patients. The minimum/maximum acceptable values of 95% and 10% are marked with dashed lines for $D_{95\%}$ and HI, respectively.

Motion compensation for large target motion amplitudes

For patients with motion amplitudes greater than 5 mm, 4D optimized plans, 4D and D4D doses were computed with and without considering the lung modulation effect. In Figure 4.*36*, interplay doses computed from 3D and 4D optimized plans are shown for patient P14.

The D4D doses of the sub-group of eight patients, because of the application of the 4D optimization method, exhibit an average difference of 0.3±2.6 pp, 3.7±8.6 pp and 1.2±0.8 pp for $D_{95\%}$, $V_{95\%}$ and $D_{50\%}$, respectively, and 2±3.2 pp for HI. $D_{50\%}$ is the only metric for which the difference was statistically significant ($p<0.05$).
When comparing 3D- and 4D-optimization in terms of D4D modulated doses of the "Extreme Pmod" case, an average difference of 0.3±2.6 pp, 2.1±7.9 pp and 1.2±0.8 pp occurs for $D_{95\%}$, $V_{95\%}$ and $D_{50\%}$, respectively, while HI

changed by 1.1±2.8 pp. Only the HI and $D_{50\%}$ differences were statistically significant with p=0.008 and p=0.03, respectively.

In addition, when 3D- and 4D-optimization plans were compared in terms of 4D doses, an average difference of 0.7±2.8 pp, 0.5±3.7 pp, 0.5±1.3 pp and 0.4±2.6 pp occurred for $D_{95\%}$, $V_{95\%}$, $D_{50\%}$ and HI. None of these differences was statistically significant (p>0.05), and a large inter-patient variability was found when comparing 3D- and 4D-optimization strategies.

However, the effect of lung modulation in reducing interplay degradations was still visible for 4D optimized plans. Quantitatively, an increase of 1.6±2.9 pp, 4.8±7.6 pp occurred for $D_{95\%}$ and $V_{95\%}$, respectively, while HI showed a decrease of 4.6±3.2 pp. These differences were statistically significant with a p-value of 0.004 for $D_{95\%}$ and $V_{95\%}$ and 0.008 for HI.

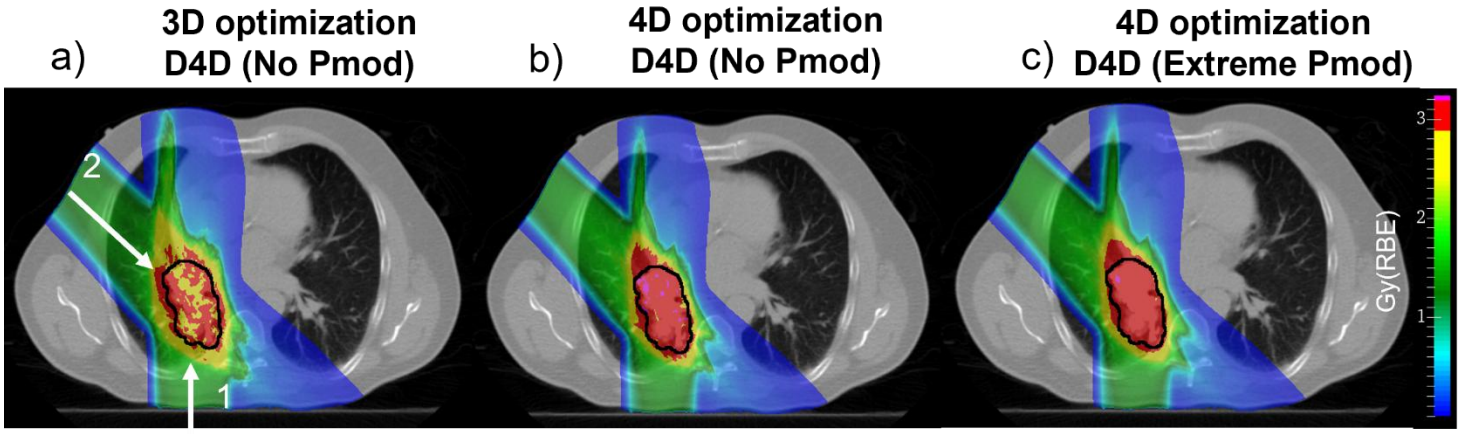

Figure 4.36 D4D dose distributions of patient P14 compared after 3D- (a) and 4D-optimization (b). Then, the D4D and D4D modulated doses are compared for the 4D-optimization method (b,c). Field directions are shown with white arrows. The IGTV is shown in black. D4D= Dynamic 4D, Pmod=Modulation Power.

4.2.3.3 Results overview

Figure 4.37 shows an overview of the results. In each row the previously described studies are displayed in terms of the target metrics $D_{95\%}$, $D_{50\%}$ and HI:

- Isolated interplay effect (4.37a): 3D doses compared to D4D doses, without including the lung modulation effect (Pmod=0 μm).

- Isolated lung modulation effect (4.37b): 3D doses without Pmod compared to "Gaussian" and "Extreme Pmod" static doses.

- Combined interplay and lung modulation effect (4.37c): D4D doses without Pmod compared to "Gaussian" and "Extreme Pmod" interplay doses.

- Isolated interplay effect in 4D-optimized plans (4.37d): D4D doses after 3D optimization compared to D4D doses after 4D optimization.

- Combined interplay and lung modulation effect in 4D-optimized plans (4.37e): D4D doses without Pmod compared to the "Extreme Pmod" D4D doses, after 4D optimization.

For each comparison, patient-specific metrics are plotted together with boxplots representing the difference distributions. The representation of the difference between the two cases in each row of Figure 4.*37* highlights the main findings of this work. Particularly, the interplay is responsible for a large and statistically significant ($p<10^{-10}$) plan quality worsening. A significant ($p<10^{-5}$) difference was also found for $D_{95\%}$ and $V_{95\%}$ of the 3D modulated doses, compared to the 3D doses. When the combined effect is investigated, the difference between D4D and D4D modulated doses was significant both for 3D-optimized ($p<10^{-5}$) and 4D-optimized ($p<0.05$) plans. The effect size was larger for 3D-optimized plans, which suggests that when the interplay is mitigated by the use of a 4D-optimization strategy, the positive effect of lung modulation on motion-related dose degradation decreases.

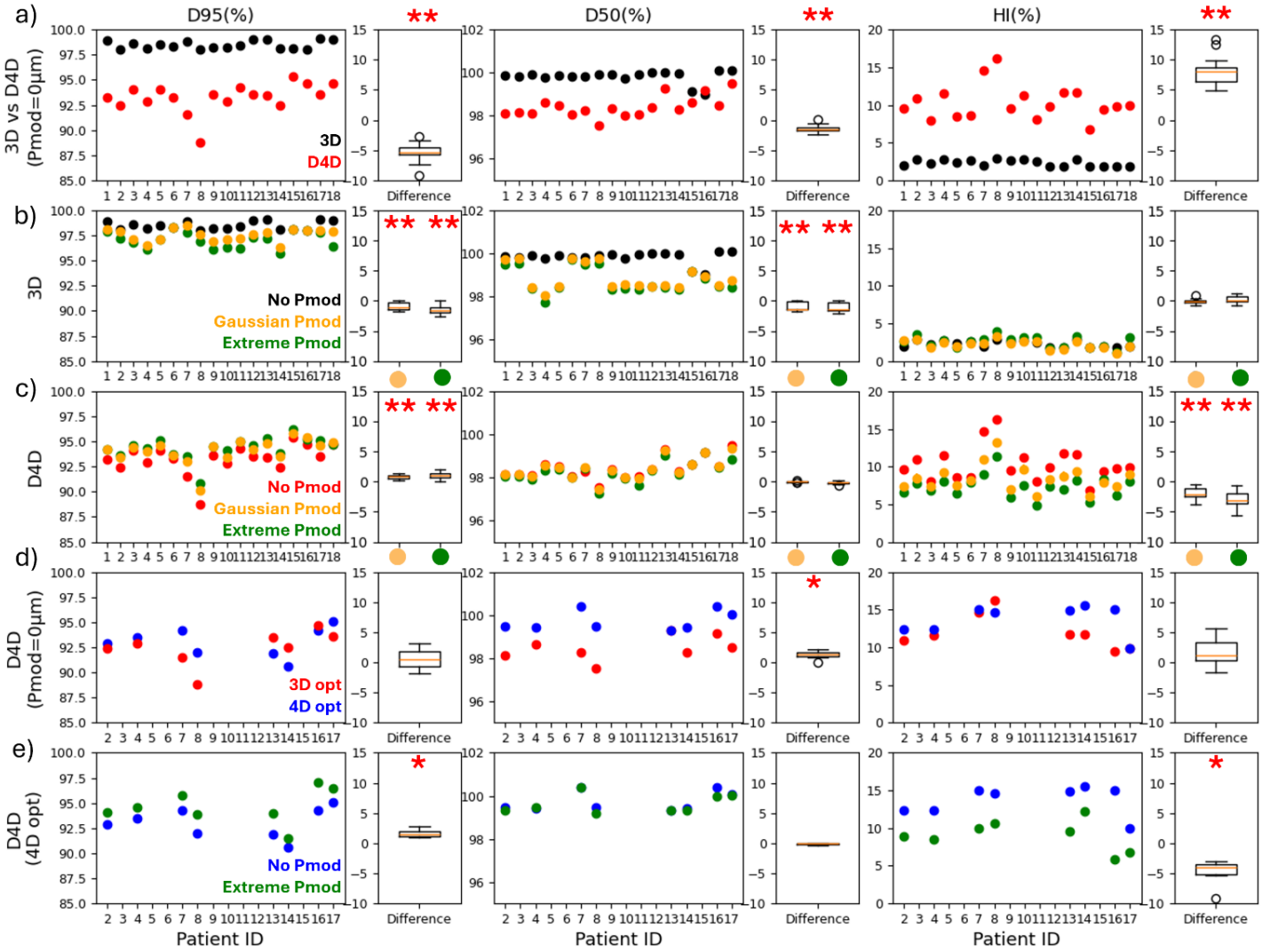

Figure 4.37 Results overview. Patient-specific $D_{95\%}$, $D_{50\%}$ and HI metrics compared for: 3D and D4D doses (a); 3D and 3D modulated doses (b), D4D and D4D modulated doses (c); D4D doses of 3D- and 4D-optimized plans (d); D4D and D4D modulated doses ("Extreme Pmod" case) of 4D-optimized plans (e). Both "Gaussian Pmod" (orange) and "Extreme Pmod" (green) values are used in modulated dose calculations (b,c). The "Gaussian Pmod" are plotted as average (dot) and standard deviation (bar) of the three values. Metric values differences are plotted with boxplots, and statistical significance ($p<0.05$/$p<0.001$) is marked with a red asterisk (*/**). D4D=Dynamic 4D, Pmod=Modulation Power, opt=optimization.

4.2.4 Discussion

This study evaluated the clinical impact of interplay and lung modulation, both individually and in combination, using a cohort of eighteen patients available from TCIA. Effect-specific parameters were analyzed, such as Pmod value and target depth in lung for the modulation effect, and motion amplitude for the interplay effect. Additionally, by comparing unmodulated and modulated interplay doses, it could be shown that lung modulation indeed has a dampening effect on interplay, partially restoring the deteriorated dose. When considering other effects mitigating interplay, such as 4D optimization or fractionation, the mitigating effect of modulation becomes smaller and eventually persists as systematic effect.

4.2.4.1 Intra-fractional motion in lung cancer treatments

In CIRT of thoracic patients, multiple factors produce range uncertainties, such as setup errors, and tissue displacement deriving from breathing motion. The latter strongly affects the finite range of ions, especially when superimposed on the actively scanned beam motion [151]. The result is severe dose distortions mainly affecting the target with hot- and cold- spots distributed inside the volume. Jakobi et al. [152] investigated the interplay effect in forty free-breathing lung cancer patients, showing that an average absolute $V_{95\%}$ reduction of 2% and 13% occurs for patients with motion amplitude smaller and bigger than 5 mm, respectively. This is in accordance with the findings of section 4.2.3.1 Isolated effect study, where P14 and P15 are reported as maximum and minimum target displacement cases.

The direct correlation between interplay effect and motion amplitude is shown in this work and was demonstrated in multiple studies [152], [153]. Thus, motion amplitude is used as the main variable in clinical practice to decide in favor or against the application of motion mitigation strategies [123]. In particular, if the amplitude exceeds 5 mm, motion management techniques are considered clinically necessary [154]. Therefore, the same criterion was used to create the sub-group of eight patients for which the 4D-optimization technique was computed. Figure 4.37 compares 3D and 4D optimized interplay doses, showing that 4D-optimizations can mitigate the interplay effect degradation. However, inter-patient variability remains large.

The random nature of motion-induced dose degradation restores plan quality after multiple fractions [152], [155], [156]. Because of its dependence on the variable breathing starting phase, motion period and amplitude, the interplay effect is averaged out over multiple fractions of a treatment course (see Figure 4.*35*). A very similar behavior would be expected if sufficient rescanning strategies were employed [157], so that rescanning was not explicitly included in the analysis.

4.2.4.2 Lung modulation in carbon ion therapy

The effect of lung tissue heterogeneities on particle range straggling has been characterized through MC simulations as well as phantom and porcine lung tissue experiments [50], [52]. This thesis includes the largest patient population so far, though still larger studies are missing to characterize true patient variability.

The dose deposition changes, mainly causing target underdosage and broadening at the dose distal fall-off, potentially impact the plan quality of lung patients treated with CIRT. However, range errors deriving from setup and motion uncertainties have been described as a major source of dose degradation in particle therapy for thoracic tumors [158]. In contrast, as shown in section 4.2.3.1 Isolated effect study, the impact of lung modulation effect is responsible for minor changes of target coverage and dose to the OARs. Baumann et al. [149] retrospectively investigated proton plan degradation of five lung cancer patients, reporting a $D_{95\%}$ decrease of at most 5% when an extreme Pmod value

of 800 μm was applied in MC dose calculations. In addition, they investigated the maximum range uncertainty of modulated cases when single field or multiple fields plan were optimized. With an increasing number of fields, the range uncertainty decreased. Winter et al. [146] in a retrospective proton therapy study investigated the lung modulation effect in ten patients, applying Pmod values of 256 μm and 450 μm as realistic and extreme cases, respectively. The "Extreme Pmod" in this study replicates the value used in their work. They found a $D_{95\%}$ worsening in the order of 0.8% for centrally located targets and 1.6% for deep seated tumors. The magnitude of the modulation effect is in accordance with the average $D_{95\%}$ decrease of 1.4±0.9 pp found when applying "Extreme Pmod" value to 3D doses. Winter et al. [146] also observed a $D_{50\%}$ decrease as a demonstration of target underdosage, as also found here.

Ringbaek et al. [128] first implemented a routine for the computation of modulated doses in TRiP98, using a continuous Poisson-based randomization process to iteratively replace lung voxel HU values with modified values. They tested it both for proton and carbon plans, after physical dose optimization. They computed dose calculations both for spherical geometries and for two patient CTs. The spherical geometries study confirmed what was also found by Flatten et al. [145] in their proton phantom study, namely the correlation between the tumor depth in lung and the lung modulation effect magnitude. However, Ringbaek and colleagues also found that these dependencies were not confirmed for the patient cases, because of the increased complexity of a real patient scenario. This is in accordance with what was found in this study and in particular the correlation analysis performed in this work. A significant positive correlation between target dose degradation and tumor depth in lung (see Figure 4.*32*) was not found. Figure 4.*37*b shows that for patients P5, P15 and P16, characterized by both fields traversing no lung tissue, the metrics of 3D doses and 3D modulated doses are the same, independent of the Pmod value. These patients guided the positive correlation between target coverage degradation and tumor depth in lung, and if excluded, the correlation became non-significant. Therefore, the tumor depth in lung is not a dominant parameter, and it needs to be considered in combination with other factors.

Paz et al. [54] showed a treatment planning case study for which the lung modulation effect was included in RBE-weighted dose calculation of one patient case. The plan was designed to maximize the beam path in lung and resulted in a $D_{95\%}$ decrease of 1.5% and 3.2% for Pmod values of 256 μm and 450 μm, respectively. The dependency of lung modulation dose degradation and on tumor depth in lung, and its effect on the mean dose $D_{50\%}$ was also confirmed in the CT-based lung tumor phantom study of Flatten et al. [145]. Notably, in a real clinical scenario, the typical plans would strive to minimize the beam path in lung tissue simply to reduce lung dose. It should also be noted that large airway structures, responsible for increased dose degradation, are resolved in the clinical CT and accounted for in the treatment plans.

4.2.4.3 Combined motion and lung modulation effects

For a comprehensive analysis of a real clinical scenario, the combination of interplay and lung modulation effect has to be considered. For this purpose, this work investigated for the first time the superposition of both effects and its impact on the RBE-weighted dose as it would occur in the patient.

Our results demonstrate that the dose smearing and broadening caused by the tissue inhomogeneities, which so far were considered as a purely negative effect, partially compensated for target underdoses and overdoses caused by the interplay effect. This was shown through $D_{95\%}$ and $V_{95\%}$ improvement of about 1 pp and 5 pp on average in the patient cohort of this study. While still, for twelve of the eighteen patients, $D_{95\%}$ and $V_{95\%}$ remained below the minimum acceptable threshold of 95% without any other motion compensation, the combination of interplay and modulation effect was always a net positive. The results also demonstrated a diminished correlation between target coverage

($D_{95\%}$) and motion amplitude when the lung modulation was applied to the interplay doses. For the "Extreme Pmod" case the correlation coefficient decreased below 0.5 and was no longer statistically significant (see Figure 4.34). While this result may seem surprising at first, it is not entirely unexpected. The interplay effect is greater for sharper beams than for broader ones, due to the higher localized dose deposition [159]. Notably, the modulation strength of heterogeneous materials has been proposed by Ringbaek et al. [50] as a ripple filter substitute in particle therapy. The results of this study confirm that the porous structure of lung tissue acts as an additional dose modulator on carbon ion dose deposition.
Finally, to embed these results in the context of a realistic treatment course, the cumulative dose over twenty fractions was simulated both for the reference D4D dose and the modulated D4D doses. The result showed that the above-mentioned plan improvement caused by the superposition of the two effects is prominent at the beginning of the treatment but fades rapidly over the following fractions. In particular, for the $V_{95\%}$ metric, the unmodulated plan at the last fraction is superior ($p<0.001$) to the modulated plan.

This demonstrates that with the averaging of interplay over multiple fractions, the motion degradation diminishes while the small degradation caused by lung modulation, with its systematic nature, persists. Indeed, the effect of tissue heterogeneities on target underdosage occurs systematically at every fraction and is not compensated for over multiple deliveries as is the random interplay effect. This can be observed in Figure 4.*35*, where fractions restore the motion-induced loss of coverage, but both $D_{95\%}$ and HI show a persistent reduction for the "Extreme Pmod" calculation. It would be interesting to analyze this also in the context of anatomical variations and fraction-wise varying modulation power. However, the fluctuation of Pmod over multiple fractions has not yet been reported, and hence, this was beyond the scope of the present work. It should also be noted that while the beam also traverses different lung regions under the influence of motion, the resulting modulation from the large number of microscopic structures involved should remain unchanged. There is no reason to assume that a repeated delivery through slightly varying lung tissue will result in a reduced modulation, the effect is indeed systematic and should not be mitigated by averaging.

The presented findings suggest that with a better mitigation of the interplay effect, for example with advanced mitigation strategies, lung modulation degradations might require additional attention, as a small but systematic effect. Among the motion mitigation methods, 4D-optimization strategies, including breathing motion scenarios at the planning stage, have been proposed [122]. As stated above, other strategies exploiting the random nature of interplay such as rescanning, will likely result in a very similar effect as fractionation and were not explicitly studied.

4.2.4.4 Study limitations

Firstly, to reproduce the modulation effect in dose calculations, a constant Pmod value is assigned to each CT voxel. This only approximates the lung tissue modulating strength that varies with different diameters of airway components. A patient-specific modulation map could assign to each lung structure a different Pmod value. For example, Flatten et al [53] proposed a method to extract patient specific Pmod directly from the HU histogram of clinical CT. In this work, this limitation was mitigated with the use of a "Gaussian Pmod" concept. For each patient three modulated doses were computed, randomly extracting the Pmod value from a normal distribution. The average result over these repetitions was then used for the analysis.

Secondly, the same motion pattern surrogate was used for interplay dose calculations, while ideally a patient-specific motion pattern could be recorded. However, to properly simulate irregular motion, image series, such as synthetic CTs from 4DMRI, or at least repeated 4DCTs would be required, which were not available for the patient cohort [160]. While it is known that the interplay pattern shows strong variability over starting phases, periods, and delivery

patterns, this is accounted for in the large number of patients as well as the fractionation study, which shows no outliers beyond those captured in the data.

Ultimately, the study is limited by the moderate number of patients, but their characteristics are distributed broadly enough to account for multiple variables and derive conclusive results, while also being the largest population investigated for the lung modulation effect to date.

4.2.5 Conclusions

This study investigated CIRT in eighteen lung cancer patients and analyzed the main factors contributing to plan degradation. The effects of interplay and tissue heterogeneity were separately assessed, and it was found that motion-induced uncertainties have a much greater impact on plan quality. However, the modulation occurs consistently at every fraction, and its relative importance increases with the improved motion control offered by modern mitigation strategies. It was also observed that the modulation of carbon ion BP caused by lung tissue spreads the dose within the target, partially compensating for the under- and over-dosage produced by the interplay effect. Due to its stochastic nature, interplay degradation becomes negligible after multiple fractions, meaning that the combined effect ultimately cancels out. Therefore, the positive effect of lung modulation on interplay would become relevant in hypo-fractionated treatments. Notably, the target coverage of the modulated interplay dose, at the last fraction, was a few percentage points lower than the unmodulated values, and the difference was not clinically relevant.

These results increase the understanding of the clinical impact of lung modulation, and its interaction with motion-related dose uncertainties, which is crucial for making CIRT a standard of care in lung cancer radiotherapy. This work indicates a small negative clinical impact of lung modulation, especially when compared to motion-related dose degradation. In addition, the use of target margin strategies in clinical practice makes the dose distribution robust against such small dose degradations (see section 3.2 Volumes of interest).

The treatment plans of this study were optimized, assuming a full beam angle flexibility of 360 degrees around the patient, would only be available with a gantry in supine position. However, currently, only 4 of the 17 CIRT facilities have a gantry. This implies that lung treatments are mostly delivered with fixed beam lines, usually from a single constant horizontal angle. Treatment options are highly limited by the lack of extended beam angle flexibility, with which superior target dose conformity and normal tissue sparing can be achieved.
Emerging gantry-less treatment modalities, such as upright therapy, that shifts the rotation from the beam delivery to the patient positioning system, have the great potential to provide maximum beam angle flexibility without the need for a gantry.
In the next chapter, the clinical impact of upright therapy and its comparison with supine therapy are presented.

5 Upright and supine carbon therapy of lung cancer: a 4D dosimetric comparison

A version of this chapter has been published in Medical Physics as Maria Chiara Martire et al. "Upright and supine particle therapy of lung cancer: a 4D dosimetric comparison" (March 2026) [161].

5.1 Introduction

The motivations behind the development of gantry-less CIRT based on upright systems were described in section 2.4. Together with economic and technological benefits, the possible clinical advantages for thoracic patients were previously introduced (see section 2.4.2 Upright radiotherapy).
The clinical outcome of upright treatments has to be comparable to that of supine therapy to permit its implementation in clinical practice. For this purpose, treatment planning studies directly comparing paired plans are required. These comparison studies are impaired by biases deriving from multiple variables that affect the robustness of the study. The treatment plan quality strongly depends on: patient image and contour quality, beam angle choice and availability, setup uncertainties as well as internal motion amplitude. Notably, all these factors may undergo substantial changes when the patient moves from the supine to the upright position.

A significant change in the body anatomy is the main consequence of a different body posture, as it emerges when comparing paired images of the same patient [78], [79], [84]. Anatomical variations might be a challenge for radiation oncologists trained and used to work with supine images. In addition, if paired CTs are acquired for the same patient, the VOI quality might also depend on the position chosen for the treatment. Furthermore, the limited availability of upright functional imaging (MRI/PET) does not allow for an accurate delineation of the target that usually only relies on CT images [61], [86]. The enormous amount of available clinical images in supine position, for different body sites and scanner types, has also enabled the development of auto-segmentation deep learning tools [162].
Together with patient imaging and contour delineation, each aspect of the treatment planning process has been standardized over the last decades for supine patient position. The definition of robustness margins is based on setup uncertainties derived from supine therapy population studies [118]. Similarly, inter- and intra-fractional motion uncertainties, investigated in supine posture, were the basis for the development of multiple motion mitigation strategies [123], [163], [164], [165]. For thoracic patients, the interplay effect is considered the major cause of dose degradation, therefore it is fundamental to assess its impact in upright therapy both for single deliveries and over the entire treatment course [16], [17], [151].
Moreover, the beam angle choice follows general rules that depend not only on the tumor site and patient-specific characteristics but also on whether a gantry or a fixed beam is available. Currently, only 4 carbon gantries are available worldwide out of 17 total CIRT facilities, which strongly limits the choice of optimal field direction [60]. This represents a limiting factor, especially for thoracic treatment plans.
Ultimately, changes of the lung anatomy and the breathing motion pattern might also affect the magnitude of the lung modulation effect. As shown in section 2.3 Lung tissue inhomogeneities, the lung modulation directly depends on the heterogeneous microstructure of the material that particles traverse. The mathematical model defines the modulation strength of a material with the Pmod, which directly depends on the material microstructure (pore) size and the density of the medium (see Equation 2.11). Matsumoto et al. [83] showed in their work that the airway changes its structure in upright position, presenting increased airway generation length and cross-sectional area. Thus,

the lung tissue might exhibit a larger modulation strength because of the lower density and the larger microstructure size.

Comparison of supine to upright therapy performed through dosimetric studies requires accounting for the role played by each of these variables. For this purpose, in this work a framework is developed to robustly compare paired 3D and 4D plans of the same patient assessing the impact of the above-mentioned factors. The framework sketch is shown in Figure 5.*38*. A DIR method was developed to register paired CTs of the same patient and propagate the target contour, to account for the impact of a different target geometry. The beam angle choice strategy is compared between postures, upright-specific field directions are investigated, and the 360 degrees angle flexibility is compared to the fixed beamlines, to reflect the actual necessity of a carbon gantry. Moreover, plan robustness is evaluated for larger robust parameters assuming that increased setup uncertainties might occur when positioning the patient in an upright position. The impact of the interplay effect on supine and upright plan degradation was also investigated through a 4D dosimetric study.

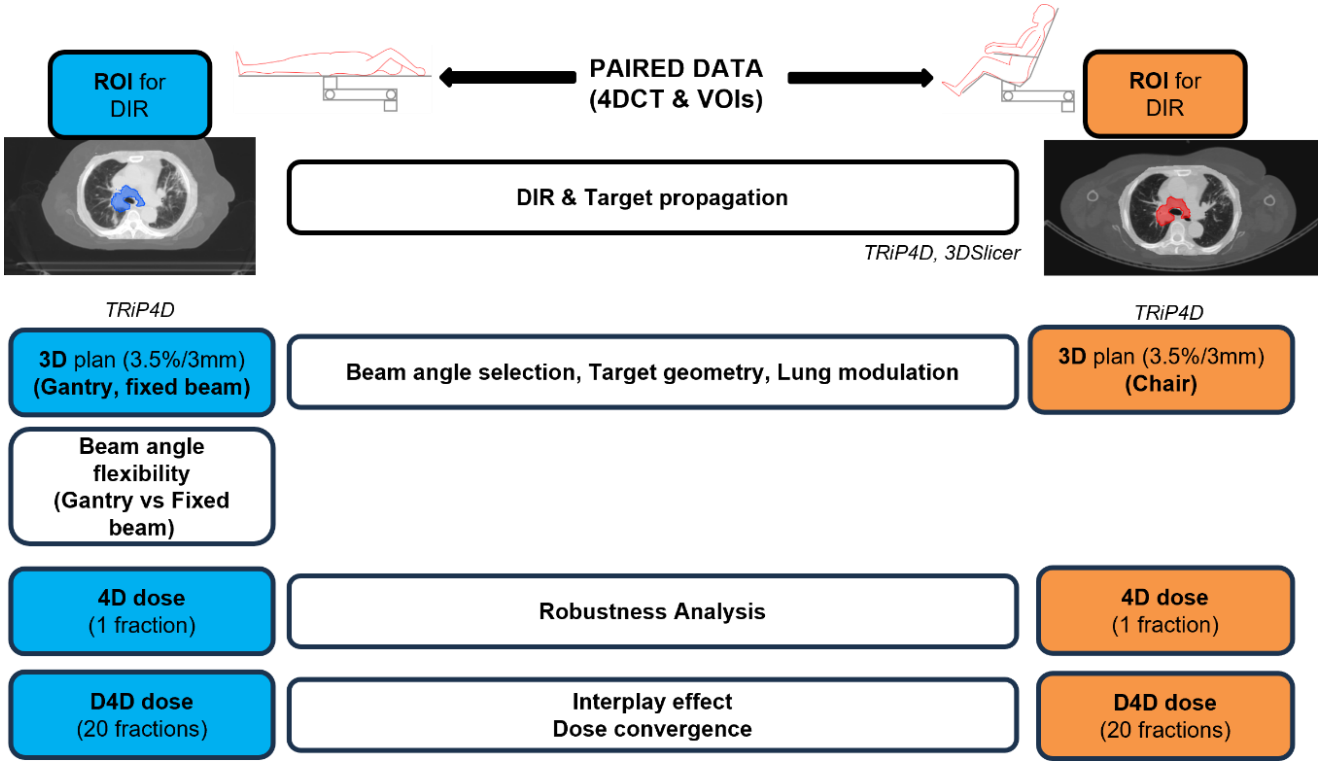

Figure 5.38 Method workflow for upright and supine image registration and treatment plan comparison. VOI=volume of interest, ROI=region of interest, DIR=deformable image registration, Opt.=optimization, D4D dose=Dynamic 4D dose/ interplay dose.

5.2 Patient data

The dataset used in this study was available from the Northwestern Medicine Proton Center (NMPC) in Warrenville, IL, USA, and includes paired 4DCT sets of six thoracic cancer patients treated under the proton collaborative group (PCG) registry. For all patients a 4DCT was acquired both in supine and upright position. In supine, patients were positioned with their arms up. In upright, patients were seated in a chair with a 20 degrees backrest incline with their arms down on an arm rest. Each supine 4DCT set is divided into individual 3DCT, each characterizing one of the 10 motion phases, each with a 650 mm field of view (FOV), 2.5 mm slice distance, 1 mm x 1mm pixel dimension. Upright images differ in having a 600 mm FOV and 3 mm slice distance.

The dataset comprises VOIs delineated by the NMPC clinical staff on both posture images. OARs and IGTV are available for each paired 4DCT, except for patient P2 and patient P4 for which the IGTV was only present on the upright and supine volume, respectively.
In Table 5.*5*, patient characteristics of interest are listed and compared between postures.
Target position in lung, volumes and motion amplitudes are shown. Particularly, the supine manually contoured (M.C.) target volume is compared both with the M.C. upright IGTV and the propagated one from the supine geometry. This comparison is relevant because the nominal 3D plans in upright were optimized on the propagated target geometry. The target motion amplitude was extracted from DIR of end-inhale (0% of the respiratory cycle) and end-exhale (50% of the respiratory cycle) CT. Table 5.*5* also reports lung (sum of ipsi-lateral and contra-lateral) and heart volumes delineated on upright and supine CT. No other OARs were considered in the study.
The quality of the contoured VOIs might vary depending on the chosen treatment position, therefore it is important to specify that patients P1, P3, P4 and P5 were treated in supine posture, whereas patient P2 and P6 were treated in the upright position.

Patient	Target Position	Target Volume (cc)			Target Δmotion (mm)		Lung Volume (cc)		Heart Volume (cc)	
		S (M.C.)	U (M.C.)	U (Prop.)	S	U	S	U	S	U
P1	RUL	60	65	58	2	3	2259	2360	858	782
P2	LLL	-	20	-	6	3	3921	4586	706	633
P3	Med.	381	340	364	3	2	3381	3957	497	590
P4	LUL	60	-	56	5	4	3251	3473	794	915
P5	LUL	273	244	262	2	2	2643	3163	717	842
P6	Med.	223	195	249	5	6	3251	3109	695	722

Table 5.5 Patient characteristics for the upright (U) and supine (S) position. The volumes of the target, heart and lungs are listed. Manually contoured (M.C.) upright and supine target volumes are listed, together with the propagated (Prop.) target volume to the upright CT. The target position in the lung is indicated (LLL = left lower lobe; LUL = left upper lobe; RUL = right upper lobe, Med.=mediastinum). The target motion is the average displacement between end-inhale and end-exhale phases (Δmotion).

5.3 Deformable image registration and target propagation

A different target structure can significantly affect the dosimetric comparison, both because of changing shape and geometry and because of the quality of the volume delineation.
To assess and quantify the impact of a different target volume, the upright nominal plan was optimized both on the contoured IGTV and the propagated one from the supine CT. The IGTV propagation is possible by means of the DIR that maps the supine to upright voxel transformation (see section 3.3 Image registration).

Because of the large anatomical changes occurring when a different body posture is taken, the conventional DIR method, applied to the whole CT, does not return an acceptable output. To overcome this limitation, a region of interest (ROI) was defined on the reference (end-inhale) upright and supine CT, around the rib-cage volume. The ROI was constructed to enclose the IGTV and high contrast structures, such as the ribs (high density) and the lung

tissue (low density). A number of slices, ranging from 3 to 25, was added from the superior and inferior IGTV limits, to create a minimum distance between ROI boundaries and the target volume. Paired ribcage ROIs were defined including the same anatomical regions and a similar number of slices was added in cranio-caudal (CC) direction to the upright and supine ROI. This number varies between patients, depending on the tumor position and the magnitude of anatomical changes between postures. With this method, similar paired ROIs, from which highly different anatomical regions were excluded, were defined. New upright and supine CTs were created by masking the reference image with the ROI and setting the density of external voxels to -1000 HU (air density).

Starting from the ribcage ROI, the DIR was performed in Plastimatch, from the supine to the upright volume and vice versa. The chosen DIR algorithm was based on three B-spline registration stages, with a regularization coefficient of 0.1 and the mean squared error (MSE) used as cost function metric. No RIR was performed prior to the DIR.

Registration and target propagation QA was computed. The qualitative analysis was carried out by comparing contoured and propagated IGTV shape, dimension and position in 3DSlicer. The distance between IGTV centers of mass (COM) coordinates was also calculated. The COMs were extracted in 3DSlicer, with their coordinates computed relative to the supine image origin and to the supine origin propagated to the upright CT for the contoured and propagated IGTVs, respectively. A further quantitative evaluation was performed by calculating the DSC and AHD between contoured and propagated structures inside each rib-cage ROI (see section 3.3 Image registration). In this case, because of the lack of a target ground truth, the lung VOIs were used for QA metric computation.
The QA was performed comparing the propagated lung structure both with M.C. lungs and with automatically contoured (A.C.) lung VOIs obtained with the TotalSegmentator deep learning tool [114]. The TotalSegmentator was trained on thousands of supine CTs available from multiple clinical centers and was applied here on both posture images. For this reason, the AI tool output was benchmarked against the M.C. lung structures, before its use in registration QA. The A.C. right and left lungs were compared to the M.C. ones, used as ground truth, and DSC as well as AHD were extracted both for the supine and the upright integral CT.

After DIR and target propagation, the propagated IGTV on upright CT was available for each patient, except patient P2. For all patients, except patient P4, the contoured IGTV on the upright CT was also available. With this dataset it was possible to optimize nominal treatment plans for both postures and compare them, taking into account the impact of a different target geometry.

5.4 Treatment planning

The treatment plans were computed in the GSI treatment planning system TRiP98 and its 4D architecture TRiP4D (see section 3.4 Plan optimization and 3.5 Dose calculation). Supine and upright nominal static plans were optimized to the IGTV on the reference CT for a carbon ion biological dose of 3 GyRBE/fraction. For a correct beam spot position, the density of the voxel inside the IGTV was replaced with the tumor tissue density (see section 3.4.2 4D optimization). A robust optimization for 3 mm isotropic margins and 3.5% range uncertainty was applied to all nominal plans and only coplanar beams were used, following the beam angle choice method described in section 5.4.1 Beam angle choice. To assess the carbon ion RBE distribution, and include it in both optimization and dose calculations, the LEM I was used considering a global alpha/beta ratio of 2 [30].

Biological 3D, 4D and D4D doses were calculated (see section 3.5 Dose calculation) and compared between paired plans for each patient. Particularly, 3D doses were used to assess nominal plan comparison and the effect of lung modulation, 4D doses were employed in RA and D4D doses were calculated to quantify the interplay effect both for single and multiple fractions.

Plan quality evaluation was carried out through visual analysis of the volumetric dose distribution, DVH and relative metrics for target and OARs (see section 3.6 Plan quality evaluation). Plan robustness was evaluated on the standard nine scenarios (see section 3.4.1 Robust optimization) both for the 3 mm/3.5% setup and range uncertainties and the increased 5 mm/5% robust parameters. This additional RA was performed to account for potentially increased setup errors and anatomical uncertainties in an upright versus supine position.
In this study, the target coverage was prioritized over OAR sparing because of the clinical complexity of the investigated patient cohort. The tumor position, shape and dimension prevented an optimal sparing of lung and heart tissue in most cases.

5.4.1 Beam angle choice

In clinical practice, the beam angle choice is driven by patient anatomy and standard beam directions exist for specific tumor sites. For example, vertical beams are preferred to oblique ones in central thoracic irradiations to reduce the beam path in lung tissue. Depending on the tumor position relative to the OARs and its depth in lung, PA or AP directions are more effective at sparing the heart or the spine, respectively. The NMPC clinical protocol was followed, optimizing two fields for each plan and assuming the availability of a gantry to simulate 360 degrees beam flexibility in supine position. For upright plans, the same assumption is made, simulating a full chair rotation around the vertical axis.
When multiple treatment strategies are compared for the same patient, a different beam geometry can significantly impact the result. With a beam angle analysis, it is possible to assess the field geometry impact on the comparison and eventually suggest upright-specific beam directions.

These steps were followed for each patient:

1. Optimize a nominal plan on supine CT, following general clinical standards for thoracic patients assuming 360 degrees beam flexibility.
2. Apply the same "supine" beam angles to the upright CT, assuming 360 degrees beam flexibility.
3. If a lower plan quality is obtained, re-optimize the upright plan with different beam directions to achieve comparable quality.
4. Optimize an additional supine plan assuming only vertical, horizontal and 45 degrees beam direction (fixed beam) and compare it with the nominal supine plan.

Following the first three steps, it is possible to assess the application of conventional beam choices for the supine position to the upright position and eventually evaluate better solution for this treatment modality. To exclude the impact of a different target geometry, the nominal upright plans were optimized on the IGTV propagated from the supine CT. However, for comprehensive results, the same upright nominal plans were optimized on the originally contoured IGTV. For consistency, the beam angles refer to the patient coordinate system because the room coordinate system would be different for the gantry and the chair.

The fourth step was included to evaluate the impact of a limited beam angle flexibility on plan conformity. Assuming 360 degrees beam flexibility is not representative of the current clinical reality since only 4 out of 17 CIRT facilities have a gantry. Most of the CIRT centers have only vertical, horizontal or 45-degrees inclined beamlines. In this work it was assumed that all three were available in the same treatment room reproducing the SAGA-HIMAT center in Tosu, Japan.

The beam angle choice study was performed neglecting the motion uncertainties. Starting from the obtained upright and supine nominal 3D plans, D4D doses were calculated to assess the interplay effect in both treatment positions.

5.4.2 Interplay dose analysis

To perform the interplay effect study comparison, D4D biological doses were calculated in TRiP4D. The available dataset did not include patient-specific motion trajectories, and the use of artificial motion surrogates was required. To reproduce the random nature of the interplay effect, for each patient and both positions, 20 D4D doses were simulated using two motion surrogates with 10 s and 5 s period lengths, and each of the 10 motion phases was selected as the starting phase. The breathing motion amplitude, instead, was directly extracted from each patient's 4DCT and did not depend on the chosen motion function. Interplay dose distributions were obtained from the 20 D4D doses and compared between supine and upright position. The statistical analysis was performed with T-tests between upright and supine distributions (statistical significance for $p<0.05$).
The interplay effect convergence speed over a full treatment course was evaluated by simulating 20 consecutive fractions. Four treatment courses were created by randomly extracting a D4D dose from the available 20 D4D doses and summing them up fraction by fraction for a cumulative dose of 60 GyRBE. For each fraction, average and standard deviation over the four treatment courses were calculated and the dose convergence was compared between supine and upright positions. The dose convergence was defined as the number of fractions necessary to achieve the plateau (±1%) of $D_{95\%}$ and HI metrics, that for clinically acceptable plans should be above 95% and below 5%, respectively.

5.4.3 Lung modulation dose analysis

Starting from the nominal supine and upright 3D plans, additional static doses were calculated including the modulation effect.

The calculation of the modulated dose in TRiP98 is based on the assignment of a global and constant Pmod value to all the voxels identified as lung parenchyma (see section 3.5.2 Lung modulation doses). An additional calculation method in TRiP98 uses the pore size (d) to derive the Pmod value, exploiting the relation between these quantities.

The Pmod formula (see Equation 2.11) can be rewritten as follows [52]:

$$Pmod = d(1 - v_{Lung})\frac{\rho_{Lung}}{\rho_{H_2O}} \quad (5.20)$$

where d is the pore size, v_{Lung} is the fraction of solid lung tissue per voxel, ϱ_{Lung} and ϱ_{H2O} are the densities of solid lung tissue (1.05 g/cm^3) and water (1.0 g/cm^3).

The lung modulation doses were computed by applying a Pmod of 0.750 mm ("Extreme Pmod" in section 4.2) both to the supine and upright CT. In addition, modulated doses were computed assigning a pore size of 0.99 mm to the supine CT and 1.09 mm to the upright CT. The supine d value was defined from Equation 5.20, with a Pmod of 0.750 mm and a lung tissue fraction of 0.28 [50]. The upright pore size d, instead, was derived from the supine one incremented by 10%. This increase was taken from the work of Matsumoto et al. [83], which showed that at the 6th airway generation the cross-sectional area is increased by 10% when the patient moves from the supine to the upright position. A Pmod of 0.824 mm corresponds to a pore size of 1.09 mm.

The modulated plans were compared to the unmodulated nominal plans both for the supine and the upright cases, for both lung modulation dose methods.

The dosimetric metrics of interest for the target were $D_{95\%}$, $D_{50\%}$ and HI, while the dose to the OARs was not evaluated since the modulation is not expected to affect the surrounding normal tissues (see section 4.2 Dosimetric study of lung modulation and interplay effect).

Differences were tested with paired a Wilcoxon signed-rank test, considering $p<0.05$ as statistically significant.

5.5 Results

5.5.1 Anatomical differences, DIR and target propagation

M.C. lung and heart volumes, as well as the target motion, are shown in Table 5.*5* for each patient in both positions. The upright lung VOIs of patients P1 to P5 show an average increase of 17% for the left lung and 10% for the right lung, resulting in an average increase of 13%±6.1% when both lungs are considered. Patient P6, instead, shows a 4.4% lung volume decrease in the upright position. The breathing motion amplitude is only minorly affected by the upright body position, with an average amplitude difference of 1 mm for all patients, except patient P2 for which the target displacement decreases from 6 mm to 3 mm when the patient is positioned upright.
An average heart volume increase of 6% for the upright position was also found. The lung volume changes reflect a different contour quality but also a lung capacity variation, while the heart volume only varies because of the VOI delineation quality. Nevertheless, quantifying heart volume changes is relevant to explain dosimetric metric values that highly depends on the structure dimension.
Figure 5.*39* shows TotalSegmentator output on patient P2 supine and upright reference CT to qualitatively analyze body posture and organ anatomy changes. Even though it is not possible to have a perfect slice-to-slice comparison, the organ shape and body position (arms up or down) differences are visible.

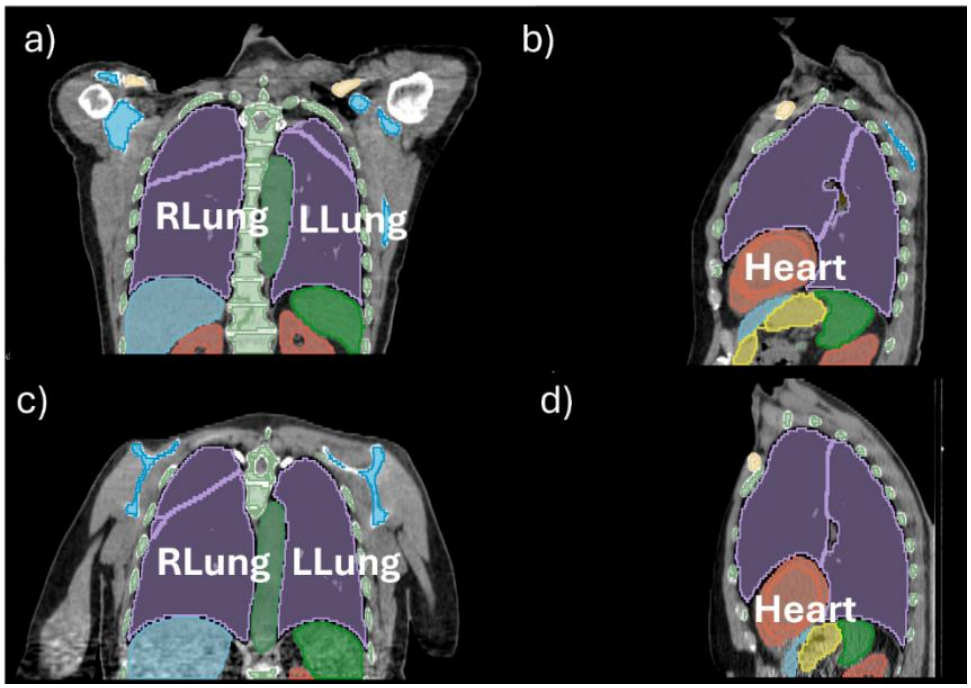

Figure 5.39 Patient P2 TotalSegmentator output on supine (a,b) and upright (c,d) reference CT, in coronal (a,c) and sagittal (b,d) view. RLung=Right Lung, LLung=Left Lung.

In Figure 5.*40* IGTV and heart M.C. structures of patient P3 are compared. The artificial cut at the superior border of the heart and at the edge between IGTV and heart are visible on the supine and upright CT, respectively. Through DIR of paired images, it is possible to propagate the IGTV, obtaining a similar target geometry on the CTs for both postures of the same patient.

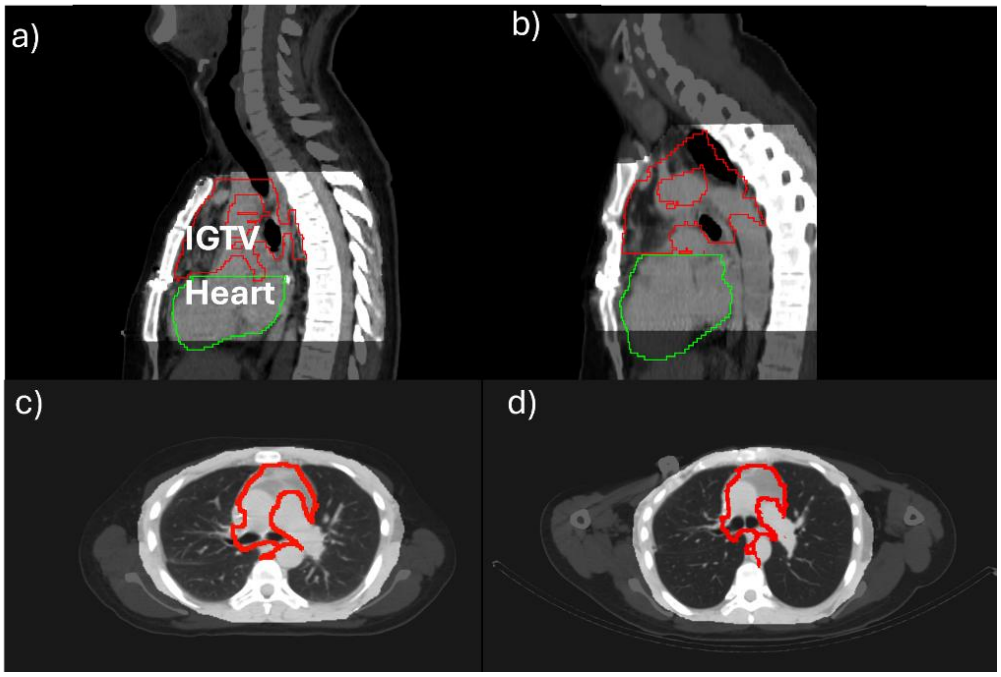

Figure 5.40 Patient P3 supine (a,c) and upright (b,d) reference CT in sagittal (a,b) and coronal (c,d) view. IGTV (red) and heart (green) contour quality differences are shown (c,d). The registration ROI is superimposed to the reference CT, together with the M.C. and propagated IGTV for the supine (c) and upright (d) case, respectively.

Since no ground truth is available for the target VOI, similarity between M.C. and propagated IGTV was assessed by comparing shape, position and volume changes. Figure 5.*41* compares 3D contoured IGTVs on supine CT and their propagated versions on upright CT.

Volumes of the upright and supine contoured and propagated IGTVs (in both directions) are listed in Table 5.*6*. The average absolute volume difference is 5.7 %±3.8 % for the six patients in both propagation directions. The maximum difference of 12.5 % was found for patient P6, when the upright IGTV is propagated on the supine image, while no volume changes occurred between the upright IGTV of patient P5 propagated to the supine CT.

The COM coordinates distance between contoured IGTV on supine CT and propagated IGTV on upright CT is shown in Table 5.*7* for all patients, except for P2. The largest difference was found for P1, while patients from P2 to P6 show COM distances of a few voxels. The differences between COM coordinates derive both from position inaccuracies and contour deformation.

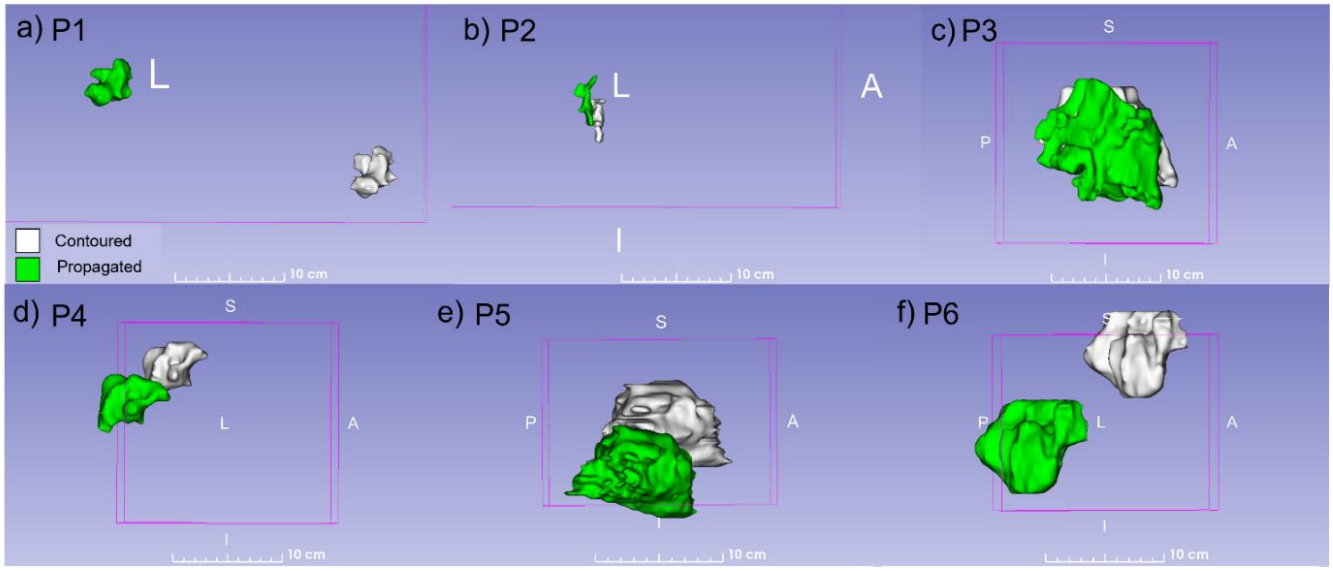

Figure 5.41 Patient P1-P6 (a-f) M.C. (white) and propagated (green) target in 3D view. Contoured supine target and the propagated one on the upright CT. For patient P2, the contoured upright and propagated supine targets are shown. S=superior, I=inferior, A=anterior, P=posterior, L=left, R=right.

Patient	Target volume (cc) (Supine→Upright)		Target volume (cc) (Upright→Supine)	
	Supine	Upright	Supine	Upright
P1	60	58	68	65
P2	-	-	21	20
P3	381	364	340	361
P4	60	56	-	-
P5	273	262	244	244
P6	223	249	223	195

Table 5.6 M.C. and propagated target volumes in both patient positions and for both propagation directions. For patients P2 and P4 the target was only contoured on the upright and supine CT, respectively.

Patient	Target ΔCOM (mm) LR, AP, IS
P1	13.8, -57, -33.1
P2	1, 5.9, -22.4
P3	-0.4, 12.1, -0.9
P4	-4.9, 1, -9.2
P5	-2.1, 8.8, -7.9
P6	1.4, -2.8, -6.7

Table 5.7 Center of Mass distance (ΔCOM) between contoured IGTV on supine CT and propagated IGTV to the upright CT. The same structures are used in supine and upright nominal 3D plans. For patient P2, the contoured upright and propagated supine IGTV are shown. Distance vector components in left-right (LR), anterior-posterior (AP), inferior-superior (IS) direction.

TotalSegmentator was used for visualization purposes (see Figure 5.*39*) and for quantitative QA of the registration and target propagation. Prior to that, the TotalSegmentator lung VOIs were benchmarked against M.C. lung structures, and the results are shown in Table 5.*8*. The AI tool QA was performed on the integral CT both for the supine and the upright CT. Average supine values of 0.95 and 1.60 mm were found for DSC and AHD, respectively. In upright, the average values of DSC and AHD are 0.96 and 1.30 mm, respectively. These results prove that A.C. and M.C. structures have comparable quality and can be used for DIR and target propagation QA.

TotalSegmentator QA				
Patient	Supine CT DSC	Supine CT AHD (mm)	Upright CT DSC	Upright CT AHD (mm)
P1	0.95	1.80	0.94	1.7
P2	0.95	1.60	0.96	1.30
P3	0.94	1.56	0.96	1.20
P4	0.97	0.90	1.00	0.10
P5	0.93	2.10	0.95	1.70
P6	0.95	1.60	0.94	2.00

Table 5.8 TotalSegmentator QA results. DSC and AHD are calculated between M.C. and A.C. lung VOIs on the integral supine and upright CT.

DIR and target propagation QA results are shown in Table 5.*9*. In this case, DSC and AHD were computed only inside the ribcage ROI since it represents the subvolume in which the registration was confined. Propagated lungs compared to the M.C. ones resulted in average DSC and AHD values of 0.95 and 1.5 mm, respectively. When the A.C. lungs are used as ground truth, an average DSC of 0.94 and AHD of 1.6 mm were found.

Propagation direction	Patient	M.C. vs propagated VOI		A.C. vs propagated VOI	
		DSC	AHD (mm)	DSC	AHD (mm)
Supine→Upright	P1	0.95	1.45	0.94	1.58
	P2	0.93	2.00	0.93	1.80
	P3	0.95	1.48	0.95	1.54
	P4	0.96	1.46	0.96	1.59
	P5	0.94	1.50	0.93	1.70
	P6	0.96	1.20	0.94	1.60
Upright→Supine	P1	0.93	1.50	0.92	1.75
	P2	0.96	1.52	0.94	1.60
	P3	0.96	1.36	0.95	1.75
	P4	0.95	1.42	0.97	0.84
	P5	0.92	2.00	0.94	1.80
	P6	0.96	1.24	0.94	1.60

Table 5.9 DIR and lung propagation QA. DSC and AHD values for each patient and propagation direction. DSC and AHD were calculated both by comparing the propagated lungs with the M.C. and A.C. lung VOIs. The QA was performed inside the ribcage ROI, the subvolume in which the DVFs were defined.

5.5.2 Beam angle choice

The beam angle geometry analysis was performed as described in section 5.4.1 Beam angle choice**5.4.1 Beam angle choice**. It returned the optimal supine and upright nominal 3D plans for each patient. In Table 5.*10* paired 3D plans are compared through OARs metrics, since the same target coverage ($D_{95\%}$=98%, HI=1.8% and $V_{95\%}$=100%) was achieved for each plan. The second column shows the 3D nominal plans optimized for the supine CT on the M.C. IGTV. Lung and heart metrics are below the clinically acceptable threshold, except patient P3, for which the partial superposition of target and heart volume prevented an optimal sparing of this organ (see Figure 5.*40*).
These optimal supine angles were directly applied to the upright reference CT on which the propagated IGTV was defined as target (3rd column). An increased OAR dose was found for each patient except P1, suggesting that a new angle optimization is necessary. Results of the new optimized plans (5th column) represent the upright nominal 3D plans are used as the reference throughout the study. Upright 3D nominal plans were also calculated on the M.C. IGTV (6th column).

Patient	"Supine" Angles (degrees)	Supine		Upright		"Upright" Angles (degrees)	Upright		Upright	
		Angles opt.		"Supine" angles			Angles opt.		Angles opt.	
		M.C. target		Prop. target			Prop. target		M.C. target	
		V_{16Gy} (%)	V_{20Gy} (%)	V_{16Gy} (%)	V_{20Gy} (%)		V_{16Gy} (%)	V_{20Gy} (%)	V_{16Gy} (%)	V_{20Gy} (%)
P1	90,290	10.4	0	9.9	0	90,290	9.9	0	10.4	0
P2	250,290	9.4*	5.5*	11.0*	8.6*	250,335	-	-	11.3*	7.8*
P3	90,270	23.0	15.0	23.5	18.6	90,270	23.5	18.6	20.1	7.6
P4	270,290	4.3	2.8	4.7	4.4	270,290	4.7	4.4	-	-
P5	270,135	17.3	8.4	21.9	6.0	225,135	18.2	6.8	16.9	5.7
P6	250,290	19.9	5.0	24.6	9.4	250,290	24.6	9.4	24.1	7.4

Table 5.10 Supine (2nd, 3rd columns) and upright (5th, 6th columns) 3D nominal plans. For each plan V16Gy(lung) and V20Gy(heart) are listed. In 1st to 3rd columns the angles optimized on supine ("Supine" angles) and resulting plans on supine contoured target (M.C. target) and upright propagated target (Prop. Target), are shown. In 4th to 6th columns the angles optimized on upright ("Upright" angles) and resulting plans on upright propagated target and M.C. target, are shown. *= Patient P2 supine plan optimized on propagated IGTV and upright plan optimized on contoured IGTV. Vertical AP 90 degrees, vertical PA 270 degrees, oblique AP 45 and 135 degrees, oblique PA 225 and 315 degrees. Field angles refer to the patient coordinate system and not the room system that would be different for the gantry and the chair.

For patient P2, an upright-specific angle selection (second field inclined from 20 degrees PA to 65 degrees PA) allowed a lower V20Gy(heart) to be achieved but the V16Gy(lung) remained elevated compared to the supine plan. Nevertheless, the V16Gy(lung) was still within the clinical acceptance threshold.

For patient P5, a new angle in upright permitted to reduce V16Gy(lung) to values comparable to the supine position. As shown in Figure 5.*42*, in the upright posture the lung is compressed less in the PA direction compared to the supine position. This results in a longer beam path in the lung for PA fields. Therefore, the oblique field direction allowed to reach a reduced V16Gy(lung) with respect to the vertical beam that was the optimal choice in supine. As a result, for this patient, the optimal field was inclined by 45 degrees compared to the initial PA direction to achieve reduced OAR doses.

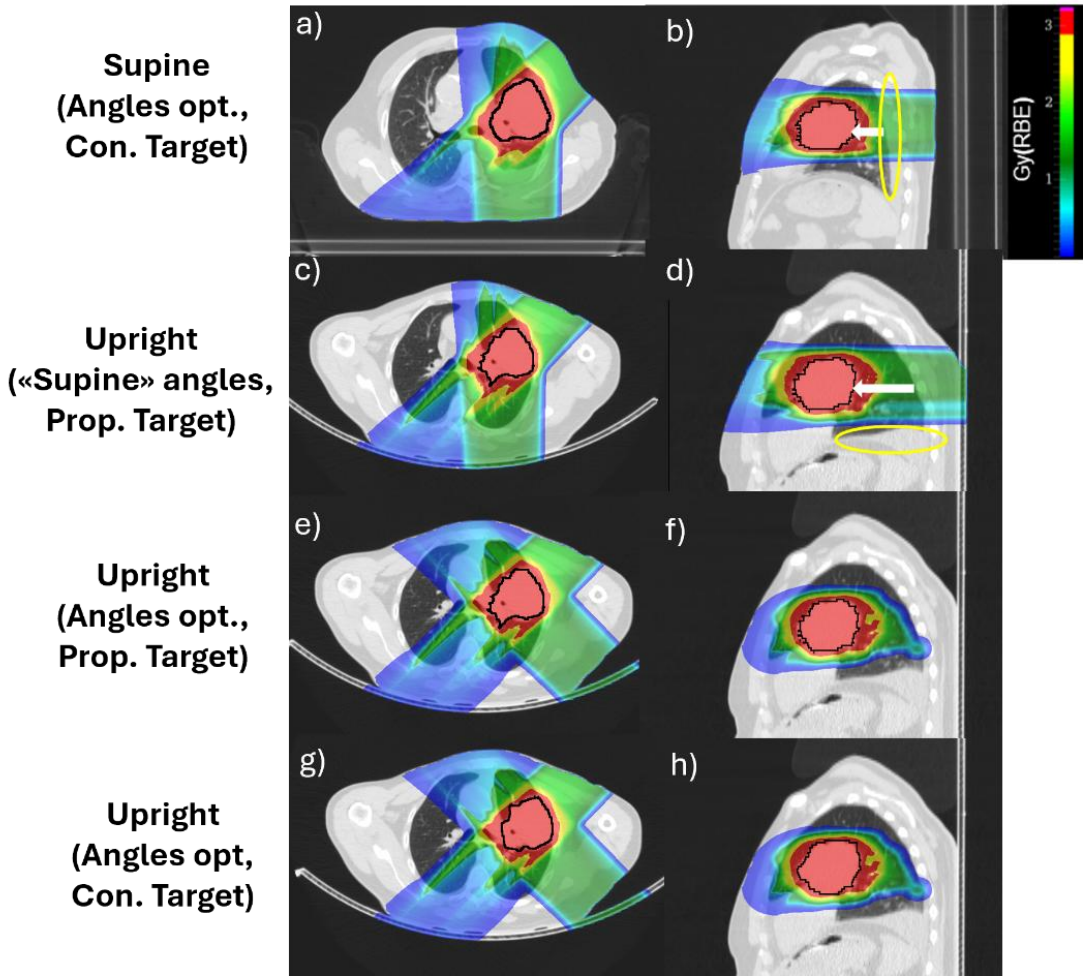

Figure 5.42 Patient P5 supine (a, b) and upright (c-h) 3D doses in axial (a, c, e, g) and sagittal (b, d, f, h) view. Supine nominal plans after beam angle optimization (Angles opt., Con. Target) (a, b). The same angles are chosen for the upright plan ("Supine" angles, prop. Target) (c, d). With a yellow line the changed position of the pleural effusion posterior (b) or inferior (d) is marked. It results in a significantly longer posterior beam path through the lung in upright position, which explains the higher V16Gy(lung), see Table 5.10. Upright plans after beam angle optimization on upright geometry, on the propagated (Angles opt., Prop. Target) (e,f) and M.C. IGTV (Angles opt., Con. Target) (g,h) are shown. The target is shown in black. Posterior lung volume changes are marked with white arrows. Opt=optimization, Prop=propagated, Con=contoured.

For P3, P4 and P6, the nominal supine angles (opposing vertical AP/PA fields for P3 and P4, and PA fields with ±20 degrees inclination from the vertical axis for P6) also resulted in the best plans for the upright posture. An increased V20Gy(heart) was found in upright for P3 and P4, as well as V20Gy(heart) and V16Gy(lung) in upright for P6, independently of the beam angle selection. For P3 this was due to the target surrounding the heart, which made

proper sparing of the heart impossible (see Figure 5.*40*). For P6 and P4, because of patient specific lung anatomy, the upright plan always resulted in higher OAR doses, independent of the beam angle configuration.
The last column of Table 5.*10* lists the upright plans optimized on the M.C. target VOI. The field directions of the upright nominal plans were used, and the dose was recalculated on the contoured IGTV. The result is a comparable plan quality with the nominal upright plans, with the only exception of patient P3 for which V16Gy(lung) and V20Gy(heart) decreased by 3 pp and 11 pp, respectively. This is explained by the relative target and heart position and the artificial cut applied to the target VOI to prevent structure overlapping. For patients P2 and P4, the comparison between propagated against contoured target geometry was not possible because the IGTV was not manually delineated in both position CTs.

The last comparison of the beam angle choice analysis was performed between 360 degrees and fixed beam plans in supine position. Table 5.*11* compares the supine nominal plans (Table 5.*10*, 2nd column), with the fixed beamline plans (field directions limited to AP/PA vertical and 45 degrees). Results indicate that for patient P1 the fixed beam angle selection did not affect the final plan quality, while for patients P2, P4 and P6 increased dose was delivered to the OARs because of the limited possible angles selection, in particular, an increase of 3 pp, 3 pp and 9 pp for V16Gy(lung) of P2, P4 and P6 was found. For patients P3 and P5, instead, the optimal 3D plan would have also been deliverable with fixed beams. When only a fixed beamline is available, the upright position offers increased benefit for these patients, compared to the gantry-based comparison. Most existing beamlines are horizontal (only 4 out of more than 50 beamlines at 17 CIRT centers are equipped with a gantry), where the plan quality would be even worse or lung treatment would be totally infeasible in supine position for most tumor locations.

Patient	Gantry angles (degrees)	Supine (Gantry)		Fixed beamline angles (degrees)	Supine (Fixed Beamline)	
		V_{16Gy} (%)	V_{20Gy} (%)		V_{16Gy} (%)	V_{20Gy} (%)
P1	90,290	10.4	0	90,270	9.7	0
P2	250,290	9.4	5.5	225,315	12.4	7.2
P3	90,270	23.0	15.0	90,270	23.0	15.0
P4	270,90	4.3	2.8	270,315	7.5	3.1
P5	270,135	17.3	8.4	135,270	17.3	8.4
P6	250,290	19.9	5.0	225, 315	28.5	5.1

Table 5.11 Supine plans optimized mimicking the full beam direction availability of the gantry (1st -2nd columns) and a fixed beamline scenario (3rd-4th columns). For patients P3 and P5 the gantry angles would have also been deliverable with a fixed beam, and the plans were not recalculated. Vertical AP 90 degrees, vertical PA 270 degrees, oblique AP 45 and 135 degrees, oblique PA 225 and 315 degrees. Field angles refer to the patient coordinate system and not the room system that would be different for the gantry and the chair.

Once the supine and upright 3D nominal plans were optimized, their robustness was assessed against standard 3 mm/3.5 % robust parameters (used in plan optimization) and more conservative 5 mm/5 %. None of the scenarios failed when the RA was computed with 3 mm/3.5% robust parameters. Figure 5.*43* shows the DVHs for the RA of supine and upright positioning performed for 5 mm/5% uncertainty parameters. Four scenarios failed to cover the target adequately. This occurs in patient P1 (1 upright), patient P2 (1 upright, 1 supine) and patient P4 (1 supine). If robust optimization had been performed with increased uncertainties, robustness would have been recovered, but at the expense of extra lung dose.

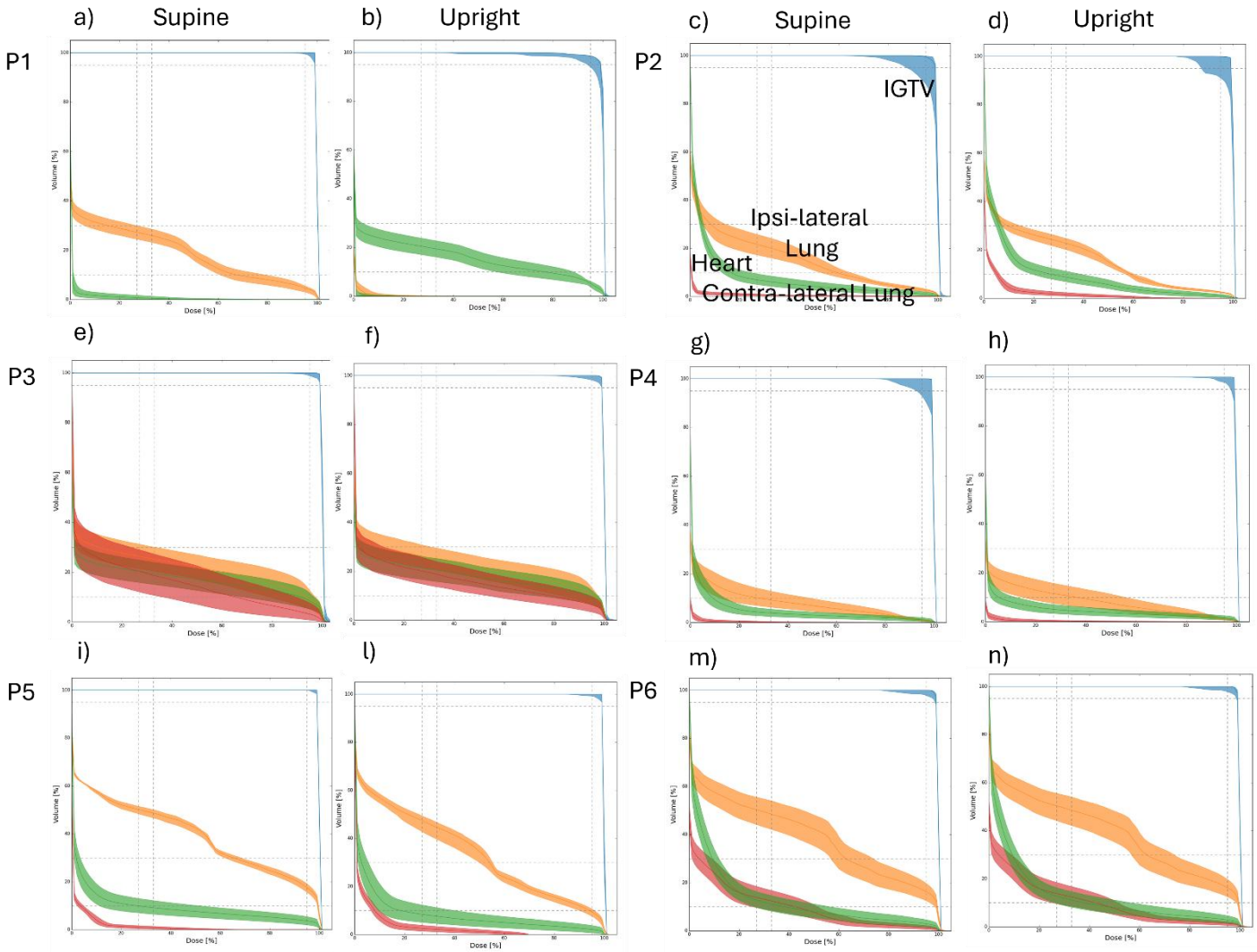

Figure 5.43 Supine (a, c, e, g, i, m) and upright (b, d, f, h, l, n) 5 mm/5% robustness analysis DVHs. Ipsi-lateral lung (orange), contra-lateral lung (red), heart (green) and IGTV (blue) nominal scenarios are plotted with solid lines, and bands illustrate the minimum-maximum range. The minimum clinically acceptable target coverage ($D_{95\%}/V_{95\%}$=95%), lung (V27%(lung)=30%) and heart (V33%(heart)=10%) dose, are marked with dashed lines. IGTV = geometrical internal target volume.

5.5.3 Interplay dose analysis

The interplay effect comparison between treatment postures was carried out as described in section 5.4.2 Interplay dose analysis. In Table 5.*12* a comprehensive result overview is provided through target and OARs metrics average and standard deviation of the 20 D4D doses, for each patient in both positions. Significant differences ($p<0.05$) were found for the target coverage of patients P1, P2, P5 and P6, but only the differences for patients P1 and P2 were clinically significant. The largest difference occurred for patient P2, and this is due to the large motion amplitude reduction in upright position. This is also visible in the boxplots of Figure 5.*44*, showing target coverage of both postures for each patient. For patients P3 to P6, because of the minor motion amplitude differences between postures, the interplay effect degradation showed no significant variation.

	Patient	Supine	Upright	Supine	Upright	Supine	Upright
		$D_{95\%}$ (%) (μ±σ)	$D_{95\%}$ (%) (μ±σ)	HI (%) (μ±σ)	HI (%) (μ±σ)	$V_{95\%}$ (%) (μ±σ)	$V_{95\%}$ (%) (μ±σ)
Target	P1	**96.1±0.2***	94.3±0.5	**7.8±0.5***	11.2±0.8	**98.2±0.5***	92.9±1.8
	P2	91.7±0.8	**94.6±0.5***	16.2±1.2	**11.0±0.7***	84.4±3.4	**93.9±1.7***
	P3	97.3±0.1	97.3±0.1	5.6±0.1	**5.5±0.1**	99.6±0.1	**99.7±0.1**
	P4	94.9±0.4	**95.0±0.5**	9.9±0.7	9.9±0.4	95.0±1.1	95.0±1.4
	P5	**97.5±0.1***	97.3±0.2	**5.0±0.2***	5.4±0.4	**99.8±0.1***	99.3±0.3
	P6	95.4±0.2	**95.7±0.2***	9.1±0.4	**8.5±0.2***	96.2±0.6	**97.2±0.5***
	P1-P6	**95.8±0.01**	95.5±0.01	**8.3±0.1**	8.9±0.2	95.5±0.2	**96.7±0.1**
		Lung				Heart	
		V_{16Gy} (%) (μ±σ)	V_{16Gy} (%) (μ±σ)	V_{16Gy} (cc) (μ±σ)	V_{16Gy} (cc) (μ±σ)	V_{20Gy} (%) (μ±σ)	V_{20Gy} (%) (μ±σ)
OARs	P1	10.8±0.03	**9.6±0.1**	245.0±0.6	**227.5±2.8**	0	0
	P2	**9.6±0.05**	11.5±0.09	**377.7±1.9**	527.4±4.1	6.0±0.06	**8.6±0.2**
	P3	**23.2±0.02**	23.7±0.02	**785.4±0.6**	938.8±0.9	**18.6±0.1**	18.8±0.06
	P4	**3.8±0.07**	4.3±0.1	**124.9±2.3**	150.3±2.5	**3.8±0.04**	4.6±0.02
	P5	**17.8±0.03**	19.5±0.06	**469.6±0.8**	618.5±1.8	9.3±0.02	**7.5±0.02**
	P6	**20.4±0.1**	25.6±0.1	**663.6±3.5**	797.1±3.8	**6.1±0.09**	11.0±0.08
	P1-P6	**14.3±0**	15.7±0	**444.4±0.2**	543.2±0.3	**7.3±0**	8.4±0

Table 5.12 Supine and upright target ($D_{95\%}$, HI, $V_{95\%}$) and OARs (V16Gy(lung), V20Gy(heart)) metrics averaged over 20 deliveries. Mean (μ) and standard deviation (σ) are listed. Better values between positions are highlighted in bold and statistically significant values ($p<0.05$) are marked with a star (*). In the last row, for both target and OARs, the average over six patients is listed.

Results of the whole patient cohort are listed in the last row of Table 5.*12* and plotted in the last column of Figure 5.*44*. No statistically significant differences ($p<0.05$) occurred between supine and upright position. Notably, V16Gy(lung) and V20Gy(heart) showed very narrow distributions around the average values. This is expected since the interplay effect mainly degrades the target dose and only minimally affects normal tissue doses. For this reason, the statistical analysis was only conducted using the upright and supine average values over the whole patient cohort. The results of the V16Gy(lung) reflect what was found for the static dose calculation, while the heart doses seem to be more heterogeneous between patients.

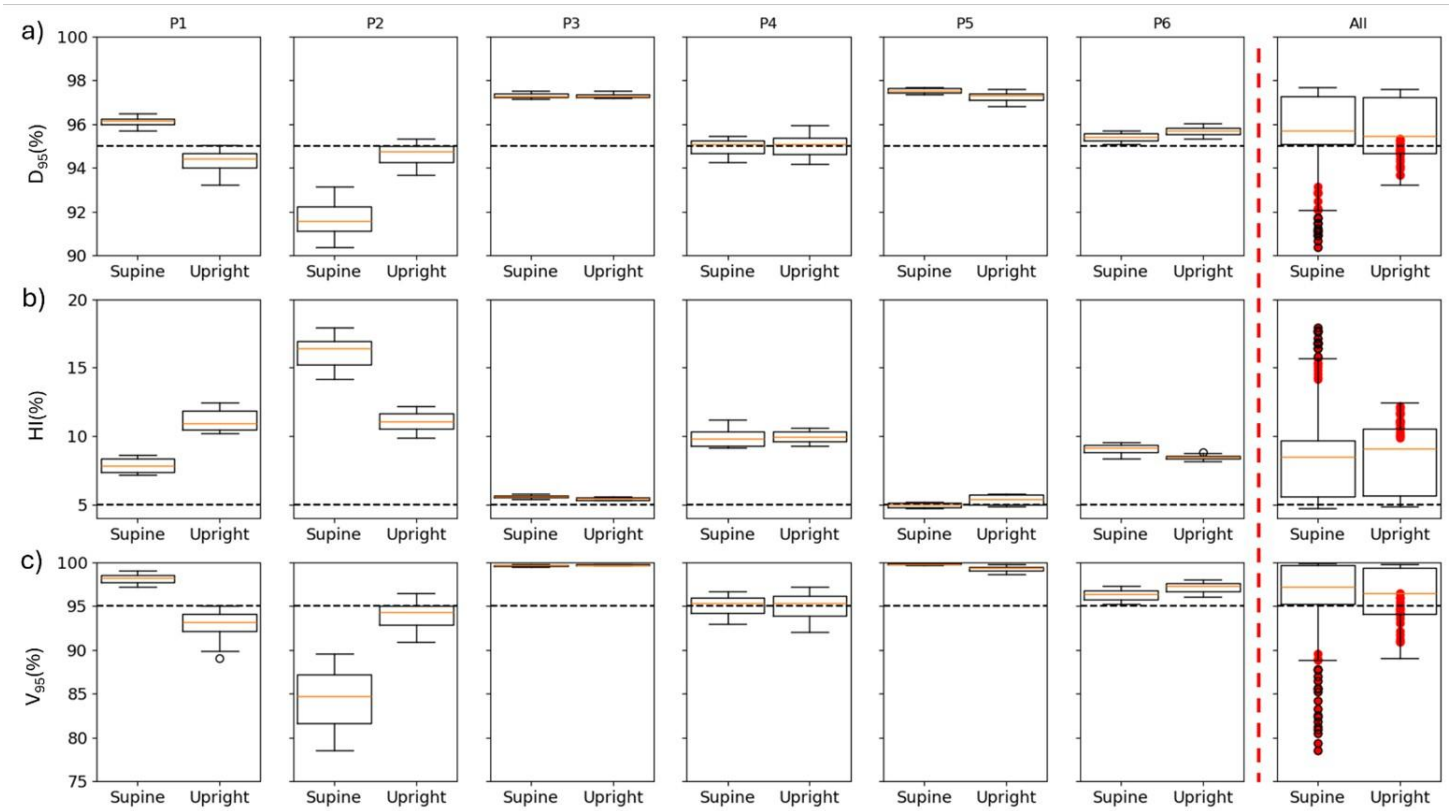

Figure 5.44 Supine and upright $D_{95\%}$, HI and $V_{95\%}$ distributions over 20 D4D dose deliveries for the IGTV. In the last column the averaged metrics distributions from the six patients are compared. Values deriving from patient P2 are plotted in red for each metric. Black dashed lines indicate the 95% and 5% threshold lines for $D_{95\%}$/$V_{95\%}$ and HI, respectively. Average and standard deviation values for each metric are listed in Table 5.12.

With the pool of 20 D4D doses, the interplay effect convergence over multiple fractions was simulated for each patient and compared between postures. Figure 5.*45* depicts $D_{95\%}$ and HI average and standard deviation, over the four simulated treatment courses, for each patient in both treatment positions. These results confirm that patients P1 and P2 show major differences between postures. For patient P1, the supine plan is superior to the upright one until the 16th fraction, where the two values almost superimpose. For patient P2, the fraction-by-fraction dose comparison shows increased plan quality in upright position. For all patients and both positions, the metric-specific threshold (95% for $D_{95\%}$ and 5% for HI) was achieved at the third fraction at the latest, and the plateau (± 1%) was reached at the 10th fraction at the latest.

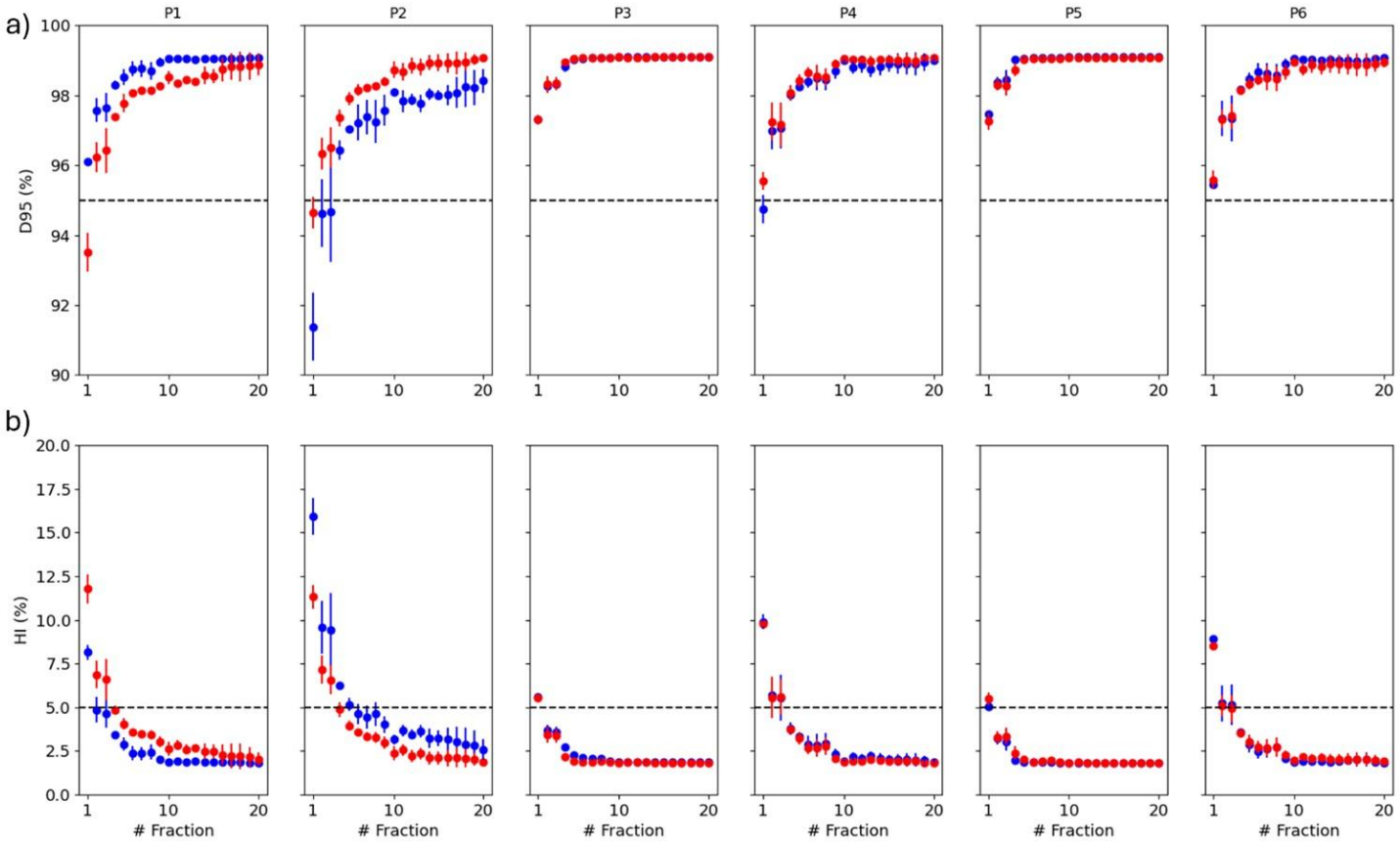

Figure 5.45 Supine and upright target coverage convergence over 20 fractions. $D_{95\%}$ and HI are shown for upright (red) and supine (blue) plans. Four fractionation treatments are simulated, and their mean (dot) and standard deviation (bars) are displayed for each fraction. The minimum clinically acceptable values of 95% and 5% are marked with dashed lines for $D_{95\%}$ and HI, respectively.

5.5.4 Lung modulation dose analysis

In Figure 5.*46*, single patient metrics are shown in each row, for one of the two treatment positions, comparing the nominal 3D plan (reference) with the modulated plan. First, the impact of the assigned Pmod (0.750 mm) is assessed for supine and upright cases, then, the modulation is obtained with the assignment of a pore size (d) value. The same comparisons are shown in Table 5.*13*.

The statistics shown in Figure 5.*46* evaluate the differences between unmodulated and modulated plans of upright and supine treatments separately. The statistical tests shown in Table 5.*13*, instead, focus on the differences between supine and upright unmodulated and modulated doses.

The results show no significant clinical impact of the modulation effect on target coverage, and no significant differences were found for the two treatment positions.

Metric	Nominal (μ±σ)		Assigned Pmod (μ±σ)		Assigned d (μ±σ)	
	Supine	Upright	Supine (Pmod = 0.750 mm)	Upright (Pmod = 0.750 mm)	Supine (d=0.99mm)	Upright (d=1.09 mm)
D_{95}(%)	99.09±0	99.09±0	99.07±0.02	99.08±0	99.07±0.02	99.08±0
D_{50}(%)	99.96±0.01	99.98±0.02	99.83±0.14	99.76±0.3*	99.82±0.14	99.89±0.08
HI	1.81±0.01	1.8±0.01	1.78±0.04	1.8±0.01	1.78±0.04	1.8±0.03

Table 5.13 Target $D_{95\%}$, $D_{50\%}$ and HI metrics of reference and modulated 3D plans, averaged over the six patients for the upright and supine case. The modulated doses are computed both by assigning the Pmod (0.750 mm) and the pore size (d) value. The supine d (0.99 mm) corresponds to a Pmod of 0.750 mm, the upright d (1.09 mm) is equivalent to a Pmod of 0.824 mm. μ=mean, σ=standard deviation, Pmod= Modulation Power, d =pore size. Statistical significance ($p<0.05$) is marked with a star (*).

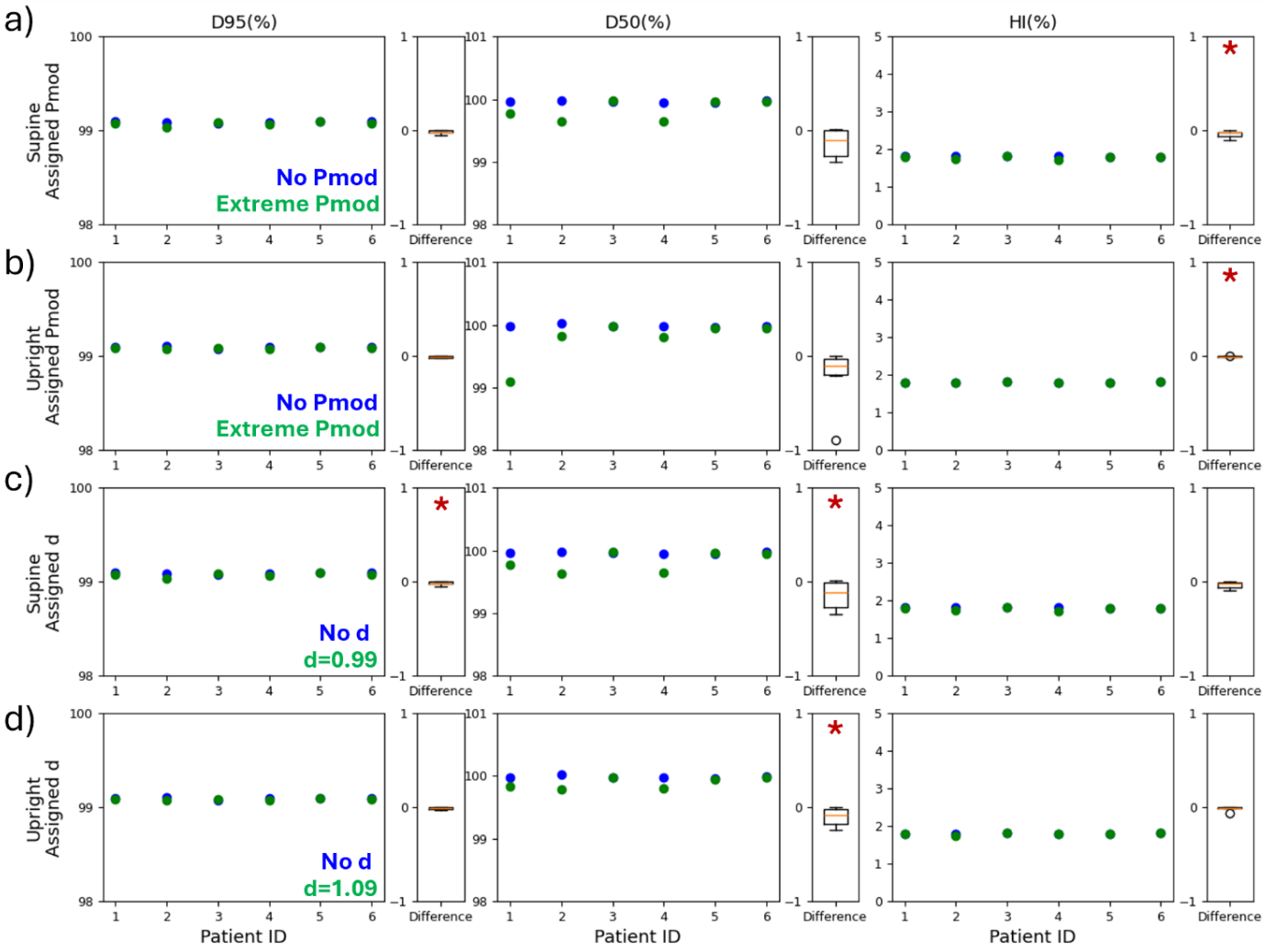

Figure 5.46 Patient-specific $D_{95\%}$, $D_{50\%}$ and HI compared for supine (a,c) and upright (b,d). Dose calculation method based on assigned Pmod ("Extreme Pmod", 0.750 mm) (a,b) and pore size (c,d) are shown. Metric values differences between the reference case (blue) and the comparison case (green) are plotted with boxplots. Statistical significance ($p<0.05$) is marked with a red star (*). Pmod=Modulation Power, d = pore size.

5.6 Discussion

We developed a framework to assess the impact of upright patient positioning on carbon ion therapy for thoracic patients, by comparing plans generated for upright and supine therapy in different aspects. The work is based on paired 4DCTs of six patients treated at the NMPC under the PCG registry. To this end, upright and supine image registration and target propagation, as necessary to optimize the plan on the same target geometry, were developed and a robust comparison between postures was achieved. For each patient, starting from the definition of an optimal supine 3D plan, multiple variables were considered and their impact on the dosimetric comparison assessed: anatomy changes and target geometry, beam angle choice and the flexibility therein, plan robustness and convergence, the magnitude of the interplay effect and the impact of lung modulation in both postures.

5.6.1 Anatomy changes and target geometry

Lung capacity increase, breathing motion reduction and heart position variations were investigated in previous works [78], [81], [82] as main changes of interest for thoracic tumor sites. Marano et al. [78] assessed lung and heart variations on 15 paired CTs, including the six patients used in this study, and found a general lung volume increase of 17% and 9.9% for the left and right lung, respectively. These findings are consistent with the results presented in section 5.5.1 Anatomical differences, DIR and target propagation. They also observed a heart displacement in the caudal direction, that could be beneficial for organ spearing when the thorax is irradiated. However, as also confirmed by the work from Marcus et al [166], the inter-patient variability exceeds the heart displacement magnitude.

Anatomical changes represent a challenge for radiation oncologists who gained their experience in contouring VOIs in supine or prone cases. The quality of contouring on upright imaging data might therefore be impaired. Moreover, because of the shortage of clinical upright MRI [95] and PET [96] imaging systems, the segmentation can only rely on CT scans, characterized by low soft tissue contrast. To overcome this problem, Schreuder et al. [86] suggested starting from upright and supine CT and supine MRI, and to then perform intra-modality image registration between the paired CTs of the same patient to generate synthetic upright MRI images.

In supine therapy, the image segmentation process is also supported by AI tools, but the shortage of available clinical upright images reduces the availability of such tools for upright cases. In this study the TotalSegmentator, trained on a supine dataset, was directly applied to upright images and demonstrated its feasibility through qualitative (see Figure 5.*39*) and quantitative (see Table 5.*8*) QA.
This is an important milestone, as it suggests that at least for segmentation tasks, tools trained on supine data may be applied directly to upright patient positioning or at least would require only little fine-tuning. Considering how important efficiency is in modern radiotherapy, having access to the workflow-accelerating options available for supine treatments is a must also for upright treatments.
The accurate contouring of target and OARs constitutes the first major hurdle in upright treatment planning. To isolate the effects of posture changes from those due to contouring differences, a method to successfully register paired CTs of the same patient was developed. The definition of a registration ROI around the IGTV and the ribcage region made it possible to properly map upright and supine CT voxels and propagate the target structures. Because of the lack of a target ground truth, registration and propagation QA was performed with lung VOIs. The good agreement between original and propagated target VOI volumes and the optimal QA metrics results confirmed the good output obtained from the ROI-restricted DIR.

Notably, the target propagation does not fully represent the tumor morphology changes occurring when the patient takes an upright position. The upright plan would be delivered to a different target geometry with respect to the propagated one used in this work. Therefore, to reflect a real clinical scenario in which supine and upright CT and target VOI are available, the static upright plans were optimized both on the propagated and the M.C. target, when available. Major plan quality differences were found for patient P3, for which the heart dose decreased by 11 pp when the originally contoured IGTV was used. A seemingly strong advantage in cardiac sparing in upright actually turned into a slight disadvantage when using comparable contours. In addition, for patients P5 and P6, the plan on the propagated target resulted in increased OARs dose. This illustrates the challenge of a fair dosimetric comparison between the postures with associated drastically changed anatomies. With the image registration and target propagation step, it was possible to isolate this variable.

5.6.2 Beam angle choice and flexibility

After target propagation, nominal 3D plans optimization was performed through position-specific beam angle adaptation. A direct application of the optimal supine field directions to the upright volumes highlighted the necessity of plan geometry adaptation for patient-specific cases. It emerged that a less outward ribcage and compressed lungs guided the use of more oblique fields in upright position, with respect to the vertical beams preferred in supine therapy to improve lung tissue sparing. Patient P5 was used as a representative case (see Figure 5.*42*) to show lung anatomy changes. In addition, further uncertainties might occur deriving from the displacement of mobile effluence because of body position changes. The pleural fluid moved out of the beam path in upright position, preventing it from affecting the final dose distribution. The employment of oblique beam directions was limited by the presence of arms and shoulders in the beam path. The development of upright treatment positioning devices supporting arms up, as already implemented in some chair systems [167], [168] could overcome this problem.
Anatomy changes between postures, and the consequent optimal plan geometry are extremely patient-specific. For example, for patient P6 it was not possible to reduce lung dose through additional beam inclination, and because of the higher position of the heart, a significant heart dose was observed. Gravity, which pushes the thoracic and abdominal organs in the inferior direction, suggests that better heart sparing may be achieved when treating lung patients upright, but multiple studies reported large inter-patient variability [78], and this is also in accordance with the presented results. In particular, conclusions may not hold up under full consideration of the parameter space. For example, if a patient indicates better heart sparing for plans on a 3D reference, it may not translate to 4D doses. It seems obvious considering that dose degradation through motion is well known, but it is important to underline the effect of various sources of bias on comparison studies. As long as upright is still a rare modality, comparisons will be performed with whatever CT datasets are available. When conducting these studies, it is extremely important to carefully address the variables that influence the outcome.

The high potential of upright therapy, especially for CIRT, lies in the possibility to offer 360 degrees beam angle flexibility without the necessity of a gantry. Yan et al. [169] showed that if pencil beam scanning techniques are available in combination with beam deflection and sitting position, it is possible to reduce the need for a gantry also for complex tumor geometries. This work assessed the impact of the gantry in supine treatments, comparing the nominal plans for which a full 360 degrees beam flexibility was assumed, with plans for which only vertical, horizontal and 45 degrees fields were available. Results show that for all patients, except for P1, a full beam angle flexibility makes it possible to achieve an increased plan quality. Despite possible dosimetric advantages, economic and practicality arguments are to be considered. For example, the delivery of a posterior beam with a fixed vertical beamline on a treatment couch implies that the patient has to be repositioned prone and a new CT scan has to be

acquired. This would increase treatment time as well as sources of error and uncertainties, both resulting from the additional positioning step but also from the necessary propagation of doses between the prone and supine CT.

To understand the feasibility of translating upright therapy into clinical practice, it is paramount to compare it with the actual state of the art. The limited number of available carbon gantries worldwide implies that thoracic treatments in supine position have to be mainly delivered via a fixed beamline. Therefore, a meaningful comparison can be made between the fixed beamline plans (see Table 5.*11*, 4th column) and the nominal upright plans (see Table 5.*10*, 3rd column). The results show that with fixed beam supine plans a lower dose is delivered to the heart for patients P3, P4 and to the lung for patient P6. If a dosimetric equivalence between the two postures can be demonstrated, it would provide a strong argument to leverage the other opportunities offered by upright patient positioning. Moreover, this may represent the only possible treatment modality for patients with breathing impairments in supine position [170], [171].

5.6.3 Plan robustness

To achieve an optimal clinical outcome, the plan quality needs also to be maintained also against systematic errors. For this purpose, robust optimization was computed with standard robust parameters, defined on supine population studies [118]. However, because of a different imaging and positioning system [118], inter-fraction motion variation [165] as well as general experience in upright therapy, larger systematic errors should be considered. Therefore, this framework also considered RA performed with 5 mm setup position uncertainties and 5% range shift. The RA results show that upright plans have comparable robustness with the supine ones, both for standard and increased robust parameters.

5.6.4 Interplay effect magnitude

The interplay effect is the major cause of plan degradation in scanned particle therapy of moving targets, and its evaluation is necessary for a comprehensive upright and supine dosimetric comparison. Studies showed that a lower breathing amplitude occurs in upright position [80], [81], indicating a consequently decreased interplay effect magnitude (see Figure 4.*34*). The patients of the dataset used in this study are characterized by small tumor motion amplitude, and small motion differences between postures, except for patient P2. Patients P1 and P2 are the only cases in which clinically significant target coverage differences occur when interplay doses are compared for the supine and the upright position. No significant differences were found for the other patients, both in single deliveries and accumulated doses in the plan convergence study. Therefore, if the interplay effect is comparable between postures, it might be assumed that also motion mitigation techniques might be similar for upright and supine therapy. In this study, motion management strategies, such as 4D optimization, were not included, since they are usually adopted in clinical practice only for target motion larger than 5 mm [165], [172]. The interplay had only a minor effect on the dose to the lung and the heart. Notably, the increased lung capacity in upright might suggest that part of the irradiated lung volume consists of air instead of tissue [79].

5.6.5 Lung modulation effect

The lung modulation doses were computed starting from the nominal 3D plans, and using the same methodology described in section 3.5.2 Lung modulation doses. Firstly, the dose modulation was achieved through the "Extreme Pmod" value of 0.750 mm (see section 4.2.3 Results). A second method, instead, was based on the definition of the lung tissue pore size (d). The supine d value was derived assuming a Pmod of 0.750 mm. Therefore, the same results

were obtained when the modulated plans derived from the two methods were compared for the supine position (3rd and 5th column of Table 5.*13*).
The upright pore size value was obtained by increasing the supine one by 10%. Notably, a 10% increase in the pore size produces a Pmod increase of about 10% (from 0.750 mm to 0.824 mm). However, the overall effect is negligible, for both patient positions and both dose calculation methods. This is in accordance with the result of the treatment planning study presented in section 4.2 Dosimetric study of lung modulation and interplay effect.

A precise characterization of the variations of the upright anatomical and physiological patterns in the lung region is not trivial, and the outcome is expected to be highly patient specific. For example, the larger air volume inhaled in upright position has been indicated to possibly reduce the dose released in lung tissue [81]. However, an increased inhalation could also be linked to larger blood perfusion in the lung, which is necessary to maintain a proper lung function [173]. This could both reduce the expected advantages of upright therapy and the larger modulation strength of this treatment position.
The low resolution of treatment planning CTs is the main limitation in achieving a complete description of the anatomical effect of the upright position on the lung modulation. A robust comparison between upright and supine lung density is also challenged by the differences between the two CT scanners and their calibration.
These limitations were also present in this study and prevented a more robust investigation of the lung modulation effect in the two positions. In fact, with the use of an *a priori* Pmod and pore size value, the obtained modulated doses do not reflect position differences. The difference mainly derives from the number of voxels in the beam path identified as lung parenchyma, the lung tissue traversed by the beam, and the pore structure size. If the beam angle selection is not optimized for the upright position, the beam path in the lung might be longer (as shown for patient P5). This not only increases the lung dose but could also affect the dose modulation, even if a significant positive correlation between modulation effect and tumor depth in lung was not found in this thesis.

This further demonstrates that the availability of a full beam angle flexibility, achievable either with the gantry or the chair, allows the beam direction with the minimum beam path in lung tissue to be selected.

5.6.6 Study limitations

This study has some limitations. Firstly, the framework was tested on a small patient cohort. This reflects the shortage of paired upright and supine 4DCTs available worldwide. The results of this study not only underline the dependency of the final comparison on individual variables but also demonstrate the impact of patient-specific characteristics. For example, the tumor location in the lung and the motion amplitude can favor one posture or the other. Similarly, differences emerging in a specific variable comparison (beam angle in 3D plans), might not be observed under different conditions (interplay doses). This was expected and initially prompted the development of a framework to compare upright and supine therapy, assessing the impact of multiple factors. Larger cohort studies are needed to derive systematic conclusions on possible tumor location dependencies.

The DIR and propagation method presents some limitations. Ideally the ribcage ROI should enclose the same lung subvolumes in both positions, but it was not possible to identify the exact same lung regions in the paired CTs. The anatomical changes and the different quality of the CT challenged the definition of the optimal ribcage ROI size that should represent the best trade-off between small size, to exclude body regions with large anatomical changes, and big size, to guarantee good anatomical match between supine and upright CT. An additional limitation is the registration and propagation QA only based on the lung VOI, easy to segment both manually and automatically, because of the density contrast with surrounding structures. However, only the structures available from the original dataset and present in both supine and upright ROI for each patient, could be used for QA purposes. The lung VOI

was the only one meeting both requirements. The heart, manually contoured for each patient but not present in every ROI, was not provided as a whole segment by TotalSegmentator, but only as different heart sectors. Therefore, the AI heart contour was completely different from the manually contoured one, segmented as a whole. For the lung, even though TotalSegmentator was trained on a supine dataset, the A.C. QA returned excellent values, justifying their use for the registration QA.
The high quality in the propagation of the lung structure together with the good agreement in the target contour volumes, COM coordinates distance as well as qualitative shape between postures suggests that the ribcage ROI-restricted DIR performed reasonably well.

Ultimately, the chair available at the NMPC for thorax irradiation has a 20 degrees backrest inclination and this was not reproduced in TRiP4D. Plan optimization and dose calculation were computed assuming a vertical backrest. This might represent an additional parameter playing a role in the comparison between postures, especially because the optimal upright patient posture is not yet clear. This parameter is not expected to have an impact on the findings of this thesis, but since vendors offer different beam geometries and conditions, vendor-specific outcomes can derive from the comparison between postures.

5.7 Conclusions

The presented study showed a thorough comparison between upright and supine CIRT of thoracic cancer patients. Through the investigation of multiple variables, the impact of position-specific angle optimization, angle flexibility, as well as target geometry on the final dosimetric comparison was highlighted. In particular, the study demonstrated the clinical benefit of a 360 degrees beam angle flexibility, which cand be provided by the upright posture, without the need for a gantry. Patient-specific characteristics can overshadow the effect of any of the considered parameters. The results of this work underline the importance of a treatment position choice based on patient-specific features, such as lung anatomy, tumor location and motion amplitude.
The main objective of this work was the introduction of a framework to guide the comparison between supine and upright therapy. As indicated by this work, if a dosimetric equivalence between postures can be demonstrated, the economic and technological advantages can be exploited without compromising the clinical outcome. The complete translation into the clinic and the establishment of upright therapy as alternative to gantry-based treatments is only possible if the therapeutic effect is not impaired. Treatment planning studies, like the one presented in this work, can properly investigate the clinical impact of upright therapy and provide the required research evidence.

6 Summary and conclusions

6.1 Context and impact of this work

Radiotherapy, one of the pillars of cancer care, is based on the delivery of a conformal radiation dose to the tumor, while sparing the surrounding normal tissues as much as possible. Particle therapy, because of its physical properties, emerged as an advanced form of radiotherapy. The increased radio biological effectiveness of carbon ions make CIRT an extremely effective treatment for radioresistant, metastatic and complex tumors, like NSCLC [2]. The maximization of dose conformity is also obtained through advanced dose delivery systems, such as active beam scanning and the use of a rotating gantry for the delivery of the beam from multiple angles around the patient.
The clinical progress of CIRT in the treatment of NSCLC has been demonstrated, but shortcomings are still present which overall limit the spread and popularization of CIRT for thoracic tumors [2]. The extremely sharp carbon ion dose deposition is intrinsically sensitive to range changes and uncertainties, which in the treatment of thoracic tumors derive both from the patient breathing motion and the lung tissue heterogeneous microstructure. These effects degrade the final dose distribution, reducing conformity. Using CIRT to its full potential requires precise control over these uncertainties.
However, even if the best possible CIRT is achieved, it is only worthwhile if it can reach the patients that would benefit from it. A major barrier towards widespread CIRT availability lies in the high cost associated with it, including facility installation, operation, and maintenance. A significant contribution to the technological and economic limitations derives from the carbon gantry [10]. Among the 133 particle therapy facilities in operation worldwide, 17 have CIRT available, and only 4 have a gantry, which confirms the high cost of this treatment modality and the numerous challenges associated with the carbon gantry [60]. Because of this, only fixed beamlines, usually horizontal, are available in the majority of the CIRT facilities. Therefore, the definition of the optimal beam direction, which maximizes OAR sparing, is hindered by the limited beam angle flexibility, especially for thoracic tumors including those located in the lung. These limitations, coupled with a wide inter-patient variability, have been indicated as main factors compromising a larger clinical implementation of CIRT [2].
Improving the precision, while at the same time reducing cost are therefore fundamental to offer CIRT for more patients in need. This thesis addressed the first point by focusing on the clinical impact of the anatomical and physiological complexities of CIRT for lung patients, particularly the isolated and combined effects of respiratory motion and lung inhomogeneities. The second point was investigated by a comprehensive analysis of the clinical impact of upright patient positioning, as an advanced gantry-less treatment modality.

The interplay effect, caused by superposition of breathing and beam motion, was indicated as the major cause of dose degradation in CIRT of lung tumors treatment and investigated in depth. Multiple motion mitigation strategies have been proposed and are currently used in clinical practice [174], [175]. 4D optimization strategies have also been reported to improve the robustness of target coverage. However, the use of internal margins, still necessary for these techniques, increases the dose to healthy tissue [98].
The lung modulation effect, deriving from the inhomogeneous microstructure of lung tissue, was described in its physical aspects but only sparsely investigated in clinical-like scenarios [50], [149]. Understanding the treatment quality achievable through CIRT for lung cancer patients requires treatment planning software capable of correctly including motion and lung modulation, validated against experiments, and extensive treatment planning studies. This thesis provides a major milestone in this direction by investigating both motion- and lung modulation- induced dose degradation with the TRiP4D research TPS.

First, to validate the TRiP4D setup regarding lung modulation calculation, cell survival experiments were performed to assess the radiobiological impact of the lung modulation. This is of utmost importance in the context of heavy ion therapy, where the physical dose is amplified by a variable and relatively large RBE. For a thorough understanding of the reduced plan conformity in CIRT of lung treatments, this work investigated the internal motion and tissue heterogeneity as intrinsic dose degradation factors. The clinical impact of modulation and interplay effects was studied in a treatment planning study based on a cohort of eighteen patients. The investigation of the combined effect was assessed for the first time, exploiting the unique features of the TRiP4D dose calculation engine.
This work confirmed that the lung modulation effect is minor when compared to the impact of interplay and demonstrated that it has a negligible clinical effect. Nevertheless, the results underlined the importance of lung modulation degradation when motion mitigation strategies are considered. This is particularly important in standard fractionation schemes: while the interplay effect averages out over multiple fractions, the lung modulation effect is not expected to do so, as it is systematic rather than stochastic. Although minor, it therefore remains as a global drop in dosimetric accuracy. Of great interest is that, when combining the two effects, the lung modulation somewhat reduces the interplay effect. This could possibly have a positive impact on hypo-fractionated treatment schemes.

The interplay and lung modulation effects were investigated, assuming a full beam angle flexibility around the patient, as it would be possible with a gantry in supine position. However, the availability of the gantry is not the current clinical reality. A limited beam angle flexibility can highly impair the conformity of the final plan, especially for thoracic tumor sites. In this context, gantry-less treatment modalities, such as upright therapy, become extremely important. In upright therapy, the rotation of the patient positioning system enables a maximum beam angle flexibility without the necessity of a gantry. An extensive clinical impact assessment of upright therapy is still missing, especially for the thorax and abdomen regions, which change significantly in anatomy when the patient changes posture. The spread of upright therapy as a gantry-less solution is only possible if its clinical outcome is at least non-inferior to supine therapy. This work focused on the investigation of the clinical impact of upright CIRT, through the development of a framework to properly compare it with the standard supine treatment. The results demonstrated that clinical experience based on supine treatments can be translated to upright therapy, which emerges as non-inferior to the standard supine therapy. This work also confirmed the great benefit of a maximum beam angle flexibility that can be provided by the upright patient positioning, without the need for a gantry.

6.2 Research hypothesis

Four research hypotheses defined the scope of this work. In this section, the respective findings given in the previous chapters are discussed.

6.2.1 Clinical impact of lung modulation and anatomical motion on carbon therapy of lung cancer

Hypothesis I:
The effect of lung tissue inhomogeneities on carbon ions and its radio-biological impact can be reproduced and investigated in cell survival experiments.

Material inhomogeneities, characteristic of the lung tissue at a microstructural level, have been widely investigated for the impact they have on particle energy and range. A particle beam traversing density inhomogeneities experiences energy deposition straggling and range broadening, resulting in a degraded final dose distribution, known as the lung

modulation effect. The physical characterization of the dose degradation is not enough, however, in the context of CIRT, due to its high and variable RBE.
The increased biological effect derives from larger LET and RBE of carbon ions, compared to protons. The works by Paz et al. [54] and Zao et al. [55] have previously demonstrated the shift in depth of LET and RBE distributions, for a carbon SOBP traversing an inhomogeneous material. In the first section of Chapter 4 it was demonstrated that an increased cell mortality occurs at the SOBP distal fall-off, downstream of the lung substitute material LN300, due to the shift in depth of high-LET carbon ions. This effect was simulated in TRiP98 and experimentally validated with cell survival experiments. Both TRiP98 simulations and experimental results showed lower cell survival at the SOBP distal fall-off. However, a good agreement between simulated and experimental data could not be found, both in terms of effect magnitude and location in depth. The investigated effect occurs at the SOBP distal edge, where the dose profile is very steep and small positioning errors can lead to large differences of the deposited dose and consequent cell survival. In addition, the measured effect is in general very small and difficult to detect, especially considering the amplitude of the superimposed biological error, and the large variability of the radiobiological behavior of the V79-4 cell line. To provide a conclusive answer, a large number of experiment repetitions, which were overall unfeasible, would be required.
Nevertheless, the introduction of cell experiments permitted investigating the radiobiological impact of the lung modulation effect on lung fibroblasts, reproducing the potential damage to normal tissue cells at the distal edge of the tumor.
The lung modulation effect is not included in clinical applications as a possible source of plan degradation. Firstly, because the clinical CT does not resolve the finest lung inhomogeneities and the calculation of the modulated dose is very computationally demanding. Moreover, the modulation effect has only a minor impact on the plan quality degradation, compared to the motion-related sources of uncertainty.
For a complete understanding of dose uncertainties in CIRT of lung cancer, the clinical impact of the lung modulation effect was investigated individually and in combination with the interplay effect in a treatment planning study.

Hypothesis II:
Interplay and lung modulation effect can be comprehensively investigated through treatment planning studies, and their superposition will lead to clinically relevant dosimetric effects beyond the state of knowledge.

In the second section of Chapter 4, a treatment planning study comparing the clinical impact of lung modulation effect and interplay effect was presented. The interplay effect, causing density changes, and the lung modulation effect, responsible of density inhomogeneities, were investigated both individually and combined to quantify their impact as it would be present in the patient.
The interplay effect is considered the major source of plan degradation in the context of moving targets treated with actively scanned ion beams [151]. Its investigation permitted the development of multiple motion management strategies, some of which are currently employed in clinical practice. On the other hand, the lung modulation was only sparsely investigated with RBE-weighted dose calculations on patient CT [54]. The presented treatment planning study confirmed that severe plan quality degradations are caused by the interplay effect, also for small motion amplitudes. In comparison, the lung modulation effect is responsible for negligible dose deteriorations, even for applied extreme modulation strength. Notably, the lung modulation increases the toxicity mainly in the lung tissue distal to the tumor and the use of treatment margins around the target, as implemented in clinical practice, intrinsically compensates for this small dose shift.

The superposition of the lung modulation to the interplay effect demonstrated how the dose broadening caused by density inhomogeneities can partially compensate for under- and over-doses inside the target caused by motion uncertainties. Therefore, the lung modulation, considered as a negative effect, is responsible for partial target dose recovery when combined with interplay. This mitigating effect of modulation decreases when motion mitigation strategies, such as 4D-optimization and dose fractionation, are considered. Indeed, for improved mitigation of the interplay effect, the lung modulation still persists as a negative effect. Even though the modulation effect of lung heterogeneities plays only a minor role in overall plan quality, it occurs consistently at every fraction, and its relative importance increases with an improved motion control offered by advanced mitigation strategies. Conversely, due to its random nature, interplay degradation becomes smaller after multiple fractions.
The formulated hypothesis was confirmed by the presented results. The treatment planning study investigated for the first time the combination of interplay and modulation effect as they would occur in a real patient case. The results demonstrated the partial compensation of dose broadening on motion-related dose degradation, that was only theorized in previous studies [49], and confirmed that the interplay effect has to be considered in CIRT treatments of lung tumor as the major plan dose degradation factor.

6.2.2 Upright and supine carbon therapy of lung cancer: a 4D dosimetric study

Hypothesis III:
Clinical experience from supine therapy can be translated to upright therapy through a treatment planning study framework which can show that upright therapy is non-inferior to supine therapy.

A renewed interest in upright therapy was firstly driven by the economic and technological advantages of a fixed beam line, compared to the gantry. Moreover, a fixed horizontal beam line, as available in the majority of the CIRT facilities, is not adequate for achieving an optimal lung treatment plan, if the patient is in supine position. Upright therapy enables the rotation to be shifted from the beam delivery to the patient positioning system, allowing for a full beam angle flexibility around the patient, with a horizontal beam line.
The clinical outcome of upright therapy needs to be investigated prior to its transition into clinical practice, and its non-inferiority to the standard supine treatment has to be demonstrated. Upright and supine therapy comparison can be performed through treatment planning studies, but the results are impaired by numerous variables playing a role. Chapter 5 presented a framework to robustly compare paired upright and supine CIRT plans for lung patients, based on the translation of the clinical experience of supine treatments.
This work demonstrated the complexity of paired plans comparison, through the investigation of the variables of interest (e.g. target geometry, beam angle flexibility, robust parameter), and underlined the effect of patient-specific characteristics on the results of the comparison.
Firstly, the impact of the target geometry was assessed through the development of a DIR method to propagate the target between the supine and upright CT. A different target geometry can significantly impact the dose distribution and to isolate the effects of posture changes from those due to the contouring differences, the upright plans were optimized both on the original IGTV (when available) and the propagated contour. The target contour presents a core dilemma of comparisons: on the one hand, the comparison should be performed on the actual target, including morphological changes related to the posture change. On the other hand, changes in the target contour may not accurately represent the morphological changes, but instead differences in the contour quality between postures. The latter may be influenced by differences in the CT scanner used, the availability of MRI scanners in both postures, the use of auto-contouring tools, or the experience or effort by the radiologist. For example, guidelines on how to extend the GTV to form a CTV or PTV may be available for supine treatments, but the same is not currently available for upright. If the available contour does not accurately reflect the GTV/CTV morphology, any comparison is biased by

volume and position differences of the segmentation. Hence, it should be considered best practice to cross-check comparisons made on segmented volumes against those made on propagated volumes. To this end, the DIR method for target contour propagation has been instrumental, as without the constraint on the ribcage VOI, the vastly different anatomy in the two postures causes DIR algorithms to fail completely.
We also demonstrated that the target margins recipe, directly translated from supine therapy population studies [118], is applicable to the upright plans and no differences were found for larger robust parameters.
The investigation of lung modulation in the two treatment positions confirmed that lung tissue density inhomogeneities remain a negligible dose degradation factor also in the presence of changes in the thorax anatomy. Indeed, a non-significant dose degradation was found for the two treatment postures, even for Pmod values (0.750 mm and 0.824 mm) much larger than the average values of the inflated lung. Notably, considerable modulation strength is produced by large airway generations, such as the trachea, that are resolved in the clinical CT.

Among the consequences of the upright patient positioning, a lower motion amplitude was indicated as a possible clinical advantage of upright therapy [81], but it was only found in one patient of the used dataset. Overall, a comparable interplay effect magnitude was found in the two positions. This suggests that motion mitigating techniques could be translated from the supine to the upright treatment.
Despite the small number of patients included, the developed framework was shown to be a valid tool to directly compare treatment planning strategies in upright and supine posture, which showed among several interesting findings the non-inferiority of upright therapy. The dosimetric equivalence between the two postures was demonstrated, and it would provide a strong argument to influence the other opportunities offered by upright patient positioning. Upright position may also represent the only possible treatment modality for patients with breathing impairments in supine position [176].

The investigation of the clinical impact of different beam angle flexibility was a central aspect of this thesis.

Hypothesis IV:
Lung cancer therapy also with carbon ions greatly benefits from a flexible beam angle arrangement, and it can be shown that upright patient positioning can provide this benefit.

In CIRT, the high potential of upright therapy lies in the possibility to offer 360 degrees beam angle flexibility without the need for a gantry.
The tumor position in the lung and its relative position to surrounding OARs in the two postures can strongly affect the beam angle choice. For some patients, the use of position-specific beam geometry did not improve the plan quality. In another case, upright-specific beam angle selection suggested favorable beam directions for this treatment position. In particular, the lung anatomy changes and the movement of the pleural effusion between postures, allowed favorable beam directions to be identified in upright position.
The optimal beam direction was found assuming in both positions 360 degrees angle availability. If a horizontal fixed beamline is available, the maximum beam angle flexibility is only possible with the chair positioning system. Otherwise, a gantry is required.
This work also demonstrated that a superior plan quality is achieved when a full beam angle flexibility is available, with respect to the fixed beam line, in supine position. In addition to possible dosimetric advantages, practicality arguments need to be considered. For example, the delivery of a posterior beam with a fixed vertical beamline on a treatment couch implies that the patient has to be repositioned prone and a new CT scan has to be acquired. This would increase treatment time, sources of error and uncertainties, both resulting from the additional positioning step but also from the necessary propagation of dose between the prone and supine CT.

Further comparisons performed for a fixed beamline between supine and upright plans showed that an overall comparable plan quality can be obtained. Notably, patient-specific characteristics, such as the tumor position relative to surrounding OARs, had a strong impact on the results.
It is important to underline that, for the supine fixed beam plans, a treatment room in which horizontal, vertical and 45 degrees fixed beamlines are present was assumed. If a single horizontal beamline is available, as it is in the majority of the CIRT facilities, the angle choice becomes even more limited, and the plan quality would be consequently considerably lower if not outright clinically impossible. The treatment of a central thoracic lesion only with lateral beams would lead to significant exposure, likely of both lungs, which for many patients would be unacceptable. Excess lung doses are linked to radiation induced pneumonia, excess heart dose to critical heart failure in the years after treatment. Without flexible beam angles, bringing the benefit of CIRT to lung cancer treatments would be drastically limited by the increased risk of severe side effects. Upright patient postures would not only decrease footprint and cost for new CIRT facilities, they would also boost the potential of available fixed beamlines. This would maximize the benefit of CIRT.
A dosimetric equivalence between upright and supine CIRT is the key to bring this advanced treatment option to a large number of patients. This thesis took a major step in this direction by demonstrating the effect of various parameters on the dosimetric comparison between postures, and, especially, by showing that new beam angles can be leveraged to increase the plan quality for upright treatments. A definitive conclusion requires a larger patient cohort than was available for the time span of this work, the framework developed here already is guiding ongoing developments in the field.

6.3 Strengths and limitations

This thesis investigates CIRT of lung cancer patients from different aspects, addressing multiple sources of dose uncertainty and reduced conformity, as they occur in a real clinical scenario. A wider spread of CIRT is possible if its clinical outcome is thoroughly investigated, under realistic clinical conditions, and if the potential benefits offered by advanced treatment modalities are assessed.
We performed the first experimental validation of the radiobiological effect of lung modulation on lung fibroblast, to quantify its impact in terms of cell damage. The outcome of the experiments was strongly influenced by positioning uncertainties and intrinsic biological variability, which overall contributed to a mismatch between the experimental results and dosimetric simulations in TRiP98. Although the repetition of the experiments would have increased statistical robustness and mitigated the biological error, the considerable time required for data analysis made the experiment repetitions unfeasible. Moreover, the small effect size and higher than expected biological variability would have required a much higher sample size than was feasible in the scope of this study.

After the characterization of the radio biological effect of lung modulation, this study proceeded with the investigation of the actual clinical impact of lung modulation, focusing on its superposition with the interplay effect. As the interplay is known to be the major sources of uncertainty in CIRT of lung cancer, the evaluation of the combined effect had already proposed [49]. The treatment planning study exploited the unique features of the GSI TPS TRiP4D with which the dose distributions can be computed including the lung modulation both alone and in combination with the interplay effect. Thanks to the implementation of the FFT, TRiP98 also has a reasonably fast dose calculation time for lung modulation doses.
However, no inter-fraction motions, that are expected to change the amount of air in the lung, and therefore the modulating effect, were assessed. In addition, a patient-specific modulation map was not created. The modulation

effect is directly proportional to the airway cross-sectional area, which is subjected to inter-patient variation and to changes in different regions of the lung and for different conditions of the same patient. Nevertheless, because of the limited impact lung modulation has on the overall dose degradation, it is assumed that the use of multiple modulation values could adequately represent the clinical impact. Because of the lack of a patient specific modulation map, this work also did not investigate the possibility of optimizing for the plan degradation, even if a dedicated function is present in TRiP98 [54]. Moreover, the most significant dose degradation derives from larger airway structures that are resolved in the clinical CT and therefore included in the treatment plan.

With the investigation of gantry-less treatment solutions this thesis provides a complete overview of CIRT of lung cancer, assessing emerging modalities with the potential of improving dose conformity.
A treatment planning study framework was developed to robustly compare supine and upright therapy, and it demonstrated the dosimetric non-inferiority of the upright treatment posture. This represents an important step toward making upright therapy feasible for thoracic patients, though it is still in its early stages.
The used approach was based on translating the knowledge from supine therapy and highlighted that more investigation is needed to confirm the results. Indeed, these findings are based on six patients, so they are not yet widely applicable. This limitation reflects a common issue in the field, since upright therapy is just starting to be studied in clinical settings for thorax, abdomen and pelvis regions [84], [177]. More data and a broader application of the presented framework will be needed before drawing stronger conclusions. For example, the used dataset did not include any daily imaging that would be required to assess upright inter-fraction changes and positioning reproducibility in comparison to supine therapy.

Ultimately, the lung anatomical and functional changes in upright position, that could impact the lung modulation effect in upright radiotherapy, were included in the presented framework, but some limitations are present. The lung modulation model and its implementation in TRiP98 rely on a fixed global parameter (Pmod/pore size) that does not adapt to patient specific characteristics and any anatomical variations between supine and upright position. The research by Matsumoto et al. [83] showed that the cross-sectional area of the airways is enlarged in the upright position and this might amplify the modulation effects. This factor was included with the use of a different pore size value for the supine and upright CTs. Also in this case, the pore size was pre-defined as a constant and global value and was not derived as a patient-specific and variable parameter.
The inherent limitations of the CT resolution, the overall not optimal CT quality and the different scanner characteristics of the upright and supine imaging systems, also precluded a robust assessment of the lung microstructure changes between postures. Therefore, a fine reconstruction of the lung tissue, able to resolve patient- and posture-specific density inhomogeneities, was not yet possible.
Given the early-stage development of upright radiotherapy, and the current shortage of available upright clinical CTs, the primary clinical hurdles are the definition of optimal positioning strategies, consistent inter- and intra-fraction reproducibility, and motion management strategies. For now, lung modulation remains a secondary dose degradation factor in CIRT of lung cancer, both in supine and upright position, as demonstrated comprehensively in this work.

6.4 Outlook

An outlook on the next steps towards the implementation of the findings of this thesis into advanced CIRT techniques is provided in this section.

6.4.1 Towards a more precise implementation of the lung modulation effect

The definition of a patient-specific modulation map is the required step to precisely evaluate the clinical impact of the lung modulation under variable conditions. The lung modulation strength mainly depends on the diameter of the air cavities, which could vary with the respiration phase, the disease progress or the patient treatment position. Therefore, the quantification of the airway generation diameter can be translated into a modulation strength map, by direct application of the mathematical model. If a precise airway segmentation and luminal area definition can be derived from the clinical CT, it would be possible to implement the lung modulation dose degradation without further image acquisition. For this purpose, good quality patient CTs are required. In particular, the inferior region of the lung, where only the smallest airway generations are present, is usually prone to image artifacts because of the diaphragm movement.

The dependency of dose modulation on the diameter of the air cavities implies that a different effect magnitude might be expected in upright position. To precisely assess this, the information about the density inhomogeneities has to be extracted from paired supine and upright CTs. This is not possible both because of the intrinsically low resolution of the clinical CT, and because of the different characteristics of the supine and upright CT scanners. The first limitation can be overcome with the method proposed by Flatten et al. [53], based on the derivation of a patient specific Pmod from the HU histogram of the CT. However, the HU histograms of the supine and upright CT can only be compared if the same calibration curves are used. This was not the case for the dataset of paired upright and supine CTs used in this work. Therefore, the following step could be the derivation of new CT calibration curves, using the LN300 lung substitute material as a calibration insert for the two scanners.

The definition of airway structure and lumen cross-sectional area would highly benefit from the use of AI tools, already widely in use for automatic structure segmentation [162]. Unfortunately, because of the shortage of upright thoracic CT, AI segmentation tools are still not available for upright applications.

The use of AI would also decrease the computational time of the dose calculation. Quarz et al. [178], in their work, proposed an AI-driven approach; for a faster dose calculation algorithm in TRiP98. The AI-based dose engine they developed predicts the absorbed dose and the α and β parameters required for standard RBE-weighted dose calculation. The same quantities are also employed in modulated dose computations through a convolution with a Gaussian distribution. This additional feature would be interesting to consider lung modulation in dose calculation, given the high computational time that they require. A dedicated AI tool could be trained with a large dataset of thoracic CTs and respective target contours, such as the one available in TCIA, for PB generation, alongside the clinically used field directions.

A further step would be the assessment of the lung modulation clinical impact in hypofractionated and motion-controlled treatments, in which the interplay effect is minimized. For example, several motion mitigation strategies were investigated in the past years. In particular, our group proposed the MP4D [179] and MP4D-RT [125] strategies, demonstrating their feasibility through experimental tests performed at "Centro Nazionale di Adroterapia Oncologica" (CNAO) in Pavia, Italy.

Ultimately, it is paramount to assess the lung modulation effect in clinically representative scenarios, in which multiple inter-patient parameters play a role in the final effect magnitude. This study (see section 4.2 Dosimetric study of lung modulation and interplay effect) only investigated the correlation with the tumor depth in the lungs, but other factors could be included. For example, Flatten et al. [145] investigated the dependencies of proton BP modulation on a CT-based lung tumor phantom. Their study analyzed the tumor depth in lung, the tumor size and shape, the thickness of the thorax wall and the tissue distal to the tumor. The impact of these parameters could be analyzed in a cohort of patient CTs, through a multiple regression analysis.

However, overall, even assuming extreme lung modulation, larger than expected in reality, did not result in meaningful degradation. Therefore, a conclusion that can be drawn from this thesis is that further modeling of the lung modulation will not lead to a great refinement of the magnitude of its effect.

6.4.2 Towards the clinical implementation of upright CIRT of lung tumors

The upright therapy research field is still in large development, and multiple questions need to be answered before a full clinical translation can happen. This thesis proposed a framework for robust comparison between supine and upright CIRT of lung tumors, but the necessary next step is the application and verification of such a method to a larger patient cohort. The treatment planning studies are a recognized tool for the investigation of treatment modality feasibility, essential at the preclinical stage. The developed framework requires good quality paired CTs, better still 4DCTs, which are usually limited because of time-related and dose-related constraints. This data shortage is a shared problem in the upright community and multiple clinical and research centers are sharing the effort to fill this gap. For example, the development of synthetic CT or 4DCT was proposed together with the use of innovative anthropomorphic moving phantoms, perfectly suitable for research purposes [180]. The definition of synthetic images is a fundamental step to compensate for the limited availability of upright functional images, such as PET and MRI, whose increased soft tissue contrast is important for diagnostic purposes. With a larger availability of upright image sets, the development of AI tools would be possible, making image registration and contour segmentation much faster.

In this work intra-fractional motion and its impact on supine and upright plans were investigated. However, inter-fraction position stability is fundamental for precise treatment delivery. Patient position reproducibility between following fractions is essential in CIRT and it has to be investigated in the upright treatment of thoracic tumors. Therefore, the availability of weekly/daily CT, and possibly weekly 4DCT, would allow for the quantification of upright therapy inter-fractional motion. The availability of complete 4D image datasets is also essential for the assessment of motion mitigation strategies in upright treatment position. For example, the quantification of interplay related dose degradation could be performed with the real-time ion dose planning and delivery system (RIDOS), a comprehensive system for real-time dose reconstruction in particle therapy, interfaced with the 4D dose delivery system (4D-DDS) available at CNAO [126], [127], [181]. RIDOS was developed for accurate monitoring and verification of the delivered dose in the presence of motion and has the great advantage of being completely non-invasive. This makes it a powerful tool for the investigation of motion related uncertainties in early clinical applications.

Ultimately, the upright positioning system has significant potential for advancing pre-clinical research in particle therapy. Specifically, the Small-Animal Spot Scanning Hadron Arc Therapy (SASHA) project [182] introduces a novel pre-clinical framework where small animals are positioned upright and subjected to spot-scanning proton arc therapy. In this approach, upright positioning plays a dual role: it enables the practical implementation of arc particle therapy [73] and simultaneously addresses key challenges of pre-clinical particle therapy research, such as the limitations imposed by small beam sizes and range accuracy.

6.5 Summary

The presented study provides a complete overview of the radiobiological, clinical, and technological aspects of CIRT for lung cancer, offering a broader understanding of related challenges and potential solutions.

Lung fibroblasts survival experiments and TRiP98 simulations confirmed a localized increase of cell mortality at the distal SOBP fall-off due to primary carbon ion range straggling in lung tissue. The treatment planning study of eighteen lung cancer patients confirmed that the clinical relevance of the lung modulation effect is negligible compared to motion-induced uncertainties. This study also demonstrated that while the interplay effect dominates plan degradation, lung tissue heterogeneities produce a systematic modulation that partially compensates for the dose degradation caused by interplay.

An increased plan conformity is possible if the beam angle flexibility is maximized. In fact, without the gantry, the optimization of the best treatment plan for thoracic patients in supine position is challenging. This thesis investigated upright therapy as an advanced gantry-less solution, able to provide full beam angle flexibility around the patient with a horizontal fixed beam line. The presented comparative study of upright versus supine therapy reveals that the dosimetric equivalence can be achieved, making upright therapy a promising, cost-effective alternative to gantry-based treatments. The presented framework will guide future treatment planning studies, required for a translation of upright therapy into clinical practice. Moreover, technological and economic advantages of upright therapy could be exploited if the dosimetric non-inferiority of this treatment position is confirmed.

Together, these findings will improve the precision of CIRT by clarifying the roles of lung modulation, motion mitigation, and treatment positioning while presenting a solution to overcome the technological and practical limitations that nowadays limit its broader implementation in lung cancer treatment.

Bibliography

[1] J. Ferlay *et al.*, “Global Cancer Observatory: Cancer Today,” International Agency for Research on Cancer. Accessed: Oct. 20, 2025. [Online]. Available: https://gco.iarc.who.int/today

[2] S. Liang, G. Zhou, and W. Hu, “Research Progress of Heavy Ion Radiotherapy for Non-Small-Cell Lung Cancer,” *Int. J. Mol. Sci.*, vol. 23, no. 4, p. 2316, Feb. 2022, doi: 10.3390/ijms23042316.

[3] A. K. Ganti, A. B. Klein, I. Cotarla, B. Seal, and E. Chou, “Update of Incidence, Prevalence, Survival, and Initial Treatment in Patients With Non–Small Cell Lung Cancer in the US,” *JAMA Oncol.*, vol. 7, no. 12, p. 1824, Dec. 2021, doi: 10.1001/jamaoncol.2021.4932.

[4] G. Delaney, S. Jacob, C. Featherstone, and M. Barton, “The role of radiotherapy in cancer treatment,” *Cancer*, vol. 104, no. 6, pp. 1129–1137, Sep. 2005, doi: 10.1002/cncr.21324.

[5] M. Douglass, “Eric J. Hall and Amato J. Giaccia: Radiobiology for the radiologist,” *Australas. Phys. Eng. Sci. Med.*, vol. 41, no. 4, pp. 1129–1130, Dec. 2018, doi: 10.1007/s13246-018-0684-1.

[6] D. Chen *et al.*, “Interaction between lymphopenia, radiotherapy technique, dosimetry, and survival outcomes in lung cancer patients receiving combined immunotherapy and radiotherapy,” *Radiotherapy and Oncology*, vol. 150, pp. 114–120, Sep. 2020, doi: 10.1016/j.radonc.2020.05.051.

[7] A. McWilliam, A. Abravan, K. Banfill, C. Faivre-Finn, and M. van Herk, “Demystifying Cardiac Dose in RTOG-0617,” *International Journal of Radiation Oncology*Biology*Physics*, vol. 111, no. 3, p. S125, Nov. 2021, doi: 10.1016/j.ijrobp.2021.07.285.

[8] J. D. Bradley *et al.*, “Standard-dose versus high-dose conformal radiotherapy with concurrent and consolidation carboplatin plus paclitaxel with or without cetuximab for patients with stage IIIA or IIIB non-small-cell lung cancer (RTOG 0617): a randomised, two-by-two factorial phase 3 study,” *Lancet Oncol.*, vol. 16, no. 2, pp. 187–199, Feb. 2015, doi: 10.1016/S1470-2045(14)71207-0.

[9] D. Harris, G. K. King, and P. J. Bergman, “Radiation Therapy Toxicities,” *Veterinary Clinics of North America: Small Animal Practice*, vol. 27, no. 1, pp. 37–46, Jan. 1997, doi: 10.1016/S0195-5616(97)50004-0.

[10] C. Graeff, L. Volz, and M. Durante, “Emerging technologies for cancer therapy using accelerated particles,” Jul. 01, 2023, *Elsevier B.V.* doi: 10.1016/j.ppnp.2023.104046.

[11] H. Paganetti *et al.*, “Roadmap: Proton therapy physics and biology,” *Phys. Med. Biol.*, vol. 66, no. 5, Mar. 2021, doi: 10.1088/1361-6560/abcd16.

[12] Ph. D. , H. Paganetti, *Proton Therapy Physics*. Boca Raton: CRC Press, 2025. doi: 10.1201/9781032616858.

[13] Y. Ding, H. H. Barrett, M. A. Kupinski, Y. Vinogradskiy, M. Miften, and B. L. Jones, “Objective assessment of the effects of tumor motion in radiation therapy,” *Med. Phys.*, vol. 46, no. 7, pp. 3311–3323, Jul. 2019, doi: 10.1002/mp.13601.

[14] S. España and H. Paganetti, “Uncertainties in planned dose due to the limited voxel size of the planning CT when treating lung tumors with proton therapy,” *Phys. Med. Biol.*, vol. 56, no. 13, pp. 3843–3856, Jul. 2011, doi: 10.1088/0031-9155/56/13/007.

[15] S. Chinniah, A. J. Deisher, M. G. Herman, J. E. Johnson, A. Mahajan, and R. L. Foote, “Rotating Gantries Provide Individualized Beam Arrangements for Charged Particle Therapy,” *Cancers (Basel).*, vol. 15, no. 7, p. 2044, Mar. 2023, doi: 10.3390/cancers15072044.

[16] K. M. Kraus, E. Heath, and U. Oelfke, “Dosimetric consequences of tumour motion due to respiration for a scanned proton beam,” *Phys. Med. Biol.*, vol. 56, no. 20, pp. 6563–6581, Oct. 2011, doi: 10.1088/0031-9155/56/20/003.

[17] C. Bert, S. O. Grözinger, and E. Rietzel, “Quantification of interplay effects of scanned particle beams and moving targets,” *Phys. Med. Biol.*, vol. 53, no. 9, pp. 2253–2265, May 2008, doi: 10.1088/0031-9155/53/9/003.

[18] U. Fano, “Penetration of Protons, Alpha Particles, and Mesons,” *Annu. Rev. Nucl. Sci.*, vol. 13, no. 1, pp. 1–66, Dec. 1963, doi: 10.1146/annurev.ns.13.120163.000245.

[19] D. Schardt, T. Elsässer, and D. Schulz-Ertner, “Heavy-ion tumor therapy: Physical and radiobiological benefits,” Feb. 19, 2010. doi: 10.1103/RevModPhys.82.383.

[20] R. Serber, “Nuclear Reactions at High Energies,” *Physical Review*, vol. 72, no. 11, pp. 1114–1115, Dec. 1947, doi: 10.1103/PhysRev.72.1114.

[21] M. Durante, J. Debus, and J. S. Loeffler, “Physics and biomedical challenges of cancer therapy with accelerated heavy ions,” Dec. 01, 2021, *Springer Nature*. doi: 10.1038/s42254-021-00368-5.

[22] U. S. Srinivas, B. W. Q. Tan, B. A. Vellayappan, and A. D. Jeyasekharan, “ROS and the DNA damage response in cancer,” *Redox Biol.*, vol. 25, p. 101084, Jul. 2019, doi: 10.1016/J.REDOX.2018.101084.

[23] Z. Nikitaki *et al.*, “Key biological mechanisms involved in high-LET radiation therapies with a focus on DNA damage and repair,” Mar. 31, 2022, *Cambridge University Press*. doi: 10.1017/erm.2022.6.

[24] K. H. Chadwick and H. P. Leenhouts, “Physics in Medicine & Biology A Molecular Theory of Cell Survival.”

[25] S. J. McMahon, “The linear quadratic model: Usage, interpretation and challenges,” *Phys. Med. Biol.*, vol. 64, no. 1, Jan. 2019, doi: 10.1088/1361-6560/aaf26a.

[26] H. Paganetti and D. Giantsoudi, “Relative Biological Effectiveness Uncertainties and Implications for Beam Arrangements and Dose Constraints in Proton Therapy,” *Semin. Radiat. Oncol.*, vol. 28, no. 3, pp. 256–263, Jul. 2018, doi: 10.1016/J.SEMRADONC.2018.02.010.

[27] H. Willers *et al.*, “Toward A variable RBE for proton beam therapy,” *Radiotherapy and Oncology*, vol. 128, no. 1, pp. 68–75, Jul. 2018, doi: 10.1016/J.RADONC.2018.05.019.

[28] U.Amaldi *et al.*, “A facility for Tumour Therapy and Biomedical Researchin South-Eastern Europe,” 2019.

[29] O. Jäkel, G. Kraft, and C. P. Karger, “The history of ion beam therapy in Germany,” *Z. Med. Phys.*, vol. 32, no. 1, pp. 6–22, Feb. 2022, doi: 10.1016/J.ZEMEDI.2021.11.003.

[30] M. Krämer and M. Scholz, “Treatment planning for heavy-ion radiotherapy: calculation and optimization of biologically effective dose,” 2000.

[31] T. Pfuhl, T. Friedrich, and M. Scholz, “Prediction of Cell Survival after Exposure to Mixed Radiation Fields with the Local Effect Model,” *Radiat. Res.*, vol. 193, no. 2, p. 130, Dec. 2019, doi: 10.1667/RR15456.1.

[32] F. Tommasino, E. Scifoni, and M. Durante, “New Ions for Therapy,” *Int. J. Part. Ther.*, vol. 2, no. 3, pp. 428–438, Dec. 2015, doi: 10.14338/IJPT-15-00027.1.

[33] C. Voyant, D. Julian, R. Roustit, K. Biffi, and C. Lantieri, “Biological effects and equivalent doses in radiotherapy: A software solution,” *Reports of Practical Oncology & Radiotherapy*, vol. 19, no. 1, pp. 47–55, Jan. 2014, doi: 10.1016/j.rpor.2013.08.004.

[34] M. Anzai *et al.*, “Safety and efficacy of carbon-ion radiotherapy alone for stage III non-small cell lung cancer,” *Anticancer Res.*, vol. 40, no. 1, pp. 379–386, 2020, doi: 10.21873/anticanres.13963.

[35] J. Yap, A. De Franco, and S. Sheehy, “Future Developments in Charged Particle Therapy: Improving Beam Delivery for Efficiency and Efficacy,” Dec. 09, 2021, *Frontiers Media S.A.* doi: 10.3389/fonc.2021.780025.

[36] U. Weber and G. Kraft, “Design and construction of a ripple filter for a smoothed depth dose distribution in conformal particle therapy,” 1999.

[37] M. Krämer and M. Durante, “Ion beam transport calculations and treatment plans in particle therapy,” *European Physical Journal D*, vol. 60, no. 1, pp. 195–202, 2010, doi: 10.1140/epjd/e2010-00077-8.

[38] Daniel Richter, “Treatment planning for tumors with residual motion in scanned ion beam therapy,” GSI Helmholtzzentrum für Schwerionenforschung , Darmstadt, 2012.

[39] S. Ramella *et al.*, “Local Control and Toxicity of Adaptive Radiotherapy Using Weekly CT Imaging: Results from the LARTIA Trial in Stage III NSCLC,” *Journal of Thoracic Oncology*, vol. 12, no. 7, pp. 1122–1130, Jul. 2017, doi: 10.1016/J.JTHO.2017.03.025.

[40] H. H. Liu *et al.*, “Assessing Respiration-Induced Tumor Motion and Internal Target Volume Using Four-Dimensional Computed Tomography for Radiotherapy of Lung Cancer,” *International Journal of Radiation Oncology*Biology*Physics*, vol. 68, no. 2, pp. 531–540, Jun. 2007, doi: 10.1016/j.ijrobp.2006.12.066.

[41] Marta Fischetti, “Development of a detector for inter-fractional monitoring in carbon ion therapy treatment,” Sapienza university of Rome, 2020.

[42] A. M. Ali, J. B. Greenwood, A. Hounsell, and C. McGarry, “A systematic review of the dosimetric consequences of the interplay effect,” Jun. 01, 2025, *Associazione Italiana di Fisica Medica*. doi: 10.1016/j.ejmp.2025.105004.

[43] P. R. Poulsen, J. Eley, U. Langner, C. B. Simone, and K. Langen, “Efficient Interplay Effect Mitigation for Proton Pencil Beam Scanning by Spot-Adapted Layered Repainting Evenly Spread out Over the Full Breathing Cycle,” *Int. J. Radiat. Oncol. Biol. Phys.*, vol. 100, no. 1, pp. 226–234, Jan. 2018, doi: 10.1016/j.ijrobp.2017.09.043.

[44] E. R. Weibel, *Geometry and Dimensions of Airways of the Respiratory Zone. In:Morphometry of the Human Lung*. Berlin, Heidelberg: Springer Berlin Heidelberg, 1963. doi: 10.1007/978-3-642-87553-3_6.

[45] “ChatGPT. Human Respiratory System Illustration (AI-Generated). OpenAI, 2025].”

[46] M. Uries, M. Goiteins, W. R. Holleyo, and G. T. Y. Cheno, “Degradation of the Bragg peak due to inhomogeneitiest,” 1986.

[47] G. O. Sawakuchi, U. Titt, D. Mirkovic, and R. Mohan, “Density heterogeneities and the influence of multiple Coulomb and nuclear scatterings on the Bragg peak distal edge of proton therapy beams,” *Phys. Med. Biol.*, vol. 53, no. 17, pp. 4605–4619, Sep. 2008, doi: 10.1088/0031-9155/53/17/010.

[48] U. Titt *et al.*, “Degradation of proton depth dose distributions attributable to microstructures in lung-equivalent material,” *Med. Phys.*, vol. 42, no. 11, pp. 6425–6432, Nov. 2015, doi: 10.1118/1.4932625.

[49] M. Witt *et al.*, “On the Way to Accounting for Lung Modulation Effects in Particle Therapy of Lung Cancer Patients—A Review,” Nov. 01, 2024, *Multidisciplinary Digital Publishing Institute (MDPI)*. doi: 10.3390/cancers16213598.

[50] T. Printz Ringbæk *et al.*, “Modulation power of porous materials and usage as ripple filter in particle therapy,” *Phys. Med. Biol.*, vol. 62, no. 7, pp. 2892–2909, Mar. 2017, doi: 10.1088/1361-6560/aa5c28.

[51] H. Bichsel, T. Hiraoka, and K. Omata, “Aspects of Fast-Ion Dosimetry,” 2000.

[52] K. S. Baumann, M. Witt, U. Weber, R. Engenhart-Cabillic, and K. Zink, “An efficient method to predict and include Bragg curve degradation due to lung-equivalent materials in Monte Carlo codes by applying a density modulation,” *Phys. Med. Biol.*, vol. 62, no. 10, pp. 3997–4016, Apr. 2017, doi: 10.1088/1361-6560/aa641f.

[53] V. Flatten *et al.*, “Estimating the modulating effect of lung tissue in particle therapy using a clinical CT voxel histogram analysis,” *Phys. Med. Biol.*, vol. 66, no. 18, Sep. 2021, doi: 10.1088/1361-6560/ac176e.

[54] A. E. S. Paz *et al.*, “Compensating for beam modulation due to microscopic lung heterogeneities in carbon ion therapy treatment planning,” *Med. Phys.*, vol. 48, no. 12, pp. 8052–8061, Dec. 2021, doi: 10.1002/mp.15292.

[55] J. Zhao, B. Chen, M. Moyers, Z. Yang, S. Yang, and W. Wang, “Impact of porous lung substitute on linear energy transfer (LET) assessed via Monte Carlo simulation and CR-39 measurement with a carbon-ion beam,” *Med. Phys.*, vol. 52, no. 4, pp. 2593–2605, Apr. 2025, doi: 10.1002/mp.17671.

[56] W. Tinganelli and M. Durante, “Carbon Ion Radiobiology,” *Cancers (Basel).*, vol. 12, no. 10, p. 3022, Oct. 2020, doi: 10.3390/cancers12103022.

[57] A. L. Elaimy *et al.*, “History and Overview of Proton Therapy,” in *Proton Therapy - Current Status and Future Directions*, IntechOpen, 2021. doi: 10.5772/intechopen.95959.

[58] E. W. Collings, L. Lu, N. Gupta, and M. D. Sumption, “Accelerators, Gantries, Magnets and Imaging Systems for Particle Beam Therapy: Recent Status and Prospects for Improvement,” Feb. 15, 2022, *Frontiers Media S.A.* doi: 10.3389/fonc.2021.737837.

[59] K. Noda *et al.*, “Recent progress and future plans of heavy-ion cancer radiotherapy with HIMAC,” *Nucl. Instrum. Methods Phys. Res. B*, vol. 406, pp. 374–378, Sep. 2017, doi: 10.1016/J.NIMB.2017.04.021.

[60] “PTCOG: Particle Therapy facilities in clinical operation. Accessed on 06/03/2026; Available from: https://www.ptcog.site/index.php/facilities-in-operation-public.”

[61] L. Volz *et al.*, “Opportunities and challenges of upright patient positioning in radiotherapy,” Sep. 21, 2024, *Institute of Physics*. doi: 10.1088/1361-6560/ad70ee.

[62] R. Fuchs, U. Weinrich, and G. E. Sust, “Assembly of the carbon beam gantry at the Heidelberg Ion Therapy (HIT) Accelerator,” 2008.

[63] E. D. Yorke, P. Keall, and F. Verhaegen, “Anniversary Paper: Role of medical physicists and the AAPM in improving geometric aspects of treatment accuracy and precision,” 2008, *John Wiley and Sons Ltd*. doi: 10.1118/1.2836420.

[64] L. J. Verhey, M. Goitein, P. McNulty, J. E. Munzenrider, and H. D. Suit, “Precise positioning of patients for radiation therapy,” *International Journal of Radiation Oncology*Biology*Physics*, vol. 8, no. 2, pp. 289–294, Feb. 1982, doi: 10.1016/0360-3016(82)90530-2.

[65] “P-Cure. Patient Centric Proton Therapy Website (2024). Available at: www.pcure.com (Accessed April, 26 2024).”

[66] “Leo Cancer Care Ltd. Leo Cancer Care Ltd. Website (2024). Available at: www.leocancercare.com (Accessed April. 26, 2024).”.

[67] J. Feldman *et al.*, “Commissioning of a novel gantry-less proton therapy system,” *Front. Oncol.*, vol. 14, 2024, doi: 10.3389/fonc.2024.1417393.

[68] J. Feldman *et al.*, “Study of upright patient positioning reproducibility in image-guided proton therapy for head and neck cancers,” *Radiotherapy and Oncology*, vol. 201, Dec. 2024, doi: 10.1016/j.radonc.2024.110572.

[69] X. Zhang *et al.*, “Development of an isocentric rotating chair positioner to treat patients of head and neck cancer at upright seated position with multiple nonplanar fields in a fixed carbon-ion beamline,” *Med. Phys.*, vol. 47, no. 6, pp. 2450–2460, Jun. 2020, doi: 10.1002/mp.14115.

[70] S. Yan, T. A. Ngoma, W. Ngwa, and T. R. Bortfeld, “Global democratisation of proton radiotherapy,” *Lancet Oncol.*, vol. 24, no. 6, pp. e245–e254, Jun. 2023, doi: 10.1016/S1470-2045(23)00184-5.

[71] T. Underwood, S. Yan, T. Bortfeld, V. Grégoire, and T. Lomax, “A Strengths, Weaknesses, Opportunities, and Threats (SWOT) Analysis for Gantry-Less Upright Radiation Therapy,” *International Journal of Radiation Oncology*Biology*Physics*, vol. 122, no. 5, pp. 1337–1343, Aug. 2025, doi: 10.1016/j.ijrobp.2025.02.039.

[72] S. Boisbouvier, A. Boucaud, R. Tanguy, and V. Grégoire, “Upright patient positioning for pelvic radiotherapy treatments,” *Tech. Innov. Patient Support Radiat. Oncol.*, vol. 24, pp. 124–130, Dec. 2022, doi: 10.1016/j.tipsro.2022.11.003.

[73] S. Mein *et al.*, “Particle arc therapy: Status and potential,” *Radiotherapy and Oncology*, vol. 199, p. 110434, Oct. 2024, doi: 10.1016/j.radonc.2024.110434.

[74] L. Volz, Y. Sheng, M. Durante, and C. Graeff, “Considerations for Upright Particle Therapy Patient Positioning and Associated Image Guidance,” Jul. 29, 2022, *Frontiers Media S.A.* doi: 10.3389/fonc.2022.930850.

[75] M. Jinzaki *et al.*, “Development of Upright Computed Tomography With Area Detector for Whole-Body Scans,” *Invest. Radiol.*, vol. 55, no. 2, pp. 73–83, Feb. 2020, doi: 10.1097/RLI.0000000000000603.

[76] J. Hrbacek *et al.*, “PTCOG Ocular Statement: Expert Summary of Current Practices and Future Developments in Ocular Proton Therapy,” *International Journal of Radiation Oncology*Biology*Physics*, vol. 120, no. 5, pp. 1307–1325, Dec. 2024, doi: 10.1016/j.ijrobp.2024.06.017.

[77] Y. Yokoyama *et al.*, “Effect of gravity on brain structure as indicated on upright computed tomography,” *Sci. Rep.*, vol. 11, no. 1, p. 392, Jan. 2021, doi: 10.1038/s41598-020-79695-z.

[78] J. Marano *et al.*, “Relative thoracic changes from supine to upright patient position: A proton collaborative group study,” *J. Appl. Clin. Med. Phys.*, vol. 24, no. 12, Dec. 2023, doi: 10.1002/acm2.14129.

[79] Y. Yamada *et al.*, “Comparison of inspiratory and expiratory lung and lobe volumes among supine, standing, and sitting positions using conventional and upright CT,” *Sci. Rep.*, vol. 10, no. 1, Dec. 2020, doi: 10.1038/s41598-020-73240-8.

[80] Duisters C, Beurskens H, and Nijsten S, “Palliative chest irradiation in sitting position in patients with bulky advanced lung cancer,” *Radiother Oncol.* , vol. 79, no. 3, pp. 285–287, Jun. 2006.

[81] J. Yang, D. Chu, L. Dong, and L. E. Court, “Advantages of simulating thoracic cancer patients in an upright position,” *Pract. Radiat. Oncol.*, vol. 4, no. 1, Jan. 2014, doi: 10.1016/j.prro.2013.04.005.

[82] R. Takazakura, M. Takahashi, N. Nitta, and K. Murata, “Diaphragmatic Motion in the Sitting and Supine Positions: Healthy Subject Study Using a Vertically Open Magnetic Resonance System,” *Journal of Magnetic Resonance Imaging*, vol. 19, no. 5, pp. 605–609, May 2004, doi: 10.1002/jmri.20051.

[83] S. Matsumoto *et al.*, “Difference in the airway luminal area between the standing and supine positions using upright and conventional computed tomography,” *Clinical Anatomy*, vol. 34, no. 8, pp. 1150–1156, Nov. 2021, doi: 10.1002/ca.23763.

[84] Y. Nomura *et al.*, “Comparison of supine and upright postures for liver respiratory motion management in radiotherapy,” *Med. Phys.*, vol. 52, no. 9, Sep. 2025, doi: 10.1002/mp.18111.

[85] J. E. Reiff, M. Werner-Wasik, R. K. Valicenti, and M. S. Huq, “Changes in the size and location of kidneys from the supine to standing positions and the implications for block placement during total body irradiation,” *International Journal of Radiation*

*Oncology*Biology*Physics*, vol. 45, no. 2, pp. 447–449, Sep. 1999, doi: 10.1016/S0360-3016(99)00208-4.

[86] A. N. Schreuder, N. Paragios, M. Kissick, M. Lis, T. S. A. Underwood, and R. Mackie, "The use of image synthesis techniques in target and roi delineation in the upright position," *J. Appl. Clin. Med. Phys.*, vol. 24, no. 8, Aug. 2023, doi: 10.1002/acm2.14079.

[87] A. R. Hayes, F. S. Gayzik, D. P. Moreno, R. S. Martin, and J. D. Stitzel, "Comparison of organ location, morphology, and rib coverage of a midsized male in the supine and seated positions," *Comput. Math. Methods Med.*, vol. 2013, 2013, doi: 10.1155/2013/419821.

[88] J. Ulman *et al.*, "Exploring patient perceptions of the current breast radiotherapy pathway and a future upright radiotherapy solution," *Radiography*, vol. 31, no. 6, p. 103157, Oct. 2025, doi: 10.1016/j.radi.2025.103157.

[89] S. Rahim, J. Korte, N. Hardcastle, S. Hegarty, T. Kron, and S. Everitt, "Upright Radiation Therapy—A Historical Reflection and Opportunities for Future Applications," *Front. Oncol.*, vol. 10, Feb. 2020, doi: 10.3389/fonc.2020.00213.

[90] M. Krämer, O. Jäkel, T. Haberer, G. Kraft, D. Schardt, and U. Weber, "Treatment planning for heavy-ion radiotherapy: physical beam model and dose optimization," 2000. [Online]. Available: www.iop.org

[91] G. C. Pereira, M. Traughber, and R. F. Muzic, "The Role of Imaging in Radiation Therapy Planning: Past, Present, and Future," *Biomed Res. Int.*, vol. 2014, pp. 1–9, 2014, doi: 10.1155/2014/231090.

[92] R. W. M. Underberg, F. J. Lagerwaard, J. P. Cuijpers, B. J. Slotman, J. R. van Sörnsen de Koste, and S. Senan, "Four-dimensional CT scans for treatment planning in stereotactic radiotherapy for stage I lung cancer," *International Journal of Radiation Oncology*Biology*Physics*, vol. 60, no. 4, pp. 1283–1290, Nov. 2004, doi: 10.1016/j.ijrobp.2004.07.665.

[93] M. W. Kissick *et al.*, "Calculation method for novel upright CT scanner isodose curves," *J. Appl. Clin. Med. Phys.*, vol. 25, no. 7, Jul. 2024, doi: 10.1002/acm2.14377.

[94] J. M. Slagowski *et al.*, "Technical assessment of a novel vertical CT system for upright radiotherapy simulation and treatment planning," *Med. Phys.*, vol. 53, no. 2, Feb. 2026, doi: 10.1002/mp.70312.

[95] "ASG Upright MRI. (n.d.). ASG Upright MRI. https://www.asguprightmri.com."

[96] S. Vandenberghe *et al.*, "Walk-through flat panel total-body PET: a patient-centered design for high throughput imaging at lower cost using DOI-capable high-resolution

monolithic detectors," *Eur. J. Nucl. Med. Mol. Imaging*, vol. 50, no. 12, pp. 3558–3571, Oct. 2023, doi: 10.1007/s00259-023-06341-x.

[97] ICRU, "ICRU REPORT 93: Prescribing, Recording, and Reporting Light Ion Beam Therapy," 2016.

[98] C. Graeff, M. Durante, and C. Bert, "Motion mitigation in intensity modulated particle therapy by internal target volumes covering range changes," *Med. Phys.*, vol. 39, no. 10, pp. 6004–6013, 2012, doi: 10.1118/1.4749964.

[99] G. Heilemann *et al.*, "Clinical Implementation and Evaluation of Auto-Segmentation Tools for Multi-Site Contouring in Radiotherapy," *Phys. Imaging Radiat. Oncol.*, vol. 28, p. 100515, Oct. 2023, doi: 10.1016/j.phro.2023.100515.

[100] M. Wolf, K. Anderle, M. Durante, and C. Graeff, "Robust treatment planning with 4D intensity modulated carbon ion therapy for multiple targets in stage IV non-small cell lung cancer," *Phys. Med. Biol.*, vol. 65, no. 21, Nov. 2020, doi: 10.1088/1361-6560/aba1a3.

[101] J. A. Dowling and L. M. O'Connor, "Deformable image registration in radiation therapy," Dec. 01, 2020, *John Wiley and Sons Ltd*. doi: 10.1002/jmrs.446.

[102] B. Rigaud *et al.*, "Deformable image registration for radiation therapy: principle, methods, applications and evaluation," *Acta Oncol. (Madr).*, vol. 58, no. 9, pp. 1225–1237, Sep. 2019, doi: 10.1080/0284186X.2019.1620331.

[103] K. K. Brock, S. Mutic, T. R. McNutt, H. Li, and M. L. Kessler, "Use of image registration and fusion algorithms and techniques in radiotherapy: Report of the AAPM Radiation Therapy Committee Task Group No. 132," *Med. Phys.*, vol. 44, no. 7, pp. e43–e76, Jul. 2017, doi: 10.1002/mp.12256.

[104] P. Decazes, P. Hinault, O. Veresezan, S. Thureau, P. Gouel, and P. Vera, "Trimodality PET/CT/MRI and Radiotherapy: A Mini-Review," *Front. Oncol.*, vol. 10, Feb. 2021, doi: 10.3389/fonc.2020.614008.

[105] J. Yuen *et al.*, "An international survey on the clinical use of rigid and deformable image registration in radiotherapy," *J. Appl. Clin. Med. Phys.*, vol. 21, no. 10, pp. 10–24, Oct. 2020, doi: 10.1002/acm2.12957.

[106] J. Barber *et al.*, "Deforming to Best Practice: Key considerations for deformable image registration in radiotherapy," *J. Med. Radiat. Sci.*, vol. 67, no. 4, pp. 318–332, Dec. 2020, doi: 10.1002/jmrs.417.

[107] J. B. A. Maintz and M. A. Viergever, "A survey of medical image registration," *Med. Image Anal.*, vol. 2, no. 1, pp. 1–36, Mar. 1998, doi: 10.1016/S1361-8415(01)80026-8.

[108] F. P. M. Oliveira and J. M. R. S. Tavares, “Medical image registration: a review,” *Comput. Methods Biomech. Biomed. Engin.*, vol. 17, no. 2, pp. 73–93, Jan. 2014, doi: 10.1080/10255842.2012.670855.

[109] B. Rigaud *et al.*, “Evaluation of Deformable Image Registration Methods for Dose Monitoring in Head and Neck Radiotherapy,” *Biomed Res. Int.*, vol. 2015, pp. 1–16, 2015, doi: 10.1155/2015/726268.

[110] R. Kashani *et al.*, “Objective assessment of deformable image registration in radiotherapy: A multi-institution study,” *Med. Phys.*, vol. 35, no. 12, pp. 5944–5953, Dec. 2008, doi: 10.1118/1.3013563.

[111] D. Müller, I. Soto-Rey, and F. Kramer, “Towards a guideline for evaluation metrics in medical image segmentation,” *BMC Res. Notes*, vol. 15, no. 1, p. 210, Dec. 2022, doi: 10.1186/s13104-022-06096-y.

[112] O. U. Aydin *et al.*, “On the usage of average Hausdorff distance for segmentation performance assessment: hidden error when used for ranking,” *Eur. Radiol. Exp.*, vol. 5, no. 1, Dec. 2021, doi: 10.1186/s41747-020-00200-2.

[113] A. A. Taha and A. Hanbury, “Metrics for evaluating 3D medical image segmentation: Analysis, selection, and tool,” *BMC Med. Imaging*, vol. 15, no. 1, Aug. 2015, doi: 10.1186/s12880-015-0068-x.

[114] J. Wasserthal *et al.*, “TotalSegmentator: Robust Segmentation of 104 Anatomic Structures in CT Images • Content codes,” *Radiol. Artif. Intell.*, vol. 5, no. 5, 2023, doi: 10.5281/zenodo.6802613.

[115] A. Fedorov *et al.*, “3D Slicer as an image computing platform for the Quantitative Imaging Network,” *Magn. Reson. Imaging*, vol. 30, no. 9, pp. 1323–1341, Nov. 2012, doi: 10.1016/j.mri.2012.05.001.

[116] J. Wolfgang *et al.*, “Plastimatch- an open source software suite for radiotherapy image processing,” 2010. [Online]. Available: https://www.researchgate.net/publication/268523129

[117] M. E. Wolf, “Robust optimization in 4D treatment planning for carbon ion therapy of lung tumors,” PhD thesis, Tu Darmstadt, 2019.

[118] M. van Herk, P. Remeijer, C. Rasch, and J. V. Lebesque, “The probability of correct target dosage: dose-population histograms for deriving treatment margins in radiotherapy,” *International Journal of Radiation Oncology*Biology*Physics*, vol. 47, no. 4, pp. 1121–1135, Jul. 2000, doi: 10.1016/S0360-3016(00)00518-6.

[119] H. J. Ball, L. Santanam, S. Senan, J. A. Tanyi, M. van Herk, and P. J. Keall, “Results from the AAPM Task Group 324 respiratory motion management in radiation oncology survey,” *J. Appl. Clin. Med. Phys.*, vol. 23, no. 11, Nov. 2022, doi: 10.1002/acm2.13810.

[120] D. Richter *et al.*, “Upgrade and benchmarking of a 4D treatment planning system for scanned ion beam therapy,” *Med. Phys.*, vol. 40, no. 5, 2013, doi: 10.1118/1.4800802.

[121] T. Steinsberger *et al.*, “Extension of RBE-weighted 4D particle dose calculation for non-periodic motion,” *Physica Medica*, vol. 91, pp. 62–72, Nov. 2021, doi: 10.1016/j.ejmp.2021.10.009.

[122] C. Graeff, “Motion mitigation in scanned ion beam therapy through 4D-optimization,” *Physica Medica*, vol. 30, no. 5, pp. 570–577, Jul. 2014, doi: 10.1016/j.ejmp.2014.03.011.

[123] H. Li *et al.*, “AAPM Task Group Report 290: Respiratory motion management for particle therapy,” *Med. Phys.*, vol. 49, no. 4, pp. e50–e81, Apr. 2022, doi: 10.1002/mp.15470.

[124] A. E. Lujan, J. M. Balter, and R. K. Ten Haken, “A method for incorporating organ motion due to breathing into 3D dose calculations in the liver: Sensitivity to variations in motion,” *Med. Phys.*, vol. 30, no. 10, pp. 2643–2649, Oct. 2003, doi: 10.1118/1.1609057.

[125] Timo Steinsberger, “Development and experimental validation of adaptive conformal particle therapy,” Dissertation, Technische Universität Darmstadt, Darmstadt, 2022.

[126] C. Galeone *et al.*, “Real-time delivered dose assessment in carbon ion therapy of moving targets,” *Phys. Med. Biol.*, vol. 69, no. 20, p. 205001, Oct. 2024, doi: 10.1088/1361-6560/ad7d59.

[127] C. Galeone *et al.*, “Real-time motion modeling and treatment verification for irregular motion in carbon ion therapy: a feasibility study,” *Phys. Med. Biol.*, vol. 70, no. 16, p. 165009, Aug. 2025, doi: 10.1088/1361-6560/adf592.

[128] T. P. Ringbæk *et al.*, “Calculation of the Beam-Modulation Effect of the Lung in Carbon Ion and Proton Therapy With Deterministic Pencil Beam Algorithms,” *Front. Phys.*, vol. 8, Nov. 2020, doi: 10.3389/fphy.2020.568176.

[129] J. M. Burg *et al.*, “Experimental determination of modulation power of lung tissue for particle therapy,” *Phys. Med. Biol.*, vol. 66, no. 24, Dec. 2021, doi: 10.1088/1361-6560/ac3e0d.

[130] L. P. Kaplan *et al.*, “Plan quality assessment in clinical practice: Results of the 2020 ESTRO survey on plan complexity and robustness,” *Radiotherapy and Oncology*, vol. 173, pp. 254–261, Aug. 2022, doi: 10.1016/j.radonc.2022.06.005.

[131] C. R. Hansen, M. Hussein, U. Bernchou, R. Zukauskaite, and D. Thwaites, “Plan quality in radiotherapy treatment planning – Review of the factors and challenges,” *J. Med. Imaging Radiat. Oncol.*, vol. 66, no. 2, pp. 267–278, Mar. 2022, doi: 10.1111/1754-9485.13374.

[132] V. Hernandez *et al.*, “What is plan quality in radiotherapy? The importance of evaluating dose metrics, complexity, and robustness of treatment plans,” *Radiotherapy and Oncology*, vol. 153, pp. 26–33, Dec. 2020, doi: 10.1016/j.radonc.2020.09.038.

[133] A. van’t Riet, A. C. A. Mak, M. A. Moerland, L. H. Elders, and W. van der Zee, “A conformation number to quantify the degree of conformality in brachytherapy and external beam irradiation: Application to the prostate,” *International Journal of Radiation Oncology*Biology*Physics*, vol. 37, no. 3, pp. 731–736, Feb. 1997, doi: 10.1016/S0360-3016(96)00601-3.

[134] S. M. Bentzen *et al.*, “Quantitative Analyses of Normal Tissue Effects in the Clinic (QUANTEC): An Introduction to the Scientific Issues,” *International Journal of Radiation Oncology*Biology*Physics*, vol. 76, no. 3, pp. S3–S9, Mar. 2010, doi: 10.1016/j.ijrobp.2009.09.040.

[135] L. B. Marks *et al.*, “Use of Normal Tissue Complication Probability Models in the Clinic,” *Int. J. Radiat. Oncol. Biol. Phys.*, vol. 76, no. 3 SUPPL., Mar. 2010, doi: 10.1016/j.ijrobp.2009.07.1754.

[136] T. Elsässer *et al.*, “Quantification of the relative biological effectiveness for ion beam radiotherapy: Direct experimental comparison of proton and carbon ion beams and a novel approach for treatment planning,” *Int. J. Radiat. Oncol. Biol. Phys.*, vol. 78, no. 4, pp. 1177–1183, Nov. 2010, doi: 10.1016/j.ijrobp.2010.05.014.

[137] S. R. M. S. , W. K. Weyrather, “RBE for carbon track-segment irradiation in cell lines of differing repair capacity,” *Int. J. Radiat. Biol.*, vol. 75, no. 11, pp. 1357–1364, Jan. 1999, doi: 10.1080/095530099139232.

[138] T. Friedrich, U. Scholz, T. ElsaSser, M. Durante, and M. Scholz, “Systematic analysis of RBE and related quantities using a database of cell survival experiments with ion beam irradiation,” *J. Radiat. Res.*, vol. 54, no. 3, pp. 494–514, May 2013, doi: 10.1093/jrr/rrs114.

[139] O. Sokol *et al.*, “In vitro measurement of proton RBE: A multi-centric comparison using a harmonized setup,” *Clin. Transl. Radiat. Oncol.*, vol. 53, p. 100978, Jul. 2025, doi: 10.1016/j.ctro.2025.100978.

[140] C. P. Karger, O. Jäkel, H. Palmans, and T. Kanai, “Dosimetry for ion beam radiotherapy,” *Phys. Med. Biol.*, vol. 55, no. 21, pp. R193–R234, Nov. 2010, doi: 10.1088/0031-9155/55/21/R01.

[141] K. Kainz, “Radiation Oncology Physics: A Handbook for Teachers and Students,” *Med. Phys.*, vol. 33, no. 6Part1, pp. 1920–1920, May 2006, doi: 10.1118/1.2201870.

[142] J. D. Chapman, E. A. Blakely, K. C. Smith, R. C. Urtasun, J. T. Lyman, and C. A. Tobias, “Radiation biophysical studies with mammalian cells and a modulated carbon ion beam.,” *Radiat. Res.*, vol. 74, no. 1, pp. 101–11, Apr. 1978.

[143] P. L. K. A. S. and, B. MARPLES, “Low dose hyper-radiosensitivity and increased radioresistance in mammalian cells,” *Int. J. Radiat. Biol.*, vol. 71, no. 6, pp. 721–735, Jan. 1997, doi: 10.1080/095530097143725.

[144] M.C. Martire, “Dosimetric Study of Lung Modulation and Motion Effects in Carbon ion Therapy for Lung Cancer,” *ArXiv*, 2026.

[145] V. Flatten, K. S. Baumann, U. Weber, R. Engenhart-Cabillic, and K. Zink, “Quantification of the dependencies of the Bragg peak degradation due to lung tissue in proton therapy on a CT-based lung tumor phantom,” *Phys. Med. Biol.*, vol. 64, no. 15, Aug. 2019, doi: 10.1088/1361-6560/ab2611.

[146] J. Winter, M. Ellerbrock, O. Jäkel, S. Greilich, and M. Bangert, “Analytical modeling of depth-dose degradation in heterogeneous lung tissue for intensity-modulated proton therapy planning,” *Phys. Imaging Radiat. Oncol.*, vol. 14, pp. 32–38, Apr. 2020, doi: 10.1016/j.phro.2020.05.001.

[147] G. D. Hugo, “Data from 4D Lung Imaging of NSCLC Patients,” 2016, *The Cancer Imaging Archive*. Accessed: Jan. 08, 2026. [Online]. Available: https://doi.org/10.7937/K9/TCIA.2016.ELN8YGLE

[148] S. Balik *et al.*, “Evaluation of 4-dimensional Computed Tomography to 4-dimensional Cone-Beam Computed Tomography Deformable Image Registration for Lung Cancer Adaptive Radiation Therapy,” *International Journal of Radiation Oncology*Biology*Physics*, vol. 86, no. 2, pp. 372–379, Jun. 2013, doi: 10.1016/j.ijrobp.2012.12.023.

[149] K. S. Baumann *et al.*, “Effects of the Bragg peak degradation due to lung tissue in proton therapy of lung cancer patients,” *Radiation Oncology*, vol. 14, no. 1, Oct. 2019, doi: 10.1186/s13014-019-1375-0.

[150] Matthias Witt, “Modulationseffekte von Kohlenstoffionen bei der Bestrahlung von Lungen,” Master’s Thesis, Technische Hochschule Mittelhessen (THM), Standort Gießen, 2014.

[151] C. Bert and M. Durante, “Motion in radiotherapy: Particle therapy,” Aug. 21, 2011. doi: 10.1088/0031-9155/56/16/R01.

[152] A. Jakobi, R. Perrin, A. Knopf, and C. Richter, “Feasibility of proton pencil beam scanning treatment of free-breathing lung cancer patients,” *Acta Oncol. (Madr).*, vol. 57, no. 2, pp. 203–210, Feb. 2018, doi: 10.1080/0284186X.2017.1355107.

[153] C. Graeff, “Robustness of 4D-optimized scanned carbon ion beam therapy against interfractional changes in lung cancer,” *Radiotherapy and Oncology*, vol. 122, no. 3, pp. 387–392, Mar. 2017, doi: 10.1016/j.radonc.2016.12.017.

[154] A. Chi, H. Chen, S. Wen, H. Yan, Z. Liao, and R. O. Author, “Comparison of particle beam therapy and stereotactic body radiotherapy for early stage non-small cell lung cancer: A systematic review and hypothesis-generating meta-analysis HHS Public Access Author manuscript,” *Radiother Oncol*, vol. 123, no. 3, pp. 346–354, 2017, doi: 10.1016/j.radonc.

[155] S. Spautz *et al.*, “Comparison of 3D and 4D robustly optimized proton treatment plans for non-small cell lung cancer patients with tumour motion amplitudes larger than 5 mm,” *Phys. Imaging Radiat. Oncol.*, vol. 27, Jul. 2023, doi: 10.1016/j.phro.2023.100465.

[156] A. Meijers *et al.*, “Evaluation of interplay and organ motion effects by means of 4D dose reconstruction and accumulation,” *Radiotherapy and Oncology*, vol. 150, pp. 268–274, Sep. 2020, doi: 10.1016/j.radonc.2020.07.055.

[157] M. H. Phillips, E. Pedroni, H. Blattmann, T. Boehringer, A. Coray, and S. Scheib, “Effects of respiratory motion on dose uniformity with a charged particle scanning method,” *Phys. Med. Biol.*, vol. 37, no. 1, pp. 223–233, Jan. 1992, doi: 10.1088/0031-9155/37/1/016.

[158] H. Paganetti, “Range uncertainties in proton therapy and the role of Monte Carlo simulations,” Jun. 07, 2012. doi: 10.1088/0031-9155/57/11/R99.

[159] J. G. Eley, W. D. Newhauser, D. Richter, R. Lüchtenborg, N. Saito, and C. Bert, “Robustness of target dose coverage to motion uncertainties for scanned carbon ion beam tracking therapy of moving tumors,” *Phys. Med. Biol.*, vol. 60, no. 4, pp. 1717–1740, Feb. 2015, doi: 10.1088/0031-9155/60/4/1717.

[160] A. Duetschler *et al.*, “A motion model-guided 4D dose reconstruction for pencil beam scanned proton therapy,” *Phys. Med. Biol.*, vol. 68, no. 11, Jun. 2023, doi: 10.1088/1361-6560/acd518.

[161] M. C. Martire, L. Volz, M. Durante, M. Pankuch, and C. Graeff, “Upright and supine particle therapy of lung cancer: A 4D dosimetric comparison,” *Med. Phys.*, vol. 53, no. 3, Mar. 2026, doi: 10.1002/mp.70377.

[162] A. C. Erdur *et al.*, “Deep learning for autosegmentation for radiotherapy treatment planning: State-of-the-art and novel perspectives,” *Strahlentherapie und Onkologie*, vol. 201, no. 3, pp. 236–254, Mar. 2025, doi: 10.1007/s00066-024-02262-2.

[163] J. M. Pakela, A. Knopf, L. Dong, A. Rucinski, and W. Zou, “Management of Motion and Anatomical Variations in Charged Particle Therapy: Past, Present, and Into the Future,” Mar. 09, 2022, *Frontiers Media S.A.* doi: 10.3389/fonc.2022.806153.

[164] A. C. Knopf *et al.*, “Clinical necessity of multi-image based (4DMIB) optimization for targets affected by respiratory motion and treated with scanned particle therapy – A comprehensive review,” Apr. 01, 2022, *Elsevier Ireland Ltd*. doi: 10.1016/j.radonc.2022.02.018.

[165] B. Knäusl *et al.*, “A review of the clinical introduction of 4D particle therapy research concepts,” Jan. 01, 2024, *Elsevier Ireland Ltd*. doi: 10.1016/j.phro.2024.100535.

[166] K. C. Marcus, G. Svensson, L. P. Rhodes, and P. M. Mauch, “Mantle irradiation in the upright position: A technique to reduce the volume of lung irradiated in patients with bulky mediastinal hodgkin’s disease,” *International Journal of Radiation Oncology*Biology*Physics*, vol. 23, no. 2, pp. 443–447, Jan. 1992, doi: 10.1016/0360-3016(92)90766-B.

[167] N. H. T. K. and colleagues at the P. M. C. C. (Melbourne, A. J. Korte, “Prototype upright positioning system integrated with a LINAC .”

[168] “Leo Cancer Care Ltd. (2025). Meet Marie – Marie particle therapy solution [Product webpage]. Retrieved August 6, 2025, from https://leocancercare.com/solutions/particle-therapy/marie/.”

[169] S. Yan, H. M. Lu, J. Flanz, J. Adams, A. Trofimov, and T. Bortfeld, “Reassessment of the Necessity of the Proton Gantry: Analysis of Beam Orientations from 4332 Treatments at the Massachusetts General Hospital Proton Center over the Past 10 Years,” *Int. J. Radiat. Oncol. Biol. Phys.*, vol. 95, no. 1, pp. 224–233, May 2016, doi: 10.1016/j.ijrobp.2015.09.033.

[170] R. E. McCarroll *et al.*, “Reproducibility of patient setup in the seated treatment position: A novel treatment chair design,” *J. Appl. Clin. Med. Phys.*, vol. 18, no. 1, pp. 223–229, 2017, doi: 10.1002/acm2.12024.

[171] E. Glatstein, “Palliative chest irradiation in sitting position in patients with bulky advanced lung cancer,” *Yearbook of Oncology*, vol. 2008, pp. 194–196, Jan. 2008, doi: 10.1016/s1040-1741(08)79068-7.

[172] Y. Seppenwoolde *et al.*, “Precise and real-time measurement of 3D tumor motion in lung due to breathing and heartbeat, measured during radiotherapy,” *International Journal of Radiation Oncology*Biology*Physics*, vol. 53, no. 4, pp. 822–834, Jul. 2002, doi: 10.1016/S0360-3016(02)02803-1.

[173] P. X. Zhou and S. X. Zhang, “Functional lung imaging in thoracic tumor radiotherapy: Application and progress,” Sep. 23, 2022, *Frontiers Media S.A.* doi: 10.3389/fonc.2022.908345.

[174] K. Shirai *et al.*, “Clinical outcomes using carbon-ion radiotherapy and dose-volume histogram comparison between carbon-ion radiotherapy and photon therapy for T2b-4N0M0 non-small cell lung cancer—A pilot study,” *PLoS One*, vol. 12, no. 4, p. e0175589, Apr. 2017, doi: 10.1371/journal.pone.0175589.

[175] J. Boda-Heggemann *et al.*, “Deep Inspiration Breath Hold—Based Radiation Therapy: A Clinical Review,” *International Journal of Radiation Oncology*Biology*Physics*, vol. 94, no. 3, pp. 478–492, Mar. 2016, doi: 10.1016/j.ijrobp.2015.11.049.

[176] R. W. Miller, A. A. Raubitschek, F. S. Harrington, J. Van de Geijn Ovadia, J. Ovadia, and E. Glatstein, “An isocentric chair for the simulation and treatment of radiation therapy patients,” *International Journal of Radiation Oncology*Biology*Physics*, vol. 21, no. 2, pp. 469–473, Jul. 1991, doi: 10.1016/0360-3016(91)90798-9.

[177] K. Oguma *et al.*, “Simulation Study of Upright Prostate Radiation Therapy: Comparison of Upright and Supine Anatomy and Dose-Volumetric Factors,” *Pract. Radiat. Oncol.*, vol. 15, no. 5, pp. 497–508, Sep. 2025, doi: 10.1016/j.prro.2025.04.007.

[178] A. Quarz *et al.*, “An AI Dose Engine for Fast Carbon Ion Treatment Planning,” *Int. J. Part. Ther.*, vol. 17, p. 100936, Dec. 2025, doi: 10.1016/j.ijpt.2025.100936.

[179] M. Lis *et al.*, “Dosimetric Validation of a System to Treat Moving Tumors Using Scanned Ion Beams That Are Synchronized With Anatomical Motion,” *Front. Oncol.*, vol. 11, Sep. 2021, doi: 10.3389/fonc.2021.712126.

[180] A. Bakhtiari Moghaddam *et al.*, “A dynamic anthropomorphic phantom for end-to-end testing in image- and surface-guided adaptive radiotherapy,” *Med. Phys.*, vol. 52, no. 11, Nov. 2025, doi: 10.1002/mp.70107.

[181] S. Giordanengo *et al.*, “RIDOS: A new system for online computation of the delivered dose distributions in scanning ion beam therapy,” *Physica Medica*, vol. 60, pp. 139–149, Apr. 2019, doi: 10.1016/j.ejmp.2019.03.029.

[182] L. Volz, A. El Beit, T. Steinsberger, L. El Ouali, M. Durante, and C. Graeff, “Small-Animal Spot-scanning Hadron Arc Therapy (SASHA),” *Int. J. Part. Ther.*, vol. 12, p. 100337, Jun. 2024, doi: 10.1016/j.ijpt.2024.100337.

List of Abbreviations

AAPM – American Association of Physics in Medicine
A.C. – Automatically Contoured
AHD – Average Hausdorff Distance
AI – Artificial Intelligence
AP – Anterior–Posterior
ART – Adaptive Radiotherapy
BP – Bragg Peak
CC – Cranio–Caudal
CIRT – Carbon Ion Radiation Therapy
CN – Conformity Number
CNAO – Centro Nazionale di Adroterapia Oncologica
COM – Center of Mass
CT – Computed Tomography
CTV – Clinical Target Volume
DDS – Dose Delivery System
DIR – Deformable Image Registration
DNA – Deoxyribonucleic Acid
DOF – Degree of Freedom
DSBs – Double-Strand Breaks
DSC – Dice Similarity Coefficient
DVF – Deformation Vector Field
DVH – Dose Volume Histogram
EQD2 – Equivalent Dose in 2 Gy Fraction
FFT – Fast Fourier Transform
FFD – Free-Form Deformation
FN – False Negative
FP – False Positive
FOV – Field of View
FWHM – Full Width at Half Maximum
GTV – Gross Tumor Volume
HD – Hausdorff Distance
HI – Homogeneity Index
HIT – Heidelberg Ion Therapy
HU – Hounsfield Units
IARC – International Agency for Research on Cancer
IC – Ionization Chamber
ICE – Inverse Consistency Error
IES – Iso Energy Slice
IGRT – Image-Guided Radiotherapy
IMPT – Intensity-Modulated Particle Therapy
IRR – Increased Radio Resistance

IS – Inferior–Superior–Inferior
ITV – Internal Target Volume
LBL – Lawrence Berkeley Laboratory
LEM – Local Effect Model
LET – Linear Energy Transfer
LLL– Left Lower Lobe
LQ – Linear-Quadratic
LR – Left–Right
LUL– Left Upper Lobe
M.C. – Manually Contoured
MC – Monte Carlo
MIT – Marburg Ion Beam Therapy Center
MRI – Magnetic Resonance Imaging
MSE – Mean Standard Error
NIRS – National Institute of Radiological Sciences
NMPC – Northwestern Medicine Proton Center
NSCLC – Non-Small Cell Lung Cancer
NT – Normal Tissue
NTCP – Normal Tissue Complication Probability
OARs – Organs at Risk
PA – Posterior–Anterior
PB – Pencil Beam
PCG – Proton Collaborative Group
PET – Positron Emission Tomography
PMMA – Polymethyl Methacrylate
PTV – Planning Target Volume
QA – Quality Assurance
QUANTEC – Quantitative Analyses of Normal Tissue Effects in the Clinic
RA – Robustness Analysis
RBE – Relative Biological Effectiveness
RIDOS – Real time Ion Dose planning and delivery System
RIL – Radiation-Induced Lymphopenia
RIR – Rigid Image Registration
ROI – Region of Interest
ROS – Reactive Oxygen Species
RUL – Right Upper Lobe
RML – Right Middle Lobe
RLL – Right Lower Lobe
SASHA – Small Animal spot-Scanning Hadron Arc
SCLC – Small Cell Lung Cancer
SE – Standard Error
SFUD – Single Field Uniform Dose
SOBP – Spread-Out Bragg Peak
SPHIC – Shanghai Proton and Heavy Ion Therapy Center

TCIA – The Cancer Imaging Archive
TCP – Tumor Control Probability
TPS – Treatment Planning Systems
TP – True Positive
VOI – Volume of Interest
WET – Water Equivalent Thickness

Publications related to this thesis

Peer-reviewed first author publications

- Martire MC, Volz L, Durante M, Pankuch M, Graeff C. Upright andsupine particle therapy of lung cancer: A 4Ddosimetric comparison. Med Phys.2026;53:e70377.https://doi.org/10.1002/mp.70377

Peer-reviewed co-authorship publications

- Volz L, Korte J, Maria CM, et al. Opportunities and challenges of upright patient positioning in radiotherapy. Inst Phys. 2024;69(18).doi:10.1088/1361-6560/ad70ee

Presented first author conference contributions

- Maria Chiara Martire et al. "Poster: Upright versus supine particle therapy of lung cancer: a 4D dosimetric study" in 61st Annual Conference of the Particle Therapy Co-operative Group, June 2023.

- Maria Chiara Martire et al. "Presentation: Dosimetric study of lung modulation and motion effects in carbon ion therapy for lung cancer" in: INSIGHTS Pisa Workshop, October 2023.

- Maria Chiara Martire et al. "Presentation: Upright and Supine therapy of lung cancer: a 4D dosimetric comparison" in: Upright Consortium Meeting, May 2024.

- Maria Chiara Martire et al. "Presentation: Dosimetric study of lung modulation and motion effects in carbon ion therapy for lung cancer" in: 63rd Annual Conference of the Particle Therapy Co-operative Group, June 2025.

- Maria Chiara Martire et al. "Presentation: Upright and Supine therapy of lung cancer: a 4D dosimetric comparison" in: 4D particle Therapy Workshop, November 2025.

- Maria Chiara Martire et al. "Poster: Field-wise online adaptive 4D-treatment planning in particle therapy" in 64th Annual Conference of the Particle Therapy Co-operative Group, June 2026.

Curriculum Vitae Maria Chiara Martire

Personal information

Name: Maria Chiara Martire

Date of Birth: 3rd March 1997

Place of Birth: Rome, Italy

Nationality: Italian

University education

11.2022 – now: PhD in Electrical Engineering and Information Technology, Technical University of Darmstadt

Thesis: Carbon ion therapy for lung cancer: enhancing dose conformity and cost-effectiveness

10.2021 – 03.2022: Erasmus+ student, GSI Helmholtzzentrum für Schwerionenforschung

10.2019 – 05.2022: Master of Science in Biomedical Engineering, University of Rome "La Sapienza"

Thesis: Assessment of advanced motion mitigation techniques for intra- and inter-fractional motion in lung tumors

10.2016 – 11.2019: Bachelor of Science in Clinical Engineering, University of Rome "La Sapienza"

Thesis: Dielectric spectroscopy of a numerical model of a single cell

School education

09.2011–07.2016: Liceo Scientifico A. Avogadro, Rome, Italy

High school diploma

Prizes

Giersch Excellence Grants" for ongoing doctoral studies, 2024

PTCOG Travel Fellowship for the PTCOG61, 2023

Acknowledgments

At the end of this thesis, I have to thank all the people who made this possible.

First, I have to thank my Professor, Christian Graeff, who guided me since the very beginning, when the PhD was not even an option and I arrived at GSI as an Erasmus student. When I found out that the German word for the PhD supervisor is "Doktorvater" I thought I could have not found a better one. I have to extend my gratitude to Lennart Volz ("älterer Doktorbruder" I guess). Both of you guided me step by step, taught me how to be a researcher, and most important, how to do this job with devotion.

I thank the PARTITUR project, and all the young and senior researchers who are part of it. It was extremely important to be part of such an interdisciplinary group. A special thanks to the PhD students in radiobiology who helped me during the experiments. Also, I have to thank Olga for her help, and for being patient enough to teach an engineer how to work in a cell lab.

I thank all the Biophysics department of GSI, starting from Marco Durante. Among all, thank you for reminding me every year that I have to submit the PTCOG abstract under the "Physics" topic. Maybe in another world I am a clinician, and my abstract would have not been rejected.
Thank you to all the people that are part of the Medical Physics group, who arrived few months ago and who have already left. When I arrived here Timo and Cosimo were PhD students of the group, then became two important friends. I learned a lot from each of you, we shared very long beam times hours together, but I am happy to only share good quality friend time now.
I have to thank all my present and past colleagues and friends at GSI. Daria, Martina, Luca, Gaia, Virginia, Federica, Fernando, Martina, Francesca and many many more. You make these offices a special place, and everything becomes a funny adventure with you. Please, just don't speak in front of my office.
A special thought goes to Cri. You inspire me every day, before from the office next to mine and now even more from the other side of the ocean. You are the pillar of a (sometimes) messy life.

I thank all my friends in Darmstadt. The list would be just too long. If it is true that people make places, you are definitely the reason why Darmstadt became Home. Special thanks to my girls, Laura and Olga. I shared multiple amazing, and few bad, moments of the last years with all of you, exactly as it happens in a large Family.
To the friends I met at the very beginning of my life here, to the friends who arrived later, to whom has already left and to whom is no longer here but always will be.

A questo punto, non posso che ringraziare tutta la mia Famiglia. I miei genitori, per essere sempre stati con me, per non avermi mai fatto mancare il vostro appoggio. Siete il mio punto di riferimento, le mie radici che affondano nella cittá piú bella del mondo.
Grazie a mio fratello Francesco e a Sara, sei da sempre come una sorella.

Last special thanks to Leander. You do the most important thing of all; you make me happy every day. You are simply fantastic.